

UNIVERSITY OF GENOVA
POLYTECHNIC SCHOOL



DICCA

Dipartimento di Ingegneria Civile, Chimica e Ambientale

MASTER OF SCIENCE THESIS

IN

REHABILITATION ENGINEERING AND BIOMATERIALS

**Numerical investigation of SARS-CoV-2
and atmospheric particulate deposition
on the surface of the eye**

Candidate

Gianmarco Carboni

Supervisor

Prof. Ing. Jan Oscar Pralits

Supervisor

Prof. Ing. Rodolfo Repetto

October 2020

Abstract

The purpose of this master thesis is to establish how the ocular surface can be protected from potentially harmful external agents by exploiting both physiological structures such as eyelashes, as shown in case study A, and protective devices such as the lens of a pair of glasses such as shown in case study B. In order to evaluate these aspects, since it is complicated to evaluate the deposition of particles in a simplified model due to the limitations that the latter presents, the study is focused on evaluating, as a useful data for the purposes of the study, the number of particles deposited on the eyelashes and on the lens. Furthermore, for the same reasons of simplicity of the model, the number of particles deposited on the surface of the eye is statistically low, for this reason the presence of particles in a cylindrical volume placed near the surface of the eye was evaluated.

In the first part of the work we focused on an aspect studied by Amador *et al*: the role that eyelashes play in daily life and the optimal length of these evaluated with the ratio L/W in which L is the length of the eyelashes, W the diameter of the eye. We have chosen as a case study a person who runs and walks in an area polluted by PM10. The results show that as the number of eyelashes and their length increases, the number of particles captured increases.

In the second part of the work we have focused on an aspect that has been extensively studied over the years for various viruses and which has spread during 2020 due to the pandemic caused by the Sars-CoV-2 virus; how do the potentially virus-carrying saliva droplets move from a source following an event such as a sneeze and a cough and how the ocular surface can be protected, also in this case, through a lens of a pair of glasses. By evaluating the quantification of deposited particles, the presence of glasses is fundamental for the capture of salivary droplets for the purpose of preventing contagion.

Sommario

Lo scopo di questo lavoro di tesi è stabilire come la superficie oculare possa essere protetta da agenti esterni, potenzialmente dannosi, sfruttando sia strutture fisiologiche come le ciglia, come mostrato nel caso di studio A, sia dispositivi di protezione come delle lenti di occhiali come mostrato nel caso di studio B. Al fine di valutare questi aspetti, essendo complicato valutare il deposito di particelle in un modello semplificato a causa delle limitazioni che quest'ultimo presenta, lo studio è incentrato nel valutare, come dato utile ai fini dello studio, il numero di particelle depositate sulle eyelashes e sulla lente. Inoltre, per gli stessi motivi di semplicità del modello, il numero di particelle depositate sulla superficie dell'occhio è statisticamente basso, per tale motivo è stata valutata la presenza di particelle in un volume cilindrico posto in prossimità della superficie dell'occhio.

Nella prima parte del lavoro ci siamo concentrati su un aspetto studiato da Amador *et al*: il ruolo di protezione che le ciglia svolgono nella vita quotidiana e la lunghezza ottimale di queste valutata secondo il rapporto L/W nel quale L è la lunghezza delle ciglia, W il diametro dell'occhio. Abbiamo scelto come caso di studio una persona che corre e cammina in un'area inquinata da PM10. I risultati mostrano che all'aumentare del numero di eyelashes e della lunghezza di esse, aumenta il numero di particelle catturate.

Nella seconda parte del lavoro ci siamo concentrati su un aspetto che è stato ampiamente studiato negli anni per vari virus e che ha preso piede nel corso del 2020 a causa della pandemia causata dal virus Sars-CoV-2; come si muovono le goccioline di saliva, potenzialmente portatrici di virus, da una sorgente a seguito di un evento come uno starnuto e un colpo di tosse e come proteggere la superficie oculare, anche in questo caso, attraverso la lente di un occhiale. Valutando la quantificazione delle particelle depositate, la presenza di una lente è fondamentale per la cattura delle goccioline salivari al fine di prevenire il contagio.

Contents

1	Introduction	1
I	Case Study and Numerical Tools	8
2	Eye and Eyelashes description	9
2.1	Eye's anatomical structure	9
2.2	Eyelashes's anatomical structure	10
2.3	Cad geometry of the eye and the eyelashes	13
2.4	Cad geometry of the protection's devices	16
3	Open Source Tools	20
3.1	Onshape	20
3.2	OpenFOAM	20
3.3	OpenFOAM case structure	24
3.4	The programming language of OpenFOAM	25
3.4.1	Why <i>C++</i>	25
II	Fluid Dynamics Characterization of Eye and Eye-	
	lashes	28
4	Governing Equations	29
4.1	Conservation laws	29
4.1.1	Continuity equation	29
4.1.2	Conservation of Linear Momentum	30
4.1.3	Conservation of Energy	31

4.2	Turbulence modelling	33
4.3	Standard $k - \epsilon$ model	36
4.4	Near wall treatment	37
4.5	The Finite Volume Method	39
5	Simulations of the flow field	42
5.1	<i>Mesh</i> generation	43
5.1.1	Grid convergence	49
5.2	Case study	51
5.2.1	Case study A: Flow field for Atmospheric particulate . . .	51
5.2.2	Case study B: Flow field for Droplets	54
5.3	Results	57
5.3.1	Case study A	57
5.3.2	Case study B	59
III	Simulations with Particles	72
6	Particle Implementation	73
6.1	Governing Equations	73
6.1.1	Particle equations	74
6.2	Dispersion Models	76
7	Particle Simulations and Results	77
7.1	Case study	77
7.1.1	Choice and setup of atmospheric particulate deposition . .	79
7.1.2	Choice and Setup of Droplets deposition	80
7.2	Results	82
7.2.1	Atmospheric particulate deposition	82
7.2.2	Droplets deposition	96
	Discussion	106
	Conclusions	108
	Appendix	109

Chapter 1

Introduction

The eye is exposed to the environment, making it vulnerable to viral, bacterial, fungal and parasitic infections and their associated medical conditions [1]. This implies that certain viral infections can be transmitted through the eye. In recent days this has become a particularly relevant issue owing to the outbreak of pandemic associated with the infection by the Coronavirus (Sars-CoV-2), which causes a respiratory disease called COVID-19. The Sars-CoV-2 virus is a spherical particle of 0.125 (0.05-0.2) μm (micron) in diameter. The outer envelope, called the pericapsid, is made up of four structural glycoproteins: *Spike*, *Envelope*, *Membrane* and *Nucleocapsid* and a lipid coating as shown in *Figure 1.1*. Inside the pericapsid there is a single strand of RNA (positive sense) of ~ 30 kb which contains 30 000 bases, a very large genome for an RNA virus [2].

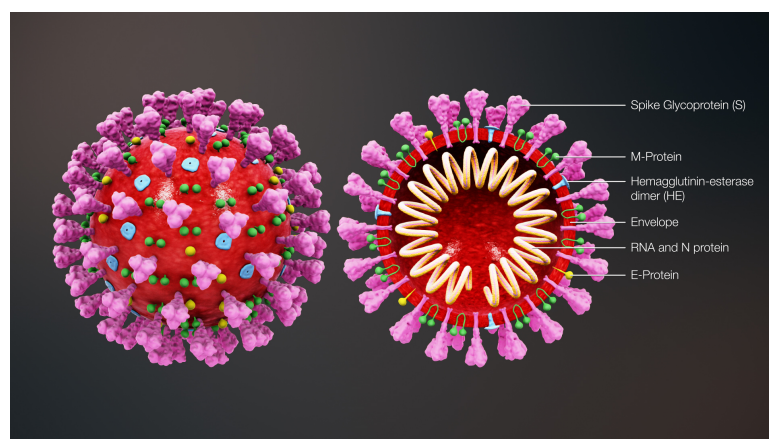


Figure 1.1: Schematic illustration of Sars-CoV-2 (credit: <https://www.scientificanimations.com/wiki-images/>).

The infection by the virus occurs mainly by air and two aspects play a fundamental role: the knowledge of the viral load that droplets are potentially capable of bringing us and the knowledge of their persistence over time [3]. Two mechanisms for air transmission are distinguished [4]:

- Near infection associated with large droplets
- Distant infection associated with small droplets

In the case of small droplets it is common to speak of *bioaerosol* contact (e.g., from talking, coughing, or sneezing). The properties of the cough have been studied extensively; cough is found to be one of the prime sources of airborne diseases as it has high velocity and large quantity of droplets [5] and the *cloud* of cough is formed by a two-phase mixture of moist air and drops in the immediate vicinity of the mouth. This phenomenon is different than sneezing in which the *cloud* is denser and shows not only drops and moist air but also liquid fragments of significant size [3]. In the case of coughing the Reynolds number is estimated to be 10^4 , in the case of sneezing 4×10^4 . The fluid dynamic analysis of vocal emissions, like talking, has not attracted as much attention from the scientific community but is known that the *cloud* is less dense and the Reynolds number is lower.

An interesting work by Chao *et al.* showed jet velocity measurements with the aid of PIV (*Particle Image Velocimetry*). The results of these measurements show that:

- The average expiration air velocity was 11.7m/s for coughing and 3.9m/s for speaking
- The geometric mean diameter of droplets from coughing was $13.5\mu m$ and it was $16.0\mu m$ for speaking
- The estimated total number of droplets expelled ranged from 947 to 2085 per cough and from 112 to 6720 for speaking
- The evaporation effect of the droplets is negligible

It must be noted here that the term *bioaerosol* is used with the medical meaning of a tiny, airborne particle that is composed of or derived from biological matter, which can spread infectious diseases by carrying viruses [6]. It is assumed that

the distance of one meter ensures protection from infection associated with the dispersion of drops by air; as illustrated in the *Figure 1.3*, some numerical and experimental models are present in the literature which estimate the distance reached by the respiratory emissions [7]

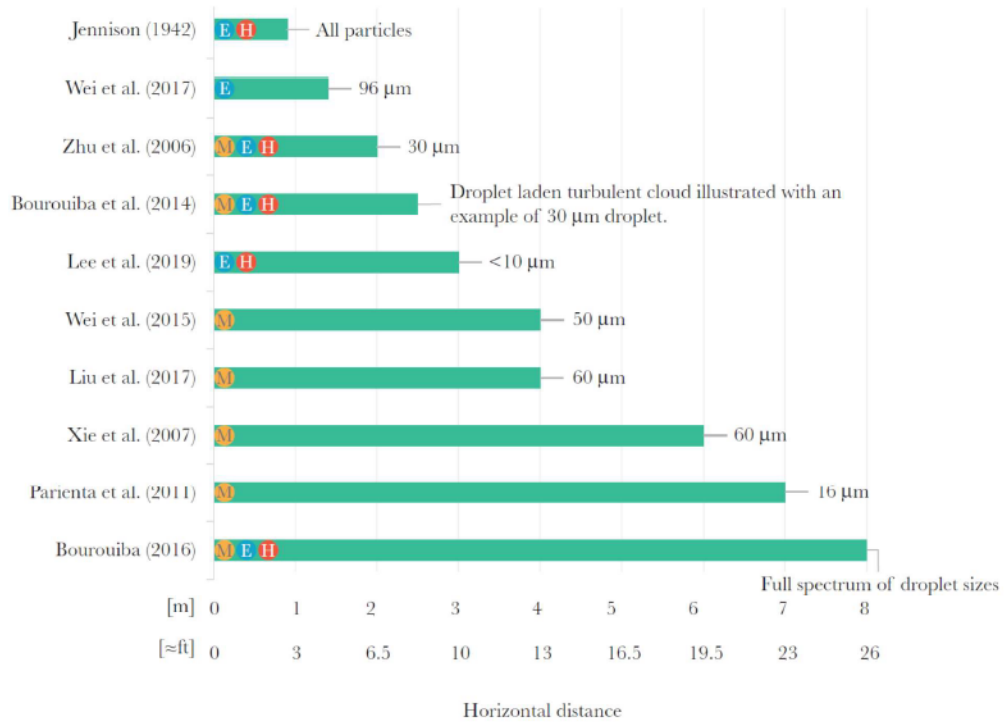


Figure 1.2: *Forecast of the distance reached by respiratory emissions, based on mathematical or numerical models (M), experimental observations (E) or experimentation on patients (H)[7].*

Airborne droplets carrying the pathogen can also transmit the infection if they come into contact with the eyes and the virus might be spread if someone touches a surface where the virus is present, and then touches mouth, nose or eyes. For this reason, the World Health Organisation has issued guidelines for protection of healthcare workers (HCWs) that recommend contact and droplet precautions for HCWs caring for suspected COVID-19 patients [8]. Although the conjunctiva is directly exposed to extraocular pathogens, and the mucosa of the ocular surface and upper respiratory tract are connected by the nasolacrimal duct and share the same entry receptors for some respiratory viruses, the eye is rarely involved in human CoV infection and conjunctivitis is quite rare in patients with Sars-CoV-2 infection. However, pathogens that the ocular surface is exposed to might be

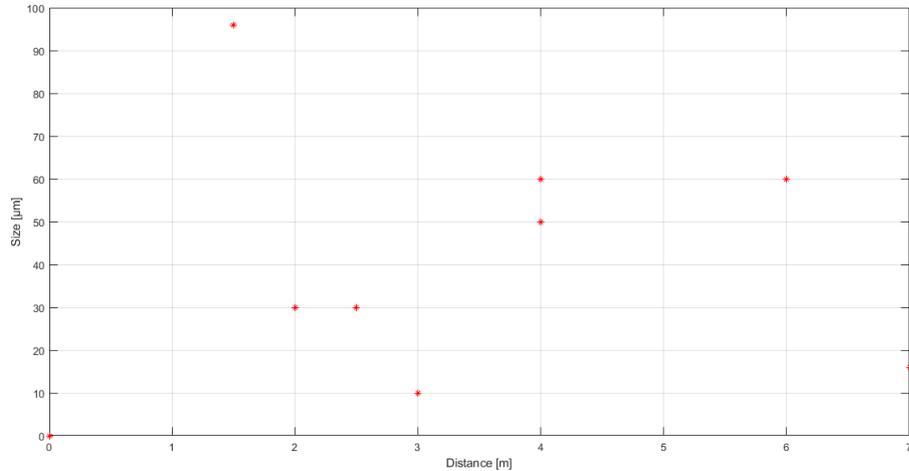


Figure 1.3: *Trend of data following the previous work [7].*

transported to nasal and nasopharyngeal mucosa by constant tear rinsing through the lacrimal duct system and then cause respiratory tract infection [9]. If the viral particles are able to reach the respiratory mucous membranes, a fusion occurs between the viral pericapside and the membrane of the human cell so that the viral RNA can penetrate inside the cell to reproduce.

So far, no consistent association has been found between concentration of airborne particles of Sars-CoV-2 onto the ocular surface and percentage of positive patients. Instead, it has already been demonstrated that there are connections between other viral infections of the lungs and particles deposition on the surface of the eye; the respiratory syncytial virus (RSV) when is instilled in the live murine eye, not only replicated robustly in the eye but also migrated to the lung and produced a respiratory disease that is indistinguishable from the standard, nasally acquired RSV disease [10]. In general, respiratory viruses (including adenovirus, influenza virus, respiratory syncytial virus, coronavirus, and rhinovirus) which cause a broad spectrum of disease in humans, have the ability to use the eye as a portal of entry as well as a primary site of virus replication [11].

The airflow direction was consistent with droplet transmission; virus transmission in this outbreak cannot be explained by droplet transmission alone. Larger respiratory droplets ($> 5\mu m$) remain in the air for only a short time and travel only short distances, generally $< 1m$. Virus-laden small ($< 5\mu m$) aerosolized droplets can remain in the air and travel long distances, $> 1m$ [12].

The speed and direction of local airflow can be further modified by artificial objects in eye vicinity. For example, it is highly likely that even regular eyeglasses can restrict the airflow around the eyes, although we are not aware of a quantitative evaluation of this phenomenon [13]. To ensure total protection of the ocular surface, the best solution is the development of a filtered eye mask comprising an eye protection device with a filter to maintain a virus-free air mass in front of the eye [14] as shown in *Figure 1.4*.

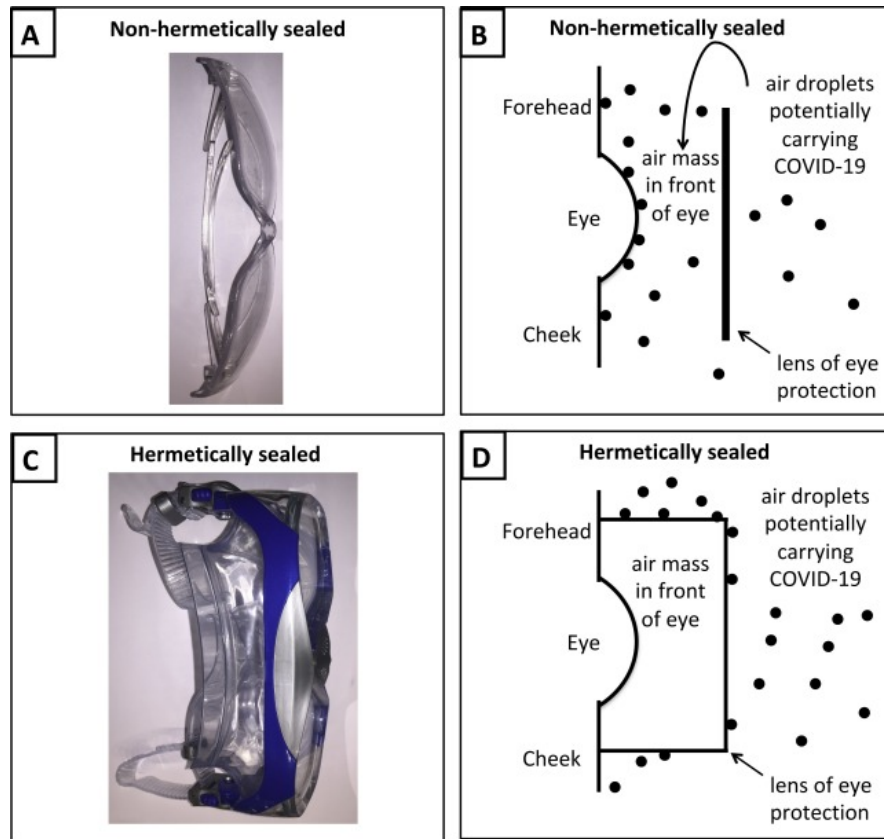


Figure 1.4: Pictures of non-hermetically sealed (A, B) and hermetically sealed (C, D) eye protection devices[14].

At the same time, eyes are exposed to atmospheric airborne particles. Their deposition velocity onto the ocular surface depends to a large degree on external factors other than particle size [15]. In this work we investigate the deposition of atmospheric particles on the ocular surface and what conditions affect a greater deposition; in fact, has been shown that the deposition of atmospheric particles, such as air pollutant particle, can cause some ocular symptoms, such as eye itch-

ing, foreign body sensation, tears and burning, as well as some other signs such as conjunctival congestion, increased mucus secretion, conjunctival keratoconus, swelling of the eyelids and conjunctival edema [16].

Among the airborne particles, PM10 particles have significant importance; it is an acronym that means Particulate Matter $\leq 10\mu m$, that is particulate material with a dimension less than or equal to 10 micrometers; with the same origin but an even smaller size, PM2.5 is also considered a powerful pollutant. In both cases, these are solid or liquid material, finely dispersed in the lower atmosphere and particularly sedentary in weather conditions similar to the current ones.

The origin of this particulate matter may be natural: it includes, for example, the particulate expelled during volcano eruptions, or the products of wood combustion developed during fires, or even plant pollens dispersed in the air in spring. It is not these natural causes, however, that cause concern in these winter days: our strong link with fossil fuels for automotive and heating must cause concern [17].

The possible role that airborne particles play in the possible transmission of the virus may be obscured if there is only a weak association between airborne particle concentrations, as conventionally measured, and the amount of particles of relevant sizes on the ocular surface [15]. Nevertheless, little is known about the fact that these particles can carry pathogens and how environmental conditions affect protection against Sars-Cov-2 but it is shown that exists a positive correlation between the level of air pollution of a region and the lethality related to COVID-19, indicating air pollution to be an elemental and concealed factor in aggravating the global burden of deaths related to COVID-19 [18]. Despite this, the influence that relative humidity, temperature and pollution generally intended have on the seasonality of Coronavirus infections that cause winter colds is well known [3]. We also investigate how a natural protection system, such as eyelashes, contributes to limit particles deposition on the ocular surface. They are speculated to act as “dust catchers” to protect the eye from dust falling from above [19]. In fact, interesting researches based on human eyelashes have been performed showing that mammal eyelashes, shown in *Figure 1.5* are the results of a natural selection and their length, orientation, quantity, and other parameters seem to follow a certain optimisation law [20]. The parameters that are most interesting for the purposes of the work are the length and number of the lashes and the spacing between them; in fact a greater or shorter length than the average

length, or a greater or shorter number of lashes present, may be a symptom of a possible pathology and for this reason they have been evaluated as the object of study. In addition, particular importance will be given to the speed of the incoming flow on the surface of the eye to understand how the cilia of a certain type can deviate it or deviate any particles or droplets carried by it; the cases analyzed, as explained in the next chapters, will concern a situation in which a person is taking a walk and a run.



Figure 1.5: *The eye of a mammalian goat, including a side-view (a), a plan view (b) and a close-up of the eyelashes (c)*[1].

Currently, previous studies evaluate how eyelashes are able to diverge the flow to protect the eye [1] and how eyelashes can protect the eye through inhibiting ocular water evaporation [20] but in all of these, simplifications of the geometric model are implemented and problems relating to specific airborne particles, such as droplets or atmospheric particulates, are not considered. Phenomena of particle deposition can be simulated with computational fluid dynamics. The purpose of this project is to estimate, through numerical simulations, how the deposition of atmospheric particles and potentially infectious droplets can be decreased thanks to the use of eye protection devices and how the morphology and the position on the eyelid's edge of the eyelashes can allow to achieve the same result. In the following text, the results of numerical simulations used to study the dynamics of airborne particles and droplets and their deposition on the surface of the eye are presented.

Part I

Case Study and Numerical Tools

Chapter 2

Eye and Eyelashes description

2.1 Eye's anatomical structure

The eye is our organ of sight. The eye has a number of components which include but are not limited to the cornea, iris, pupil, lens, retina, macula, optic nerve, choroid and vitreous [21]. as shown in *Figure 2.1*.

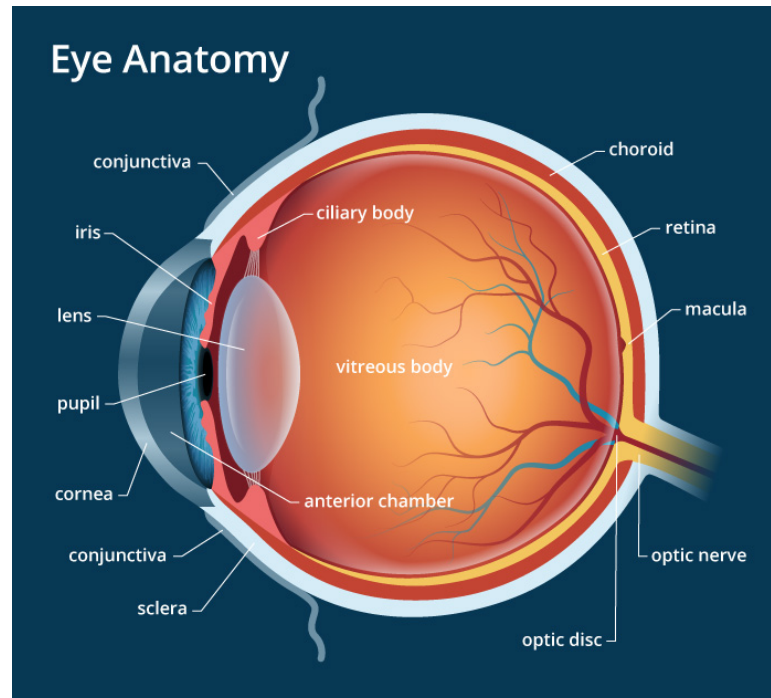


Figure 2.1: *Pictures of eye anatomical structure.* Credits: <https://www.onlinebiologynotes.com/human-eye-anatomy-parts-structure>[21]

- Cornea: clear front window of the eye that transmits and focuses light into the eye
- Iris: colored part of the eye that helps regulate the amount of light that enters
- Pupil: dark aperture in the iris that determines how much light is let into the eye
- Lens: transparent structure inside the eye that focuses light rays onto the retina
- Retina: nerve layer that lines the back of the eye, senses light, and creates electrical impulses that travel through the optic nerve to the brain
- Macula: small central area in the retina that contains special light-sensitive cells and allows us to see fine details clearly
- Optic nerve: connects the eye to the brain and carries the electrical impulses formed by the retina to the visual cortex of the brain
- Vitreous: clear, jelly-like substance that fills the middle of the eye

2.2 Eyelashes's anatomical structure

The eyelids are also known as the palpebrae, and are formed by the reinforced folds of skin that are attached to the slight skeletal muscles which permit movement. The orbicularis oculi muscle assists in the control of the eyelids, and it receives additional assistance from the levator palpebrae superioris muscle, which is designated to the upper eyelid and explains why the upper lid has more movement options than the lower lid.

When the eyelids draw down over the eye, or the eyes “close”, it is the result of the orbicularis oculi muscle contracting. When the levator palpebrae superioris muscle contracts, the result is the “opening” of the eye, or the eyelid drawing back up over the eye to reveal the eyeball.

The eyeball is protected by the eyelid, both from desiccation and from impalement. When the eyelid blinks, which occurs every 7 seconds or so, fluid flushes the eyeball and keeps it moisturized. The eyelid also reflexively blinks when the eye

senses a particle that threatens to enter it. The eyelid will usually blink reflexively when the eye is adjusting to a new line of vision to help prevent the initial blurry vision that can occur from refocusing too quickly

The last forms of secretion protection available for the eyelids are the modified sweat glands known as ciliary glands. All of these glands help to keep proper moisture in the eye and permit smooth eye movements and operation. If one of the sebaceous glands becomes infected, this is commonly referred to as a sty.

Each eyelid is the perfect anchoring ground for eyelashes, one row per eyelid. Each single eyelash is embedded into the eyelid by the root, which anchors into a root hair plexus. This give the eyelash hairs additional sensitivity to snap the eye closed in the event of an airborne particle reaching the eye.

The eyelashes belonging to the upper lids and the lower lids vary from each other. The upper lid eyelashes are longer, tend to curve in an upward direction, and are more noticeable than the lower lid eyelashes, which are shorter and tend to be stumpy without much curve [22]. It is important to underline that the terminal eyelash fibre is characterized by a regular curved shape, more or less marked depending on ethnic origin. Because of the aesthetic value of eyelashes, various cosmetics and procedures have been developed to make eyelashes look longer, more voluminous and curled. However, eyelashes have been far less investigated than scalp hair, and the information available is insufficient. Moreover, in terms of the effect of ethnicity, little is known [23]. The number of lashes is variable, higher in the upper eyelid than in the lower one, but generally between 150 and 200 against 50-150. The lashes of the small upper eyelid also to be longer, 8 to 12 mm versus 6-8 mm of the lower eyelid [24].



Figure 2.2: *Pictures of eyelashes anatomical structure.* Credits: <http://www.medicalook.com/humananatomy/organs/Eyelidsandeyelashes.html> [22]

Mammal eyelashes are the typical results of natural selection and its length, orientation, quantity and other parameters seem to follow a certain selection law. Its protective functions, however, are not yet fully understood. Eyelashes are a hair structure which is very common for mammals and similar structures can also be found in birds and reptiles. Generally, as a product of biological evolution, eyelashes have different structures and functions for animals living in different environments [20].

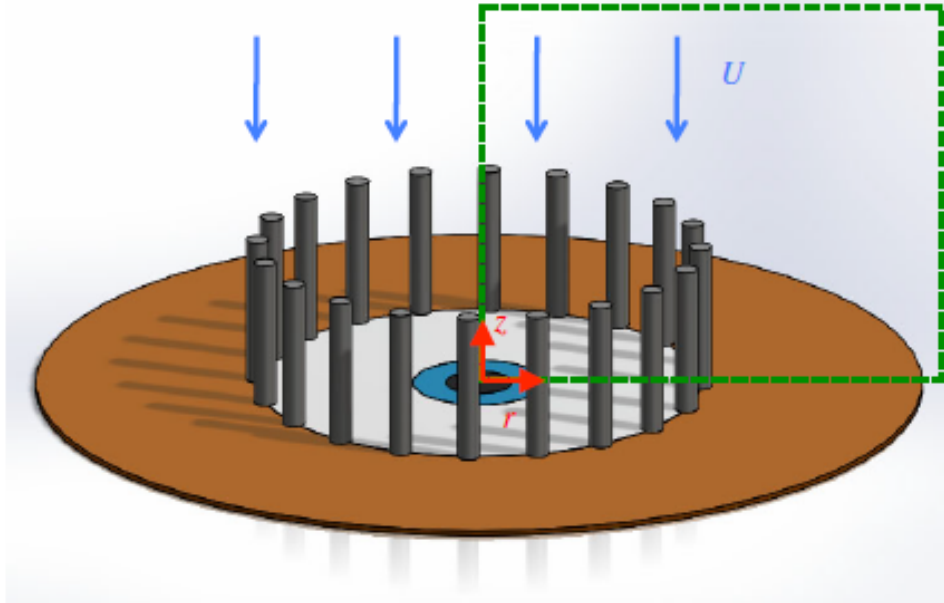


Figure 2.3: Geometry of eye and eyelashes used by Amador et al.[1]

2.3 Cad geometry of the eye and the eyelashes

The dissertation starts with a description of the CAD geometry of the eye and the eyelashes which are the fundamental components of this of Computational Fluid Dynamic (CFD), a tool that analyzes and solves fluid dynamics problems; the description of this tool will be explain in *Chapter 4*. The software system that has been used to generate the geometries is Onshape, as explained in the next chapter. The first basic step in a computational fluid dynamics case is to obtain the geometry of the domain where we will run our simulations. The following section describes all the assumptions that have been made when going from reality to the aerodynamic model of the eye and eyelashes. The basic guideline in this process of geometrical modelling is to keep the model as close as possible to the reality without forgiving that computational fluid dynamics can be extremely time consuming. In order to achieve an acceptable computational effort simplifications of the real geometry are needed. If the physics of the problem (and the experience in CFD) suggests that an element isn't fundamental in the overall aerodynamic of the model, the element can be simplified.

The first geometry taken into consideration has been inspired by Amador *et al.*'s work, as shown in *Figure 2.3*

The calculation volume, the domain, is made up of a horizontal plane with

dimensions $2.5W \times 2.5W$, $W = 20mm$ and the height of the volume is $7W$. The eye is shaped like a disk with diameter W and on the edge of this disk there are 20 equally spaced cylinders which represent the eyelashes; each cylinder has a diameter $d = 1mm$ as shown in Figure 2.5 and an height of $L = 5.8mm$.

The surfaces delimiting the calculation volume have been named as follows:

- *Bottom*
- *Top*
- *North*
- *South*
- *West*
- *East*

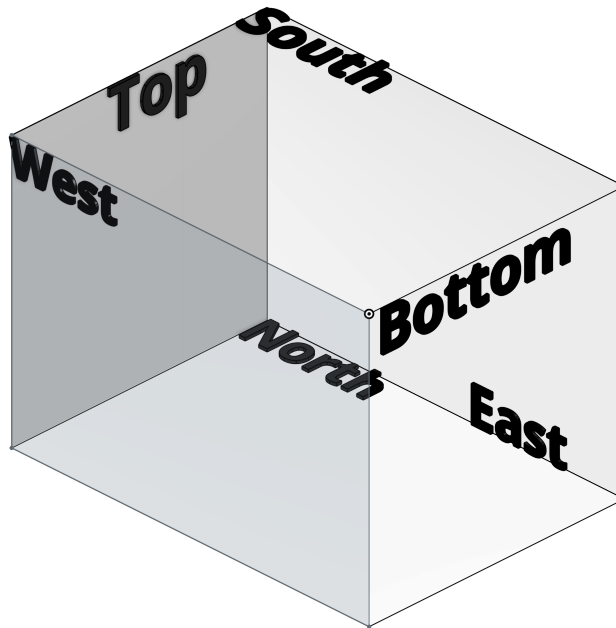


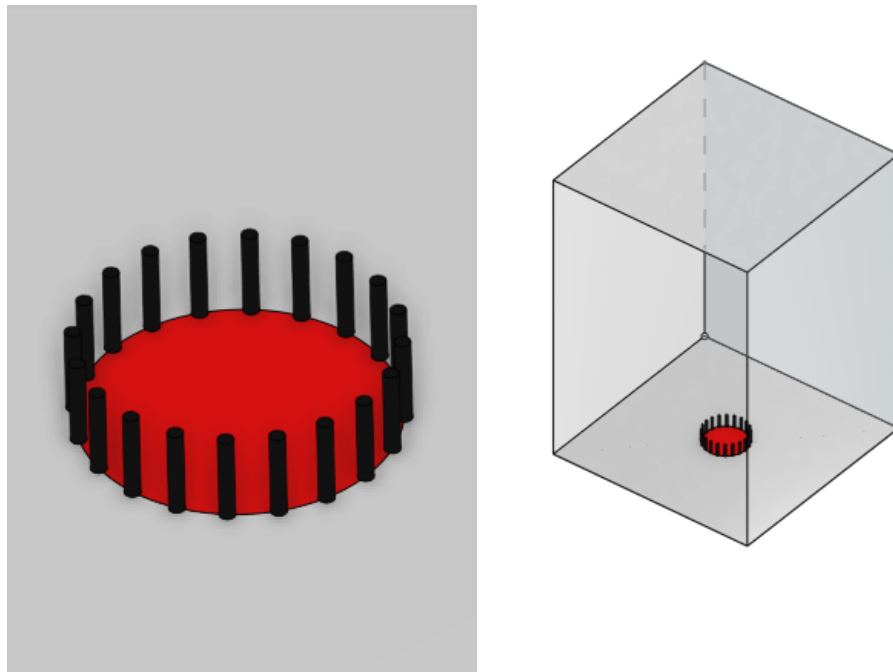
Figure 2.4: *Model of the control volume*

During numerical simulations, *Bottom* represents the part of the face that surrounds the eye, *Top* represents the inlet of the computational domain

for particles and flux, North, South, East and West represent the side walls of the computational domain and the other two patches are *eye and eyelashes*.

As can be noted in the previous description, the real geometry of the eye and eyelashes is really complex and includes a lot of small details. This kind of detail could have an impact on the fluid motion but they can highly increase the computational cost of simulations and for this reason they will be simplified. It's reasonable to expect, in future studies, that the first point to be developed is an improvement of the geometry.

The resulting geometry is a rectangular parallelepiped domain, 20 cylinders and a circular disk. All components designed are showed in *Figure 2.6*



(a) *Eye and eyelashes*

(b) *Entire domain*

Figure 2.6: *CAD of the control volume*

Due to the fact that different ethnic groups have different eyelash lengths and number of eyelashes, in order to parameterize the simulations that will be explained in the following chapters, different geometries have been generated: assuming that the diameter remains unchanged $d = 1mm$, the size of the eye remains unchanged $W = 20mm$ the lash lengths $L = 7.1mm$ and $L = 9.0mm$ were evaluated as shown in *Figure 2.7*



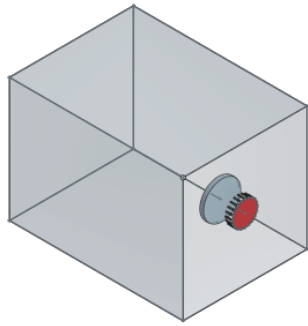
Figure 2.7: *Different eyelashes length: green eyelashes $L = 9.0\text{mm}$, brown eyelashes $L = 7.1\text{mm}$, black eyelashes $L = 5.8\text{mm}$*

The same geometries have been recreated in a similar way by modifying the number of eyelashes around the eye and approaching the real case; from 20 eyelashes to 30 and 40 eyelashes.

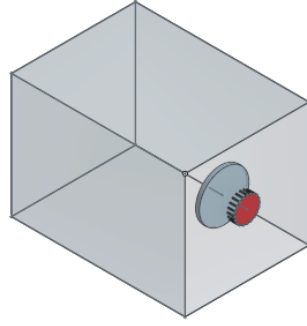
2.4 Cad geometry of the protection's devices

Using the same software introduced in the previous section, three different protection's devices as shown in *Figure 2.8* have been developed; their usefulness consists in diverging air flows and any particles carried by them. The aim of the modeling of these geometries is to find the optimal size and morphology of the protection's device, as example glasses, to protect the surface of the eye.

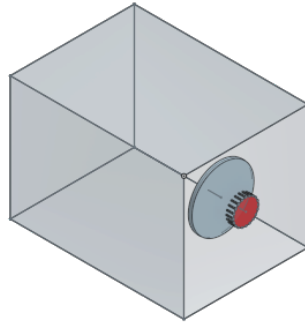
Also in this case, to avoid too high a computational cost, the ocular protection device has been simplified to a lens with shapes of a simple cylinder. Three diameters $d = 3\text{cm}$, $d = 4\text{cm}$, $d = 5\text{cm}$ were chosen. The distance between the lens and the eye is 2cm and the thickness of the lens 3mm .



(a) *Lens $d=3\text{cm}$*

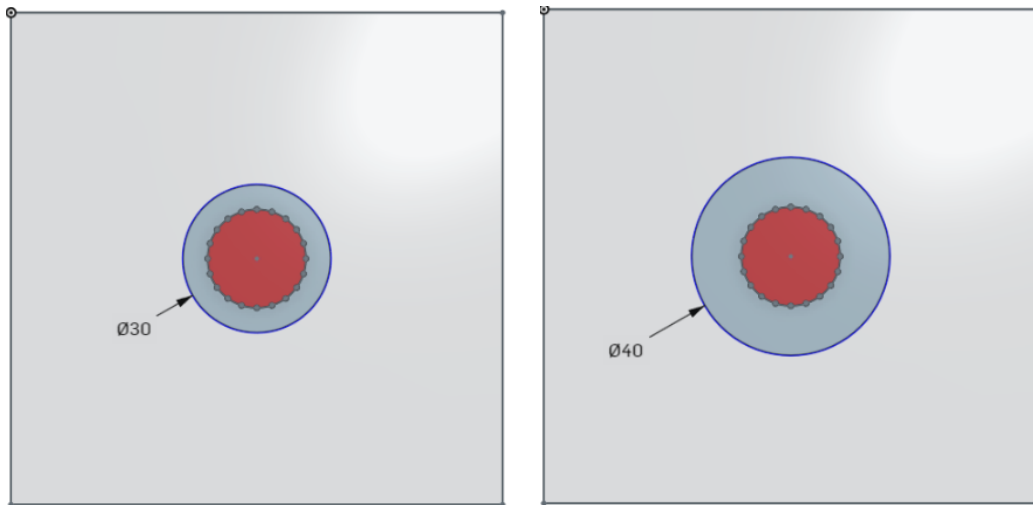


(b) *Lens $d=4\text{cm}$*



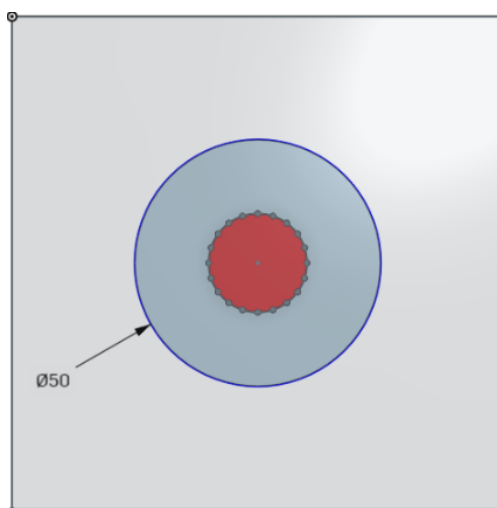
(c) *Lens $d=5\text{cm}$*

Figure 2.8: *CAD of the control volume and protection's device*



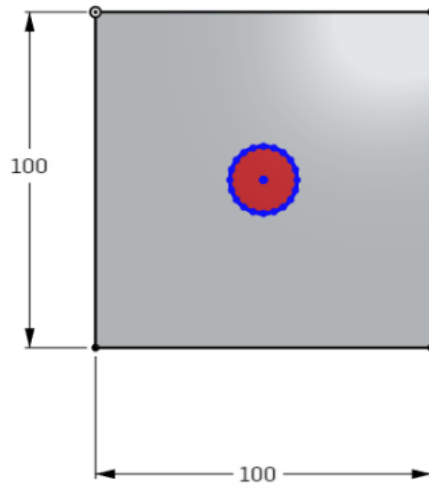
(a) *Lens d=3cm*

(b) *Lens d=4cm*

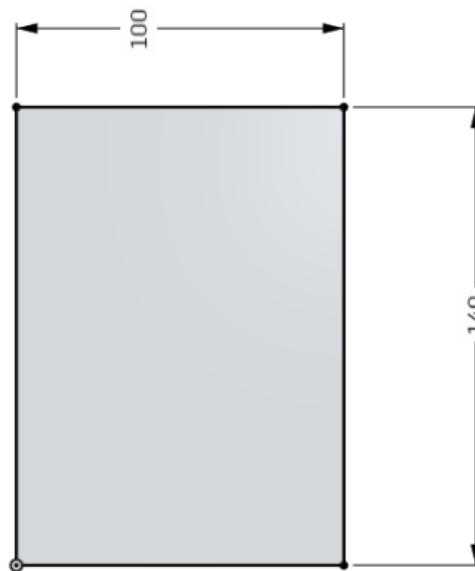


(c) *Lens d=5cm*

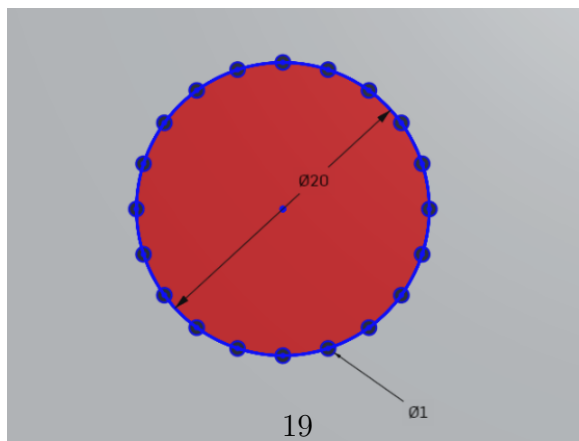
Figure 2.9: *Prospectus of the control volume and protection's device*



(a) *Horizontal view*



(b) *Vertical view*



(c) *Horizontal view of the iris*

Figure 2.5: *Different surfaces of the control volume*

Chapter 3

Open Source Tools

3.1 Onshape

Onshape is a computer-aided design (CAD) software system that is used in a wide range of industrial fields including consumer electronics, mechanical machinery, medical devices and 3D printing. It is the only product design platform built from scratch using the latest cloud web and mobile technologies work and the 3D modelling part of it is completely free and online. With Onshape's unique architecture it is possible to build complex parametric parts, assemblers and production ready drawings. Data management is built-in so there's no waiting for files to be checked in or checked out and no accidental overrides. Onshape support also a programming language, Feature Script that can be used to define custom feature [25]. Thanks to real-time functionality of Onshape, team members could edit feature's update during the work and see the impact of design change instantly. In this thesis, this tool has been used to create the geometry of various cases, changing the dimensional parameters of the eye and eyelashes on a case-by-case basis.

3.2 OpenFOAM

OPENFOAM[®] (*Open source Field Operation And Manipulation*) is an open source finite volume software for computational fluid dynamics (CFD), owned by OPENFOAM[®] Foundation and distributed exclusively under the GNU General Public Licence (GPL) [26]. That means it is freely available and according to

the GNU general public license principles the users can modify and share the source code that is freely distributed. Generally speaking OPENFOAM[®] is a C++ library, used to solve partial differential equations (PDEs), and ordinary differential equations (ODEs). Its primary usage is to create executables, known as applications that fall into two categories: solvers, each of which is designed to solve a specific problem in continuum mechanics, and utilities, that are designed to perform tasks that involve data manipulation [26]. The OPENFOAM[®] distribution has an extensive range of features to solve anything from complex fluid flows involving combustion and chemical reactions, multiphase flows and mass transfer, turbulence and heat transfer, particle methods (DEM,DSMC,MD) and Lagrangian particles tracking to acoustics, solid mechanics and electromagnetics. It includes tools for meshing in and around complex geometries, and for data processing and visualisation, and more. Almost all computations can be executed in parallel as standard to take full advantage of today’s multi-core processors and multi-processor computers. OPENFOAM[®] is supplied with pre- and post-processing environments. The interface to the pre- and post-processing are themselves OpenFOAM utilities, thereby ensuring consistent data handling across all environments [26]. The overall structure of OPENFOAM[®] is shown in *Figure 3.1*.

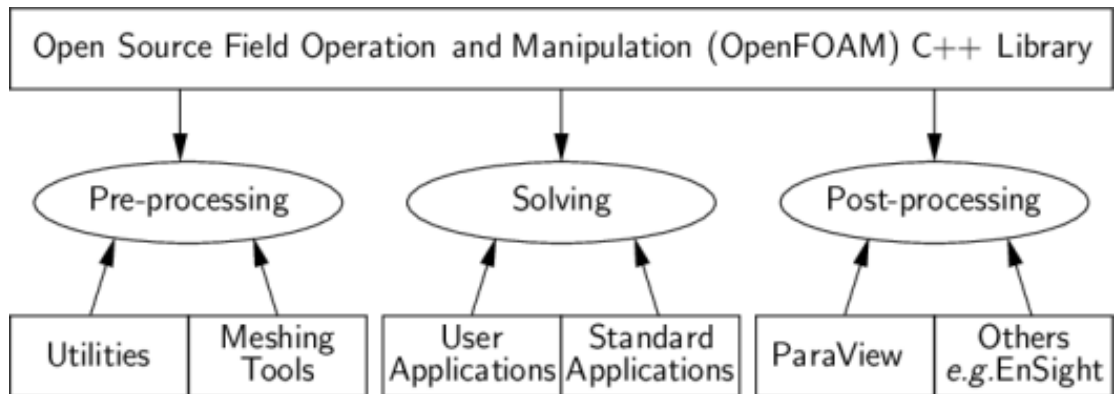


Figure 3.1: *Overview of OpenFOAM structure [26].*

At the core of these libraries are a set of object classes that allow the programmer to manipulate meshes, geometries, and discretization techniques at a high level of coding. Tables 4.1, 4.2, 4.3 and 4.4 present a list of the main OPENFOAM[®] classes and their functions. These classes represent the basic bricks for the development of OPENFOAM[®] based applications and utilities [27].

Objects	Type of data	openFOAM [®] Class
Interpolation	Differencing schemes	surfaceInterpolation<template>
Differential operator (explicit)	ddt, div, grad, curl	fv::
Differential operator (implicit)	ddt, d2dt2, div, laplacian	fvn::

Table 3.1: *Numeric and discretization [27].*

Objects	Type of data	openFOAM [®] Class
Variables	Primitive variables	scalar, vector, tensor
Mesh components	Point, face, cell	point, face, cell
Finite volume mesh	Computational mesh	fvMesh, polyMesh
Time	Time database	Time

Table 3.2: *Computational domain [27].*

Objects	Type of data	openFOAM [®] Class
Field	List of values	Field< template >
Dimension	Dimension set up	dimensionSet
Variable field	Field + mesh + boundaries + dimension	GeometricField< template >
Time	Time database	Time

Table 3.3: *Field operation [27].*

Objects	Type of data	openFOAM [®] Class
Sparse matrix	Matrix Coefficients and manipulation	lduMatrix, fvMatrix
Iterative solver	Iterative matrix solver	lduMatrix::solver
Preconditioner	Matrix preconditioner	lduMatrix::preconditioner

Table 3.4: *Linear equation system and linear solvers [27].*

Hence it is clear that OPENFOAM[®] capabilities mirror those of commercial CFD applications, but there are still some disadvantages compared to them, such as the lack of a native GUI, not much available documentation and, in wider terms, it is less user friendly; however, as the users have complete access to the source code, they have total freedom to modify existing solvers or use them as the starting point for new ones with some pre-requisite knowledge of the underlying method, physics and programming techniques involved. Summing up some of the features of OPENFOAM[®] are listed below taken from the official web-site [26]:

- FLUID DYNAMICS & PHYSICAL MODELLING

- Turbulence modelling (Reynolds-Averaged (RANS), Large-Eddy Simulation (LES), Detached-Eddy Simulation (DES, DDES, etc))

- Thermophysical modelling
- Transport/rheology
- Multiphase flows
- Rotating flows with multiple reference frames (MRF)
- Rotating flows with arbitrary mesh interface (AMI)
- Dynamic meshes
- Compressible/thermal flows
- Conjugate heat transfer
- Porous media
- Lagrangian particle tracking
- Reaction kinetics/chemistry
- GEOMETRY & MESHING
 - Mesh generation for complex geometries with *snappyHexMesh*
 - Mesh generation for simple geometries with *blockMesh*
 - Mesh conversion tools
 - Mesh manipulation tools
- NUMERICAL SOLUTION
 - Numerical method
 - Linear system solver
 - Parallel computing
- DATA ANALYSIS
 - *Paraview* post-processing
 - Post-processing command line interface (CLI)
 - Graphs and data monitoring

3.3 OpenFOAM case structure

The basic directory structure for a OPENFOAM[®] case, with the minimum set of files run an application, is presented in *Figure 3.2*.

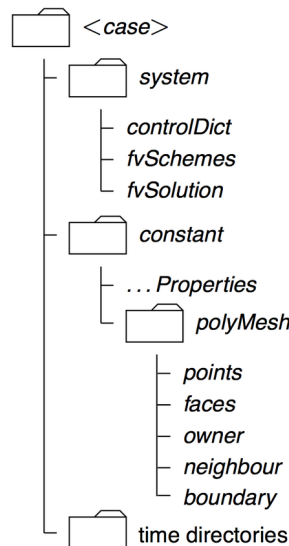


Figure 3.2: *Structure of an OPENFOAM[®] case [26]*

The roles of the main directories, contained in the case folder, are listed below:

- **system**, it contains the dictionaries to set up the entire solution procedure (from meshing to solving); at least it must contain three files:
 - **fvSchemes** to specify (run-time) the numerical schemes to discretize the equations;
 - **fvSolution** to set equation solvers, tolerances and other algorithm controls;
 - **controlDict** to control (run-time) the simulation run (start/end time, time-step, function objects etc.)
- **constant**, it contains a folder (**polyMesh**) with the full description of the case mesh and files that specify the physical properties involved (transport and turbulence properties, gravity, dynamic properties etc.)

- **time directories**, it contains files that represent the specific fields at initial condition (e.g. 0 folder) or computed by OPENFOAM[®] (e.g. 0.01, 0.02, ... folders, the name of these corresponds to the simulated time at which data are written) at consecutive times; it must be underlined that OPENFOAM[®] always require fields to be initialized, even in steady-state problems

A lot of pages should be written to exhaustively explain OPENFOAM[®], but that is beyond the scope of this thesis. For further details the CFD *direct* website [26] is suggested.

3.4 The programming language of OpenFOAM

3.4.1 Why C++

C++ is a *Object-Oriented Programming* language that attempts to provide techniques for managing complexity, achieving the aim of the reuse of software components. As an *Object-Oriented Programming* languages is based on three pillars of the object-oriented development [28]:

- encapsulation
- inheritance
- polymorphism

Encapsulation

C++ supports the properties of encapsulation through the creation of user-defined types, called classes. Once created a well defined class acts as a fully encapsulated entity and it is used as a whole unit. The actual inner workings of the class should be hidden. Users of a well defined class do not need to know how the class works; they just need to know how to use it.

Inheritance

C++ supports inheritance; a new type (class), which is an extension of an existing type, can be declared. This new subclass is said to derive from the existing type (sometimes is called a derived type) and inherits all its qualities, but the user can add new ones as needed.

Polymorphism

C++ supports the idea that different objects (belonging to the same class) do “the right thing” when the user chooses one of them. Being more exhaustive, in programming languages, polymorphism means that some code or operations or objects behave differently in different contexts.

A clarifier example inherent to a CFD code is relative to a velocity field. The expression encapsulates the idea of movement with direction and magnitude and relates to other physical properties. In mathematics, we can represent a velocity field by a single symbol, e.g. U , and express certain concepts using symbol, e.g. “the field of velocity magnitude” by $|U|$. The advantage of mathematics over verbal language is its greater efficiency, making it possible to express complex concepts with extreme clarity. The problems that we wish to solve in continuum mechanics are not presented in terms of intrinsic entities, or types, known to a computer, e.g. bits, bytes, integers. They are usually presented first in verbal language, then as partial differential equations in 3 dimension of space and time. The equations contain the following concepts: scalars, vectors, tensors, and field thereof; tensor algebra: tensor calculus; dimensional units. The solution to these equations involves discretisation procedures, matrices, solvers, and solution algorithms. Programming languages that are *Object-oriented*, as stated in the introduction to this chapter, provide the mechanism to declare types - *classes*- and associated operations that are part of the verbal and mathematical languages used in science and engineering. The velocity field introduced earlier can be represented in programming code by the symbol U and “the field of velocity magnitude” can be $mag(U)$. The velocity is a vector field for which there should exist, in a *Object-Oriented*, a *vectorField* class. The velocity field U would then be an instance, or object, of the *vectorField* class. The clarity of having objects in programming that represent physical objects and abstract entities should not be underestimated. The class structure concentrates code development to contained

regions of the code, the classes themselves, thereby easier to manage. New classes can be derived or inherit properties from other classes, e.g. the *vectorField* can be derived from a *vector class* and a *Field class*. *C++* provides the mechanism of template classes such that the template class *Field<Type>* can represent a field of any *<Type>*, e.g. scalar, vector, tensor. The general features of the template class are passed on to any class created from the template. Templating and inheritance reduce duplication of code and create class hierarchies that impose an overall structure on the code [29].

Part II

Fluid Dynamics Characterization of Eye and Eyelashes

Chapter 4

Governing Equations

4.1 Conservation laws

The principle of conservation states that, for an isolated system, certain physical measurable quantities are conserved over a local region. This conservation principle or conservation law is an axiom that cannot be proven mathematically but can be expressed by a mathematical relation. Laws of this type govern several physical quantities such as mass, momentum, and energy (the Navier-Stokes equations) [27]. The conservation laws involving fluid flow and related transfer phenomena can be mathematically formulated following either a Lagrangian (material volume, MV) or an Eulerian (control volume) approach. Assuming a continuous phase the most common method of describing fluid flow is the fixed reference system Eulerian approach that is synthetically presented below. A short description of the Lagrangian method will be introduced in the next section.

4.1.1 Continuity equation

The principle of conservation of mass indicates that, in the absence of mass sources and sinks, a region will conserve its mass on a local level [27]. Being ρ the density, through the application of the Reynolds transport theorem, the general expression for conservation of mass as applied to a control volume will be:

$$\int_V \frac{\partial \rho}{\partial t} dV + \int_S \rho \mathbf{V} \cdot \mathbf{n} dS = 0 \quad (4.1)$$

where S is the surface of the control volume V . Thanks to the divergence theorem - and noticing that the conservation of mass should be respected for

every control volume - this equation can be written in a differential form, called the continuity equation:

$$\frac{\partial \rho}{\partial t} + \nabla \cdot (\rho \mathbf{V}) = 0. \quad (4.2)$$

4.1.2 Conservation of Linear Momentum

Through application of the Reynolds transport theorem and divergence theorem, the general expression for conservation of linear momentum as applied to a control volume is:

$$\rho \frac{\partial \mathbf{v}}{\partial t} + \nabla \cdot (\rho \mathbf{v} \otimes \mathbf{v}) = \mathbf{f}. \quad (4.3)$$

Where $\mathbf{f} = \mathbf{f}_s + \mathbf{f}_b$ is the sum of the external surface forces \mathbf{f}_s and body forces \mathbf{f}_b acting on the control volume.

Surface forces

The forces acting on the control volume surface are due to pressure and viscous stresses which can be expressed in terms of the total stress tensor $\boldsymbol{\sigma}$ that in Cartesian coordinates is given by:

$$\boldsymbol{\sigma} = \begin{pmatrix} \sigma_{xx} & \tau_{xy} & \tau_{xz} \\ \tau_{yx} & \sigma_{yy} & \tau_{yz} \\ \tau_{zx} & \tau_{zy} & \sigma_{zz} \end{pmatrix} = \begin{pmatrix} -P & 0 & 0 \\ 0 & -P & 0 \\ 0 & 0 & -P \end{pmatrix} + \begin{pmatrix} \tau_{xx} & \tau_{xy} & \tau_{xz} \\ \tau_{yx} & \tau_{yy} & \tau_{yz} \\ \tau_{zx} & \tau_{zy} & \tau_{zz} \end{pmatrix} = -p\mathbf{I} + \boldsymbol{\tau}, \quad (4.4)$$

where \mathbf{I} is the identity tensor, p the pressure and $\boldsymbol{\tau}$ is the deviatoric of viscous stress tensor. The pressure is the negative part of the mean of the normal stresses and is given by:

$$p = -\frac{1}{3}(\sigma_{xx} + \sigma_{yy} + \sigma_{zz}). \quad (4.5)$$

Hence the surface force acting on a differential surface element dS is:

$$\int_S \mathbf{f}_s dS = \int_A \boldsymbol{\sigma} \cdot \mathbf{n} dA = \int_V \nabla \cdot \boldsymbol{\sigma} dV \longrightarrow \mathbf{f} = \nabla \cdot \boldsymbol{\sigma} = -\nabla p + (\nabla \cdot \boldsymbol{\tau}). \quad (4.6)$$

Body forces

Body forces per unit volume and the predominant ones are given below:

- Gravitational forces $\mathbf{f}_b = \rho \mathbf{g}$, due to the presence of a gravitational field

- Coriolis and centrifugal forces, respectively $\mathbf{f}_b = -2\rho(\boldsymbol{\omega} \times \mathbf{v}) - \rho(\boldsymbol{\omega} \times (\boldsymbol{\omega} \times \mathbf{r}))$, due to a rotating frame of reference

Hence introducing the expressions of surface and body forces in Eq. (4.3) the general conservative form of the momentum equation is obtained as:

$$\rho \frac{\partial \mathbf{v}}{\partial t} + \rho \nabla \cdot (\mathbf{v} \otimes \mathbf{v}) = -\nabla p + (\nabla \cdot \boldsymbol{\tau}) + \mathbf{f}_b \quad (4.7)$$

To proceed further the type of fluid should be specified in order to relate $\boldsymbol{\tau}$ with the other flow variables. For a Newtonian fluid the stress tensor is a linear function of the strain rate and is given by:

$$\boldsymbol{\tau} = \mu(\nabla \mathbf{v} + (\nabla \mathbf{v})^T) + \lambda(\nabla \cdot \mathbf{v})\mathbf{I}, \quad (4.8)$$

where μ is the molecular viscosity, λ the bulk viscosity coefficient usually set equal to $\lambda = \frac{2}{3}\mu$. Taking the divergence of Eq.(4.8) and substituting in Eq.(4.7) the final conservative form of the momentum equation for Newtonian fluids becomes also called Navier-Stokes equation:

$$\rho \frac{\partial \mathbf{v}}{\partial t} + \rho \nabla \cdot (\mathbf{v} \otimes \mathbf{v}) = \nabla \cdot (\mu \nabla \mathbf{v}) - \nabla p + \nabla \cdot (\mu(\nabla \mathbf{v}^T)) + \nabla(\lambda \nabla \cdot \mathbf{v}) + \mathbf{f}_b. \quad (4.9)$$

For incompressible flows the divergence of velocity vector is zero, $\nabla \cdot \mathbf{v} = \mathbf{0}$, and for constant molecular viscosity the momentum equation can be further simplified:

$$\rho \frac{\partial \mathbf{v}}{\partial t} + \rho \nabla \cdot (\mathbf{v} \otimes \mathbf{v}) = -\nabla p + \mu \nabla^2 \mathbf{v} + \mathbf{f}_b \quad (4.10)$$

4.1.3 Conservation of Energy

The conservation of energy (the first law of thermodynamics) simply states that energy can be neither created nor destroyed during a process; it can only change from one form (mechanical, kinetic, chemical, etc.) into another. Consequently, the sum of all forms of energy in an isolated system remains constant. Considering a material volume MV of mass m , density ρ , and moving with a velocity \mathbf{v} the total energy E can be written as:

$$E = m(\hat{u} + \frac{1}{2}\mathbf{v} \cdot \mathbf{v}) \quad (4.11)$$

where \hat{u} is the internal energy per unit mass. The first law of thermodynamic states that the rate of change of the total energy of the material volume is equal to the rate of heat addition and work extraction through its boundaries:

$$\left(\frac{dE}{dt}\right)_{MV} = \dot{Q} - \dot{W}. \quad (4.12)$$

The net rate of heat transferred to the material element \dot{Q} is the sum of two components. The first component is the rate transferred across the surface of the element \dot{Q}_S and the second generated/destroyed (e.g., due to a chemical reaction) within the material volume \dot{Q}_V . Moreover, the net rate of work done by the material volume \dot{W} is due to the rate of work done by the surface forces \dot{W}_S and the rate of work done by the body forces \dot{W}_b . Thus the first law can be written as:

$$\left(\frac{dE}{dt}\right)_{MV} = \dot{Q}_V + \dot{Q}_S - \dot{W}_b - \dot{W}_s \quad (4.13)$$

By definition, work is due to a force acting through a distance and power is the rate at which work is done. Therefore, the rate of work done by body and surface forces can be represented by:

$$\dot{W}_b = - \int_V (\mathbf{f}_b \cdot \mathbf{v}) dV \quad (4.14)$$

$$\dot{W}_S = - \int_S (\mathbf{f}_S \cdot \mathbf{v}) dS \quad (4.15)$$

The rate of work due to surface forces can be expanded by replacing \mathbf{f}_S by its equivalent expression as given in Eq. (4.4) through (4.6). This leads to:

$$\dot{W}_S = - \int_S [\boldsymbol{\sigma} \cdot \mathbf{v}] \cdot \mathbf{n} dS = \int_V \nabla \cdot [\boldsymbol{\sigma} \cdot \mathbf{v}] dV = - \int_V \nabla \cdot [(-p\mathbf{I} + \boldsymbol{\tau}) \cdot \mathbf{v}] dV \quad (4.16)$$

After manipulation, \hat{W}_S can be written as:

$$\dot{W}_S = - \int_V (-\nabla \cdot [p\mathbf{v}] + \nabla \cdot [\boldsymbol{\tau} \cdot \mathbf{v}]) dV \quad (4.17)$$

If q_V represents the rate of heat source or sink within the material volume per unit volume and q_S the rate of heat transfer per unit area across the surface area of material element, then \dot{Q}_V and \dot{Q}_S can be written as:

$$\begin{aligned} \dot{Q}_V &= \int_V q_V dV \\ \dot{Q}_S &= \int_V \nabla \cdot q_S dV \end{aligned} \quad (4.18)$$

Applying the Reynolds transport theorem and substituting the rate of work and heat terms by their equivalent expressions, Eq.(??) becomes:

$$\begin{aligned} \left(\frac{dE}{dt}\right)_{MV} &= \int_V \frac{\partial(\rho e)}{\partial t} + \nabla \cdot [\rho \mathbf{v} e] dV \\ &= - \int_V \nabla \cdot \dot{q}_S dV + \int_V (-\nabla \cdot [p\mathbf{v}] + \nabla \cdot [\boldsymbol{\tau} \cdot \mathbf{v}]) dV + \int_V (\mathbf{f}_b \cdot \mathbf{v}) dV + \int_V \dot{q}_V dV \end{aligned} \quad (4.19)$$

Collecting terms together and considering that the integrand has to be zero, the equation is:

$$\frac{\partial(\rho e)}{\partial t} + \nabla \cdot [\rho \mathbf{v} e] = -\nabla \cdot \dot{q}_S + (\nabla \cdot [p\mathbf{v}] + \nabla \cdot [\boldsymbol{\tau} \cdot \mathbf{v}]) + (\mathbf{f}_b \cdot \mathbf{v}) + \dot{q}_V \quad (4.20)$$

which represents the mathematical description of energy conservation or simply the energy equation written in terms of specific total energy. The energy equation may also be written in terms of specific internal energy, specific static enthalpy (or simply specific enthalpy), specific total enthalpy, and under special conditions in terms of temperature [27].

4.2 Turbulence modelling

Most of turbulence industrial applications involve turbulent flows. However a precise definition is somewhat difficult and all that can be done is a brief outline of some of its characteristics [30]. One characteristic is the irregularity, or randomness, of all turbulent flows. This makes a deterministic approach to problems including turbulence impossible; instead, statistical methods have to be relied on. Another important turbulence feature is its diffusivity that leads to rapid mixing, thereby increasing transfer rates of momentum, heat and mass through the flow domain. Turbulent flows usually occur at large Re number, and often originate as the instability of laminar flows with increasing Reynolds numbers. Instabilities are related to the interaction of viscous terms and nonlinear inertia terms in the equations of motion. Turbulence is a 3-D phenomenon and there are no satisfactory 2-D approximations for determining fine details of turbulent flows; all turbulent flows are inherently dissipative and turbulence characterized by a cascade process, whereby there is energy transfer from larger ones to smaller eddies and the latter dissipate mechanical energy into heat due to molecular viscosity. Turbulence is a

continuum phenomenon governed by the equations of fluid mechanics. Even the smallest scales in any turbulent flow are much larger than any molecular length scale. Finally, turbulence is a flow feature, and not a fluid feature. It is possible to estimate the scale of the smallest eddies through dimensional analysis. As stated above the cascade process involves a transfer of turbulent kinetic energy k (associated to fluctuating turbulent velocity) from larger eddies to smaller ones. The smallest eddies should be in a state where the rate of receiving energy from larger eddies is very nearly equal to the rate at which the smallest eddies dissipate the energy to heat [31]. Hence the motion at the smallest scales should depend only upon the rate at which the larger eddies supply energy, $\epsilon = -\frac{dk}{dt}$ and the kinematic viscosity ν . Having established appropriate dimensional quantities for ϵ and ν one can derive *Kolmogorov* scales of length, time and velocity:

$$\begin{aligned}\eta &= \left(\frac{\nu^3}{\epsilon}\right)^{\frac{1}{4}} \\ \tau &= \left(\frac{\nu}{\epsilon}\right)^{\frac{1}{2}} \\ v &= (\nu\epsilon)^{\frac{1}{4}}.\end{aligned}$$

With dimensional analysis the dissipation rate ϵ could be related with k through:

$$\epsilon \sim \frac{k^{\frac{2}{3}}}{l}$$

where l is the integral length scale of the largest eddies. Hence the ratio:

$$\frac{l}{\eta} \sim Re_t^{\frac{3}{4}}$$

with Re_t being the turbulence Reynolds number based on l and k . Thus, the energy cascade involves a number of scales proportional to N :

$$N = Re_t^{\frac{9}{4}}.$$

It is now clear that in order to ensure that all the features of turbulence are predicted correctly, a large computational domain and a very dense grid are requested. This is a *DNS* (direct numerical simulation) approach and it is not affordable for industrial applications because of the need to obtain results within a reasonable time and because of the great request of computational resources. Hence a mathematical model is required to predict turbulent flow properties but

modelling turbulence involves statistical studies of the equations of fluid flow and always leads to the closure problem: more unknowns than equations. In order to make the number of equations equal to the number of unknowns, assumptions are imperative. Usually there are two approaches: filtering in space or averaging in time. The first approach called *LES* (large eddy simulation) consists on applying a spatial filter to Navier Stokes equations with only the length scales smaller than the size of the filter modelled. Nevertheless, nowadays time averaging is still the most common turbulence model approach in industrial applications and all turbulent fluctuations need to be modelled. The key approach is to decompose the flow variables into a time-mean value component and a fluctuating one, substituting in the original equations, and time-averaging the obtained equations. Expressing the instantaneous velocity as the sum of a mean and a fluctuating part so that:

$$\mathbf{v}(\mathbf{x}, t) = \bar{\mathbf{v}}(\mathbf{x}) + \mathbf{v}'(\mathbf{x}, t). \quad (4.21)$$

The time-averaging leads to the following expression for the incompressible *RANS* continuity, momentum, energy equations:

$$\nabla \cdot (\rho \bar{\mathbf{v}}) = 0 \quad (4.22)$$

$$\frac{\partial \rho \bar{\mathbf{v}}}{\partial t} + \nabla \cdot \{\rho \bar{\mathbf{v}} \bar{\mathbf{v}}\} = -\nabla \bar{p} + \nabla \cdot (\bar{\tau} - \rho \overline{\mathbf{v}' \mathbf{v}'}) + \rho \mathbf{g} \quad (4.23)$$

$$\frac{\partial (\rho c_p \bar{T})}{\partial t} + \nabla \cdot (\rho c_p \bar{\mathbf{v}} \bar{T}) = \nabla \cdot (k \nabla \bar{T} - \rho c_p \overline{\mathbf{v}' T'}) + \bar{S}^T \quad (4.24)$$

Keeping the unsteady term $\frac{\partial \rho \bar{\mathbf{v}}}{\partial t}$ in the momentum equation usually brings to the definitions of *URANS* (unsteady Reynolds averaged Navier-Stokes), but attention should be maintained for those turbulent flows where there is no clear distinction between timescale characteristic of slow variation of the mean flow and that related to turbulent fluctuations. Indeed, the approximation:

$$\frac{\partial \mathbf{v}(\mathbf{x}, t)}{\partial t} \approx \frac{\partial \bar{\mathbf{v}}(\mathbf{x})}{\partial t}, \quad (4.25)$$

is true if $|\mathbf{v}'| \ll |\bar{\mathbf{v}}|$. This is always questionable, however using time averaging in this manner is useful for analysis especially for time marching numerical methods implemented for solving fluid dynamics problems but a degree of caution must be exercised when fluctuations are not too small. Comparing Eq. (4.23) with Eq. (4.7) and the Incompressible Energy equation with Eq. (4.24), one can note

the appearance of new terms on the right-hand side. These terms are called *Reynolds Stresses* and *turbulent heat fluxes*. So what Reynolds-averaging does is to introduce 9 new variables (Reynolds averaged Navier-Stokes) equations, and therefore additional equations are required.

Here comes into play the *Boussinesq hypothesis*, which makes an analogy with Newtonian fluids by assuming that the *Reynolds stresses* are a linear function of the *mean velocity gradients*:

$$-\overline{\rho \mathbf{v}' \mathbf{v}'} = \mu_T [\nabla \mathbf{v} + (\nabla \mathbf{v})^T] - \frac{2}{3} \rho k \mathbf{I}. \quad (4.26)$$

This assumption reduces the number of unknown from 6 to 2: the *turbulent eddy viscosity* μ_T and the *turbulent kinetic energy* k .

For incompressible flows, the equations can be rearranged by defining a *turbulent pressure* p [27]:

$$p \longleftarrow p + \frac{2}{3} \rho k.$$

In this manner, the only unknown that remains to compute is the *turbulent eddy viscosity* μ_T . The great variety of existing turbulence models derive from different ways of evaluating μ_T . In a similar way, the turbulent thermal fluxes are calculated in analogy with Fourier's law such that:

$$-\rho c_p \overline{\mathbf{v}' T'} = \alpha_t, \quad (4.27)$$

where α_t is the turbulent thermal diffusivity. In the following section the Standard $k - \epsilon$ model is presented, the mathematical model most commonly used model in computational fluid dynamics to simulate the average flow characteristics in turbulent conditions.

4.3 Standard $k - \epsilon$ model

This turbulence model involves the resolution of two additional partial differential equations, in order to locally compute the *turbulent eddy viscosity* μ_T and the *turbulent thermal diffusivity* α_T . Like others models based on the *Boussinesq hypothesis*, the $k - \epsilon$ model is based on the following expressions for *turbulent eddy viscosity* μ_T and for turbulent thermal diffusivity α_T :

$$\mu_t = \rho C_\mu \frac{k^2}{\epsilon}$$

$$\alpha_t = c_p \frac{\mu_t}{P_r}$$

where C_μ is a calibration constant, k is the *turbulent kinetic energy* and ϵ is the *rate of dissipation of turbulent kinetic energy per unit mass due to viscous stresses*. Solving the following transport equations for k and ϵ a local value of μ_t can be computed:

$$\frac{\partial(\rho k)}{\partial t} + \nabla \cdot (\rho \mathbf{v} k) = \nabla \cdot \left(\left(\mu + \frac{\mu_T}{\sigma_k} \right) \nabla k \right) + \underbrace{[P_k - \rho \epsilon]}_{S_k}. \quad (4.28)$$

$$\frac{\partial(\rho \epsilon)}{\partial t} + \nabla \cdot (\rho \mathbf{v} \epsilon) = \nabla \cdot \left(\left(\mu + \frac{\mu_T}{\sigma_k} \right) \nabla \epsilon \right) + \underbrace{\left[C_{\epsilon 1} \frac{\epsilon}{k} P_k - C_{\epsilon 2} \rho \frac{\epsilon^2}{k} \right]}_{S_\epsilon}. \quad (4.29)$$

where (P_r) is the turbulent and the compact form of the production of turbulent energy is given by:

$$P_k = \boldsymbol{\tau}^R : \nabla \mathbf{v}$$

It must be kept in mind that the construction of this model is based on two important assumptions:

- *fully turbulent flow;*
- *negligible molecular viscosity effects.*

This establishes the limits of this approach:

- *validity only for high values of the Reynolds;*
- *inability to reach the wall.*

To account for this lack the so-called *low Reynolds k - ϵ* models have also been developed. These models use damping functions to damp the turbulent viscosity while getting close to the wall.

4.4 Near wall treatment

On every solid surface, due to the fluid viscosity, a boundary layer develops. This layer of fluid can be divided in three regions:

- *viscous sub-layer* ($0 < y^+ < 5$), where the effect of viscosity dominates;
- *buffer sub-layer* ($5 < y^+ < 30$), where viscous and inertial effects are equal;
- *inertial (log-law) sub layer* ($30 < y^+ < 500$), where the effect of inertia dominates.

These three sub-layers can be identified by the value of y^+ that is the dimensionless normal distance (d_{\perp}) from the wall:

$$y^+ = \frac{d_{\perp} u_{\tau}}{\nu}, \quad (4.30)$$

where $u_{\tau} = \sqrt{\tau_{\omega}/\rho}$ is the velocity scale.

This subdivision of the boundary layer is schematized in *Figure 5.1*

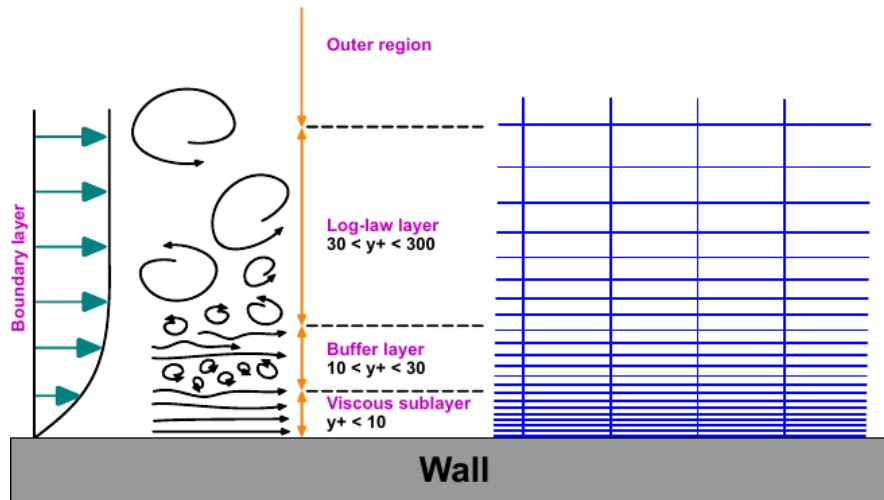


Figure 4.1: *Boundary layer subdivision and correspondent y^+ ranges (courtesy of Wolf-Dynamics srl [32])*

Turbulence models avoid the *buffer sub-layer*, because the high turbulent production, by placing the first cell center in the *viscous sub-layer* or in the *inertial sub-layer*.

The first option leads to accurate prediction of the boundary layer, but requires a very fine discretization near the wall, usually leading to unaffordable costs.

The second, combined by the definition an appropriate wall-value to each new variable introduced, significantly reduces computational costs while giving a good

accuracy. This velocity profile is called *wall function* and its action is schematized in *Figure 5.2*.

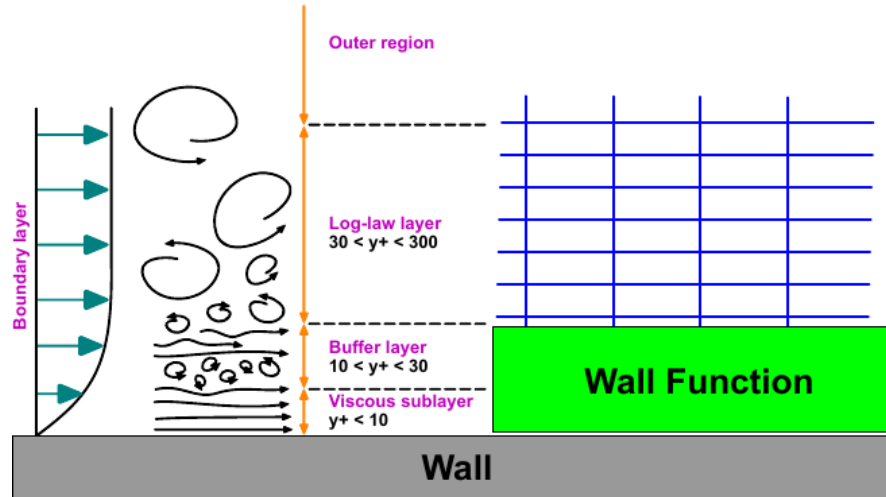


Figure 4.2: Representation of the wall function approach. (courtesy of Wolf-Dynamics srl [32])

4.5 The Finite Volume Method

The Finite Volume Method (FVM) is the standard approach used in most commercial codes for CFD. The equations are solved in a discrete control volume (cell). The typical approach requires to discretize the fluid domain in elementary cells in order to obtain a computational grid (also called mesh), on which to apply iterative resolution methods in order to solve the Navier-Stokes equations or the Euler equations.

In detail, FVM is a numerical technique that transforms the partial differential equations representing conservation laws over differential volumes into discrete algebraic equations over finite volumes (or elements or cells). In a similar fashion to the finite difference or finite element method, the first step in the solution process is the discretization of the geometric domain, which, in the FVM, is discretized into non-overlapping elements or finite volumes. The partial differential equations are then discretized/transformed into algebraic equations by integrating them over each discrete element. The system of algebraic equations is then solved to compute the values of the dependent variable for each of the elements [27].

Discretization of the solution domain produces a computational mesh on which the governing equations are solved (mesh generation stage). It also determines the positions of points in space and time where the solution will be computed. The procedure can be split into two parts: temporal discretization and spatial discretization. The temporal solution is simple obtained by marching in time from the prescribed initial conditions. For the discretization of time, it is therefore necessary to prescribe the size of the time-step that will be used during the calculation. The spatial discretization of the solution domain of the FVM method presented in this manuscript, requires a subdivision of the continuous domain into a finite number of discrete arbitrary control volume. In our discussion, the control volumes do not overlap, have a positive finite volume and completely fill the computational domain. Finally, all variables are computed at the centroid of the control volumes (collocated arrangement).

A typical control volume is shown in *Figure 4.3* In this figure, the control volume V_P is bounded by a set of flat faces and each face is shared with only one neighboring control volume. The shape of the control volume is not important for our discussion, for our purposes it is a general polyhedron. The control volume faces in the discrete domain can be divided into two groups, namely; internal faces (between two control volumes) and boundary faces, which coincide with the boundaries of the domain. The face area vector S_f is constructed for each face in such a way that it points outwards from the control volume, is located at the face centroid, is normal to the face and has a magnitude equal to the area of the face (e.g., the shaded face in *Figure 4.3*). Boundary face area vectors point outwards from the computational domain. In *Figure 4.3*, the point P represents the centroid of the control volume V_P and the point N represents the centroid of the neighbor control volume V_N . The distance between the point P and the point N is given by the vector \mathbf{d} . For simplicity, all faces of the control volume will be marked with f , which also denotes the face centroid [33].

For more detailed information about it we recommend the work of J.Guerrero *et al.* [33].

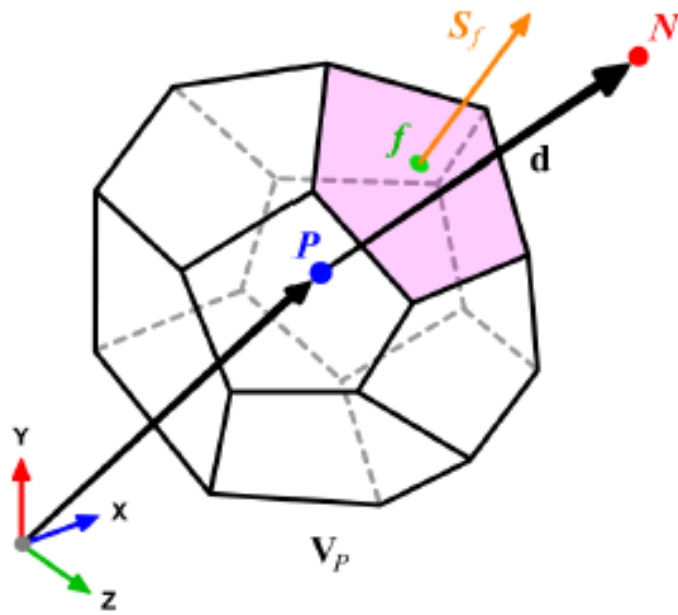


Figure 4.3: Arbitrary polyhedral control volume V_P . The control volume has a volume V and is constructed around a point P (control volume centroid), therefore the notation V_P . The vector from the centroid of the control volume V_P (point P), to the centroid of the neighboring control volume V_N (point N), is defined as \mathbf{d} . The face area vector S_f points outwards from the surface bounding V_P and is normal to the face. The control volume faces are labeled as \mathbf{f} , which also denotes the face center. [33])

Chapter 5

Simulations of the flow field

Following the 3D geometry created above, the aim of the simulation was to characterize the fluid velocity near the surface of the eye due to a person walking. Several cases were run in order to investigate the influence of different flow inlet velocities and turbulence parameters, as well as the fluid dynamic role of the eyelashes. Moreover we analyzed how protection devices can modify the flow on the eye, according to the size. To keep the computational cost of the simulation that is not too onerous and to start with a simple simulation, circular lenses were chosen as protection devices and the dimensions were parameterized as a function of the diameter.

For the study of mesh convergence three different cases were evaluated based on the number of cells called: *case0*, *case1*, *case2*. For the study of flow characteristics different cases were evaluated based on turbulence, intensity and presence or absence of eye protection devices; all of these cases will be described in the sections below.

The preliminary work therefore consists in generating a velocity field for each situation to be simulated; the limitations to be taken into consideration in the model are certainly the fact that the constructed geometric model does not correspond to a real model but is simplified. For this reason, the flows that will be generated will be evaluated as suitable for the model and not for a real case in which the presence of an eye with a three-dimensional spherical shape, nose, or in general, should also be taken into consideration. a real face. Furthermore, the turbulence model has been chosen to have a base case, which does not lead to the formation of major turbulence and vortexes within the model.

The following sections briefly describe the mesh generation process, the grid

convergence, the velocity fields of the cases of study and the results obtained.

5.1 Mesh generation

Mesh generation has been carried out with two OPENFOAM[®] utilities: *blockMesh* and *snappyHexMesh* that are controlled respectively the *blockMeshDict* and *snappyHexMeshDict* dictionaries. With *blockMesh*, the background mesh is obtained by decomposing user defined domain into a set of hexahedral blocks. The domain chosen is a parallelepiped that must contain the whole geometry. An OPENFOAM[®] utility called *surfaceCheck* suggests the proper coordinates of the edges of the parallelepiped and the spatial discretization can be defined by the user. Once the background mesh is obtained the *snappyHexMesh* utility generates the actual mesh containing hexahedra and split-hexahedra from the surface geometries. The first step in the meshing process is the cell splitting according to specification defined. Here the user can select several levels and types of refinement for different surfaces, volumes and also edges with the dedicated utility *SurfaceFeatureExtract*. Briefly, the next steps remove and snap the cells then add layers on walls if needed. During the process the mesh quality is controlled by the entries in the sub-dictionary *meshQualityControls*. After the meshing process is completed, the OPENFOAM[®] utility *checkMesh* will output the features of the mesh. The most important parameters for checking the quality of the mesh are:

- *Mesh orthogonality*: This parameter is related to angular deviation of the cell face normal vector from the vector connecting two consecutive cell centres. Non-orthogonality can lead to oscillatory solutions (unboundedness), which in turn can lead to nonphysical values. The higher the non-orthogonal angle (the angle between the face area vector \mathbf{S} and the vector \mathbf{d} in *Figure 5.1 (a)*), the higher the numerical diffusion, and this in fact reduces the accuracy of the numerical method [33]. Usually this parameter is kept below 75.
- *Mesh skewness*: Skewness is the deviation of the vector that connects two cell centres from the face centres. Skewness can be defined as the deviation of the face centroid f from the point where the vector \mathbf{d} intercepts the face. This situation is shown in *Figure 5.1 (b)*, where f is the face centroid, f_i is the point where the vector \mathbf{d} intersects the face f , and Δ_i is the vector that represents the deviation of f_i from f . Skewness adds numerical diffusion to

the solution and reduces the accuracy of the numerical method. It also leads to unboundedness, which in turn can conduct to nonphysical results and/or divergence of the solution [33]. Usually this parameter should be kept below 8.

- *Aspect Ratio*: Aspect Ratio AR is the ratio between the longest side Δx and the shortest side Δy of the cell. Large AR is good if gradients in the largest direction are small.

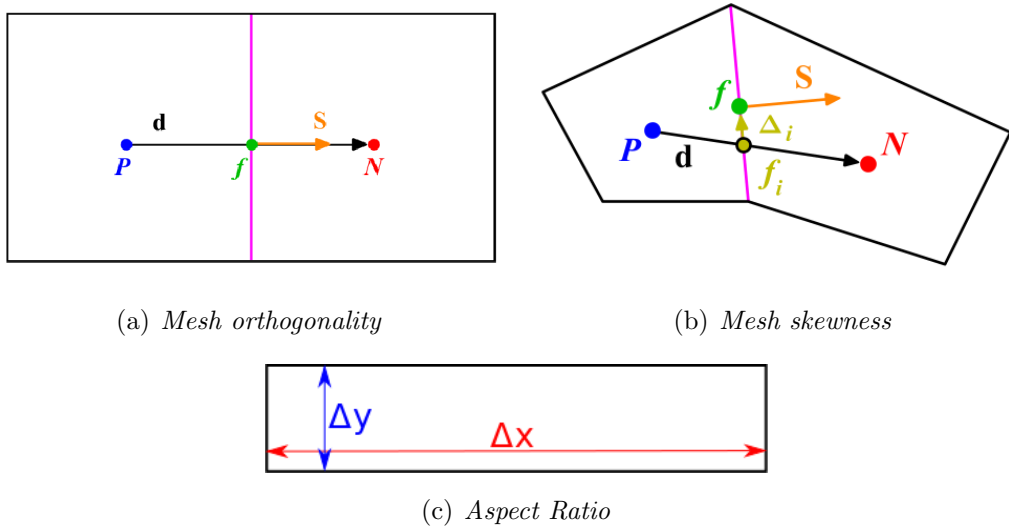


Figure 5.1: Main mesh quality parameters

As previously expressed, three different cases were evaluated based on the number of cells, in each mesh, in the directions x , y , z called; *case0*, *case1*, *case2*. In *Table 5.1* are shown the different number of cells in the three main directions. In *Table 5.2* are listed the main features of the two meshes.

Recalling the three experimental setups: *case0*, *case1*, *case2*, it is clear that three meshes have been made but the generating criteria were the same in all cases.

In *Table 5.2* are listed the main features of the two meshes.

	Mesh Case setup		
	<i>case0</i>	<i>case1</i>	<i>case2</i>
XCells	70	56	56
YCells	100	80	80
ZCells	150	100	100

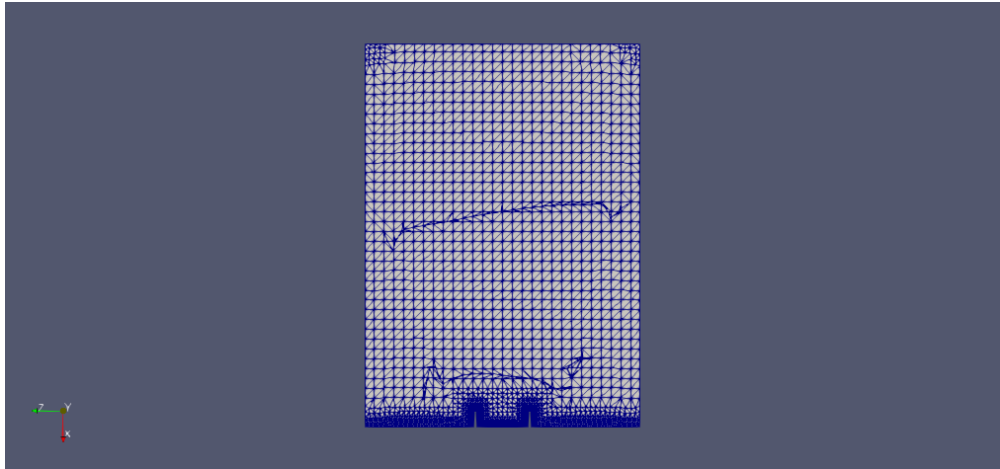
Table 5.1: *Mesh features*

Features	Mesh Case setup		
	<i>case0</i>	<i>case1</i>	<i>case2</i>
Cells	328485	651848	1497336
Faces per cell	6.283	6.289	6.239
HexaGedra	283339	584562	1369732
Prism	8974	906	1460
Pyramids	0	0	0
Tetrahedra	0	0	0
Polyhedra	36076	66252	125920
Non-orthogonality Max	38.739	37.531	37.774
Non-orthogonality Average	9.551	9.227	8.472
Max Skewness	1.002	3.220	2.986
Max <i>AR</i>	9.891	10.406	9.996

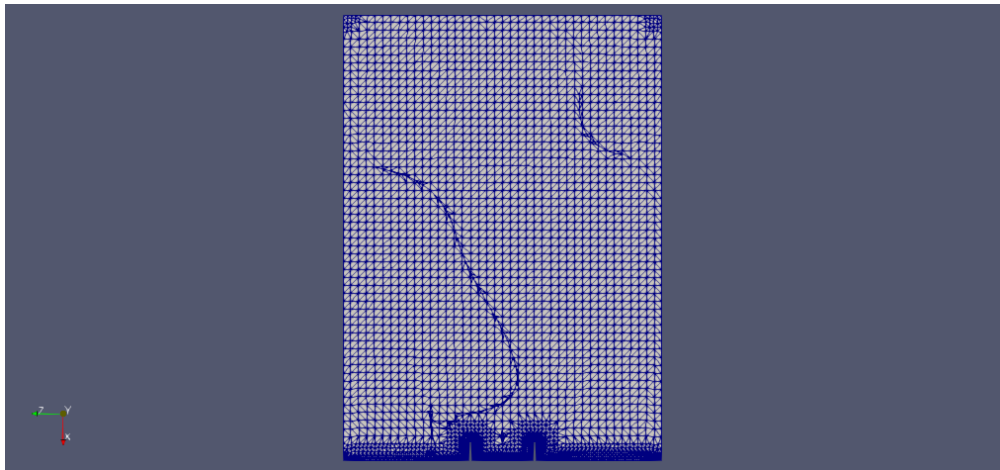
Table 5.2: *Mesh features*

In this part of the study we used these three meshes to analyze the flow behaviour without turbulence and with turbulence, however we decided to run simulations with the eye protection device and with the particles only with the mesh *case1*; despite this mesh doesn't have an large number of cells, it consent to avoid high computational efforts and to have consistent results. For this reason *snap-pyHexMeshDict* has been set up with low refinement in the domain while the eye and the eyelashes have been highly refined. In *Figure 5.2* the three meshes are visualized in a vertical plane section using the OPENFOAM[®] utility *paraView*. As can be seen in *Figure 5.2* well refined mesh regions has been created in close proximity to the eyelashes and the eye. The same evaluations could be made

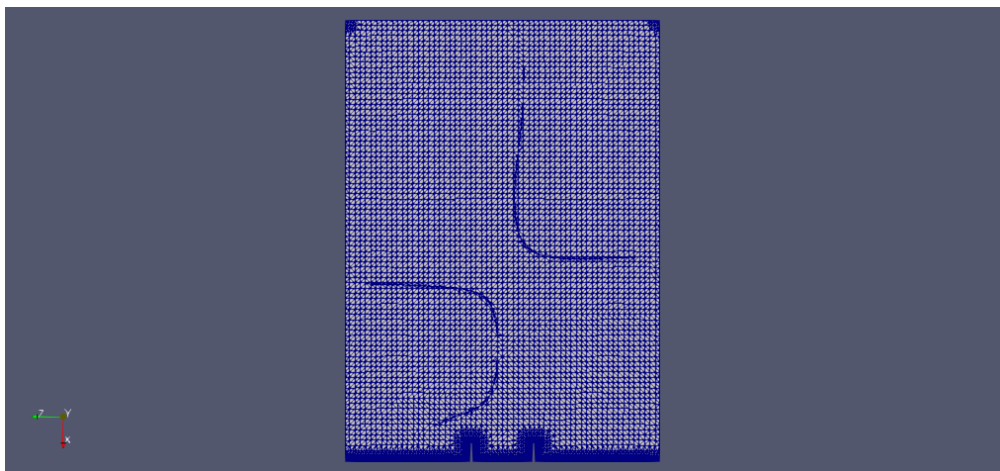
observing *Figure 5.3* in which is underlined the mesh next to the eye.



(a) *Mesh case0*

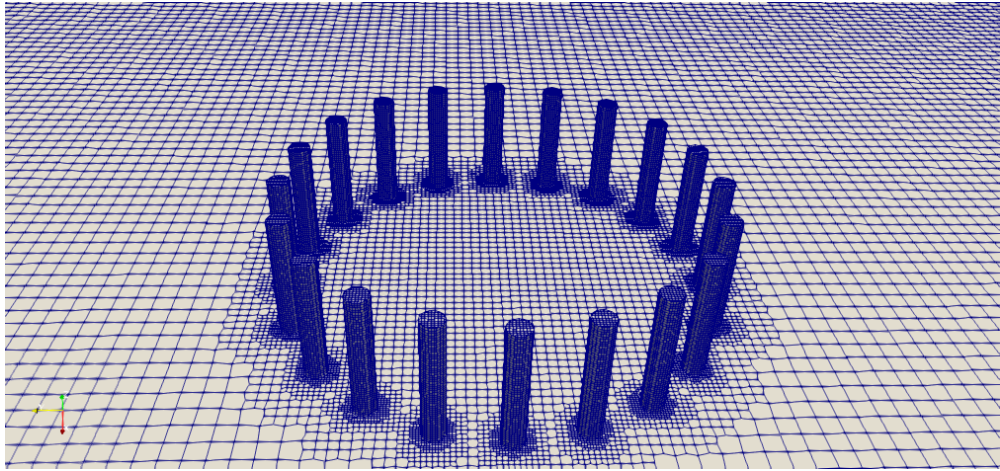


(b) *Mesh case1*

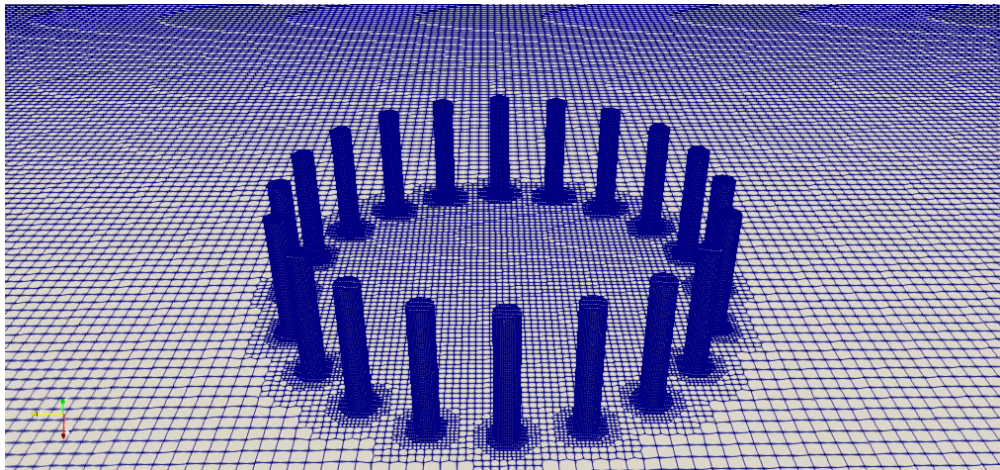


(c) *Mesh case2*

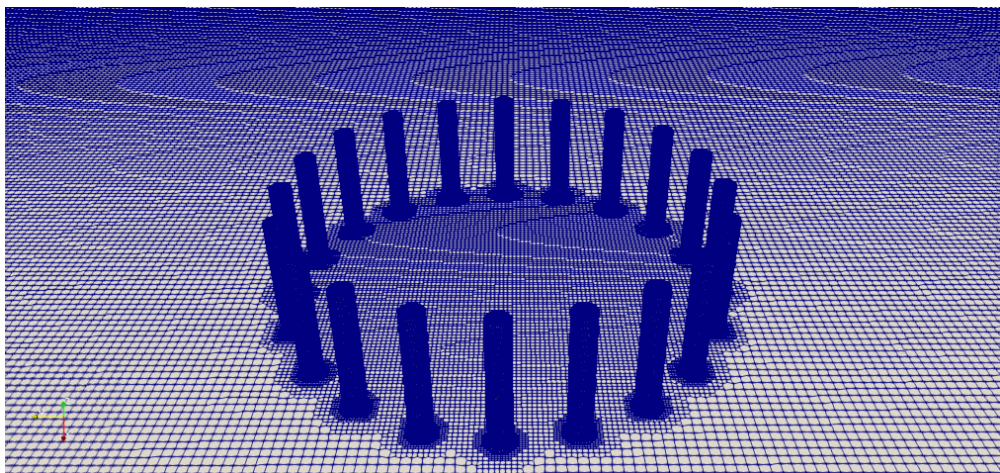
Figure 5.2: *Mesh vertical visualization with paraView*



(a) *Mesh case0*



(b) *Mesh case1*



(c) *Mesh case2*

Figure 5.3: *Mesh next to the eyelashes and eye with paraView*

5.1.1 Grid convergence

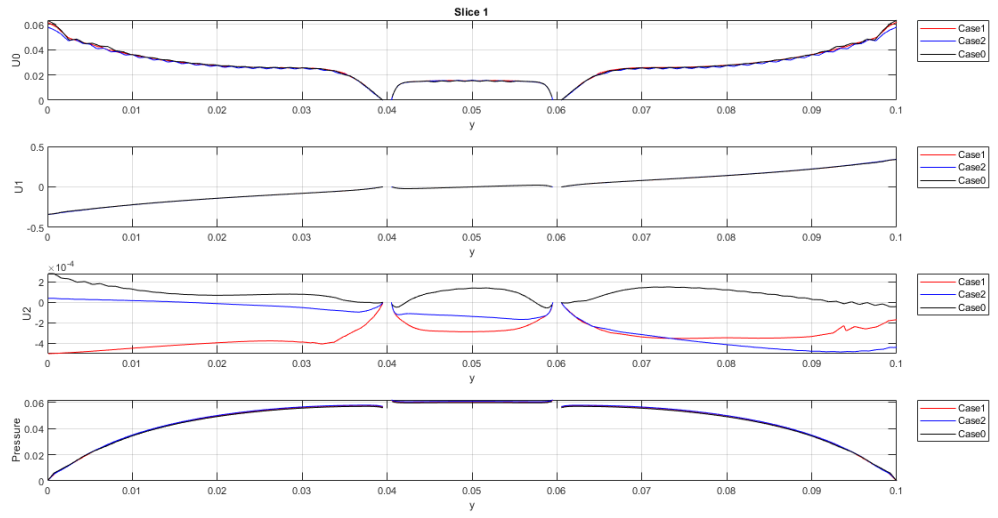
In finite volume modeling, a finer mesh typically produces a more accurate solution. However, when a mesh is refined, the time required for processing increases, so a mesh has been obtained that allows one to balance accuracy and processing resources by performing a mesh convergence study [34].

Following basic steps were required:

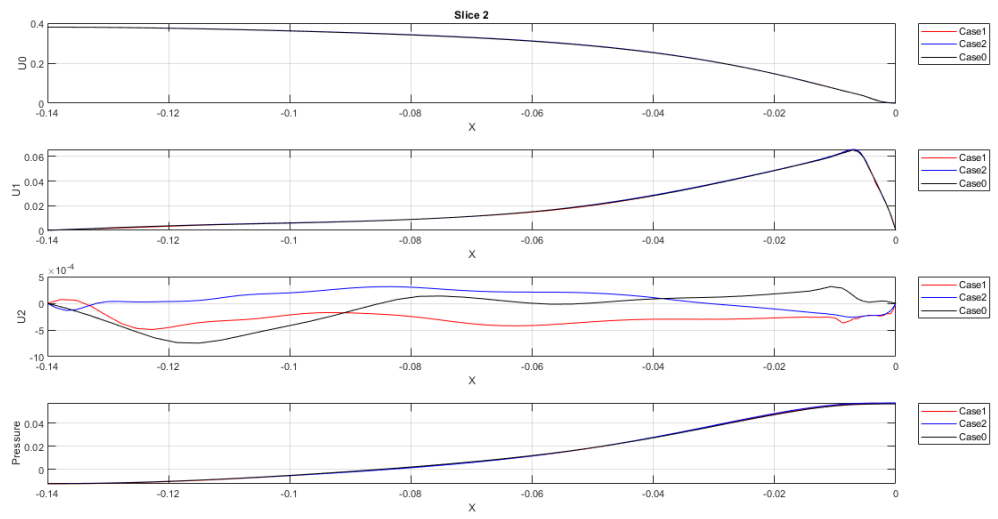
- Create a mesh using as few elements as possible and analyze the model
- Recreate the mesh with a denser element distribution, rerun the analysis and compare the results with those of the previous mesh
- Continue increasing the mesh density and re-analyzing the model until the results converge satisfactorily.

To analyze grid convergence we compared the three mesh models have been compared, *case0*, *case1*, *case2*. In particular, the value of U_0 , U_1 , U_2 , which are the velocity in x , y and z direction respectively and *pressure* were examined along two different slice directions; *Slice1* is on the y direction, *Slice2* is on the x direction.

In *Figure 5.4* the level of convergence in the form of an alignment is shown.



(a) Convergence plot Slice2



(b) Convergence plot Slice1

Figure 5.4: Convergence level in the form of an alignment

5.2 Case study

5.2.1 Case study A: Flow field for Atmospheric particulate

The first simulations concern the role that eyelashes play in protecting the ocular surface and the aim of this is to characterize the fluid velocity. To test this, two different flow field were evaluated: a first case in which a person is walking, a second case in which the person is running. The inlet velocity represented the walking/running was set at 1.11 m/s (=4 km/h) for walking and 4 m/s (=14.4 km/h) for running, as suggested by Blocken *et al.* [35]; The field of velocity generated in this work is shown in *Figure 5.5*.

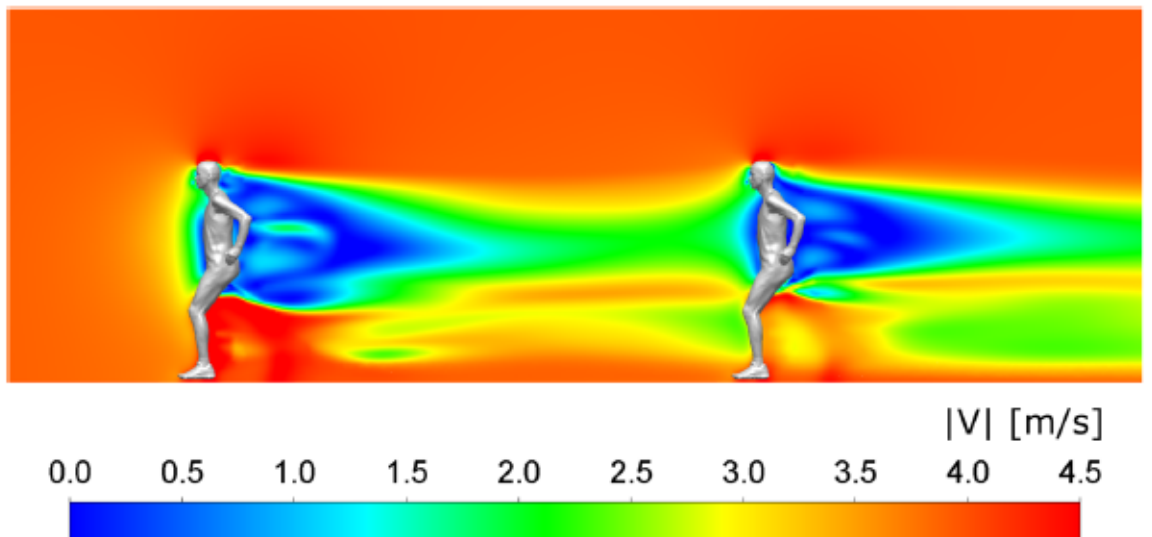


Figure 5.5: *Contours of air speed in the vertical centerplane when running at 4.5 m distance at 4 m/s taken from [35]*

The Reynolds Number for each case is given by $Re = \frac{UW}{\nu}$, where U is the inlet velocity, W the diameter of the eye and ν the kinematic viscosity.

To simulate a real situation, we chosen to use turbulent flow, with a $k - \epsilon$ model. The parameters of this model, which are calculated with *calculator for the estimation of turbulence properties* provided by Wolf Dynamics [32], are shown below:

- Turbulence intensity T_u : 1 %
- Turbulence length scale T_{uL} : 1 mm

- Turbulence kinetic energy k : $0.0000217 \text{ m}^2/\text{s}^2$
- Turbulence dissipation ϵ : $9.27\text{e-}7 \text{ m}^2/\text{s}^3$
- Kinematic viscosity ν : $1.5 \cdot 10^{-5} \text{ m}^2/\text{s}$

The goal of our work is to analyze a domain two orders of magnitude smaller than Blocken's work and concentrated in the area in front of the ocular surface, without taking into account the flows generated in a larger computational volume. The control volume used is that shown in the *Chapter 2*. Once the convergence mentioned in the previous section was demonstrated, *case1* was chosen as the default mesh for the simulations.

To evaluate the effect of the eyelashes on the deposition of particles, it is essential to carry out simulations with different geometries: for this reason, both for the walk case and for the run case we considered eye models without and with eyelashes; once the eyelashes were inserted in the geometry, they were parameterized by changing two parameters:

- Eyelashes length 5.8mm , 7.1mm , 9.0mm
- Number of Eyelashes: 20, 30, 40

Following the study by Amador *et al.* [1], two other parameters were evaluated:

- L/d ,
- S/d ,

where L is the length of the eyelashes, d their diameter (set at value $d = 1\text{mm}$), S the distance between them calculated as the distance between the center of each circumference on the arc of the circumference representing the eye..

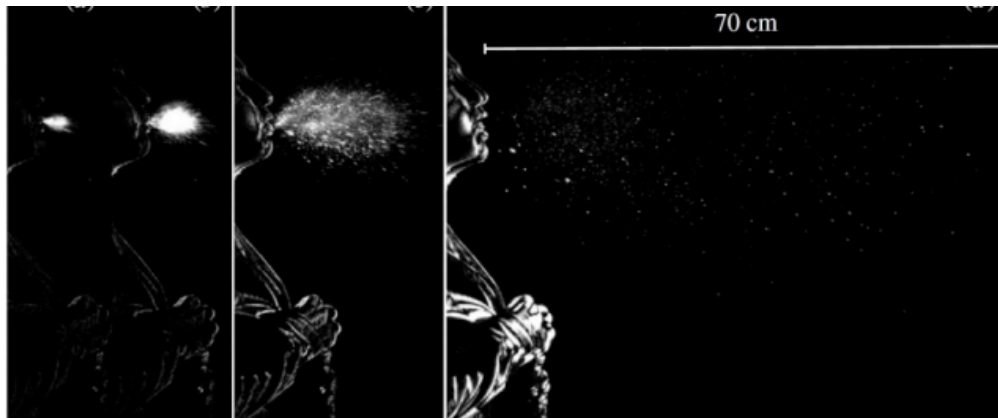
The *Table 5.3* below summarizes all the information presented; following the parameters previously evaluated, twenty simulations were carried out by linearly combining the lengths of the eyelashes with their number, emulating both the running situation and the walking situation.

Case	Parameters					
	L	N	V	Re	L/W	S/d
1. Walk	5.8	20	1.11	1470	0.29	3.12
2. Run	5.8	20	4	5298	0.29	3.12
3. Walk	7.1	20	1.11	1470	0.355	3.12
4. Run	7.1	20	4	5298	0.355	3.12
5. Walk	9.0	20	1.11	1470	0.45	3.12
6. Run	9.0	20	4	5298	0.45	3.12
7. Walk	//	//	1.11	1470	//	//
8. Run	//	//	4	5298	//	//
9. Walk	5.8	30	1.11	1470	0.29	2.09
10. Run	5.8	30	4	5298	0.29	2.09
11. Walk	7.1	30	1.11	1470	0.355	2.09
12. Run	7.1	30	4	5298	0.355	2.09
13. Walk	9.0	30	1.11	1470	0.45	2.09
14. Run	9.0	30	4	5298	0.45	2.09
15. Walk	5.8	40	1.11	1470	0.29	1.56
16. Run	5.8	40	4	5298	0.29	1.56
17. Walk	7.1	40	1.11	1470	0.355	1.56
18. Run	7.1	40	4	5298	0.355	1.56
19. Walk	9.0	40	1.11	1470	0.45	1.56
20. Run	9.0	40	4	5298	0.45	1.56

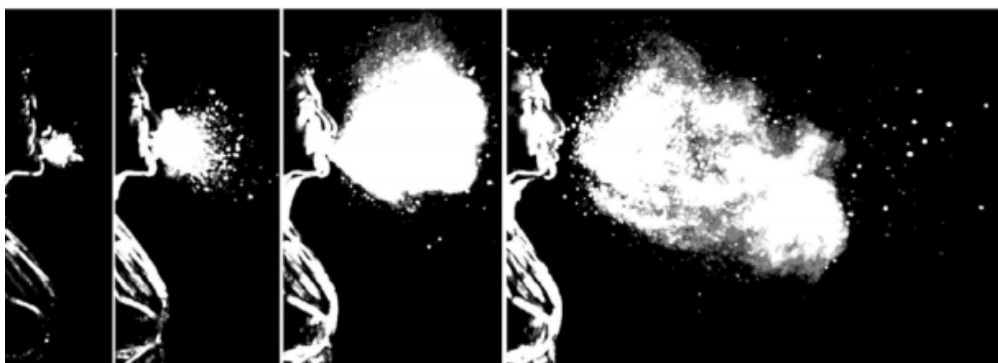
Table 5.3: *Simulations Case study A. Re = Reynolds Number, L =length mm, N =number of eyelashes, W =eye diameter, V =velocity m/s, d =diameter, S = distance center to center*

5.2.2 Case study B: Flow field for Droplets

The second set of simulations is concerned with the role of protective devices, such as a spectacle lens, in protecting the eye from any external agents or particles. For the purpose of the work and to analyze a situation of great scientific interest, it was chosen to generate velocity fields potentially generated by a cough and a sneeze: in fact, these two events are the ones that can later lead to the transport of saliva droplets potentially viral vectors of Sars-CoV-2 or other viruses. The 1- to 2-meter rule of spatial separation is central to droplet precautions and assumes that large droplets do not travel further than 2 meters; however, the work of Bahal *et al* [7] brings together several studies that show that this distance is not always sufficient to prevent droplets from finishing their path within that range of meters.



(a) Case Cough



(b) Case Sneeze

Figure 5.6: High speed images of a cough (a) and of a sneeze (b) recorded at 1000 frame per second [36]

Following these considerations, the choice of the set up of the velocity field has put together in parallel information from different studies to evaluate the initial velocity of the particles in cases in which one coughs and sneezes and the distance they reach;

- Maximum speed at the exit of the mouth in the sneeze case: $50m/s$ [37].
- Maximum speed at the exit of the mouth in the cough case: $10m/s$ [37].
- Maximum distance covered by droplets during coughing: $2m$ [38].
- Maximum distance covered by droplets during sneezing: $6m$ [38].

Putting this information together and considering that the droplet ejection events occur 2 meters away in the case of coughing and occurs 6 meters away in the case of sneezing and that the speed seems to decrease linearly during the journey, the input speed to the reference computational volume was chosen as $0.5m/s$ in the case of cough and $0.83m/s$; this means that in both cases the droplets will potentially reach on the surface of the eye.

As in the case study A, the Reynolds Number for each case is given by $Re = \frac{UW}{\nu}$, where U is the inlet velocity, W the diameter of the eye and ν the dynamic viscosity. To simulate a real situation, it was chosen not to use a laminar flow but turbulent, with a $k - \epsilon$ model. The parameters of this model, which are calculated with *calculator for the estimation of turbulence properties* provided by Wolf Dynamics [32], are shown below:

- Turbulence intensity T_u : 1 %
- Turbulence length scale T_{uL} : 1 mm
- Turbulence kinetic energy per unit mass k : $0.0000217 m^2/s^2$
- Turbulence dissipation ϵ : $9.27e-7 m^2/s^3$
- Kinematic viscosity ν : $1.5 \cdot 10^{-5} m^2/s$

To evaluate the effect of the glasses on the deposition of droplets, it is essential to carry out simulations with different geometries: for this reason, both for the sneezing and the coughing cases there are eye models without glasses and with circular glasses, with a diameter $d = 4cm$ and $d = 5cm$, and with a distance

between the surface of the eye and the lens of 2cm and a lens thickness of 3cm . In all cases evaluated, 20 eyelashes with length of 7.1mm were chosen.

The *Tabel 5.4* below summarizes all the information presented.

Case	Parameters				
	d	N	V	Re	L
1. Sneezing	4	20	0.83	1099	0.71
2. Coughing	4	20	0.5	662	0.71
3. Sneezing	5	20	0.83	1099	0.71
4. Coughing	5	20	0.5	662	0.71
5. Sneezing	//	20	0.83	1099	0.71
6. Coughing	//	20	0.5	662	0.71

Table 5.4: *Simulations Case study B. d =diameter of glasses (cm), N =number of eyelashes V =inlet velocity, L =length of eyelashes(cm)*

5.3 Results

Every simulation has been run with the same OPENFOAM[®] solver: *simpleFoam*, a steady-state solver for incompressible, turbulent flow. The solver settings in file called *fvSolution* and *fvSchemes* have been kept constant. The only exceptions are the relaxation factors that started from low values in order to avoid divergence of the solution. Successively after an adequate number of iterations the factors have been increased to standard values.

The post processing of the results about Case study A is made with ParaView and follows two basic ideas. For regarding cases the contours of velocity are visualized on two sections that cut the simulation domain. For the parametric analysis we plotted components of velocity, pressure, turbulent kinetic energy (k) and rate of dissipation of turbulent kinetic energy (ϵ) on different sections; these results are made with Matlab.

This section shows the results concerning a walk case, a run case with a number of lashes equal to 20 and a length of $5.8mm$, $7.1mm$, $9.0mm$; in fact, the differences in the velocity field for the other parameterized cases are irrelevant for the purposes of the study. However, the number of eyelashes and the length will be crucial in the simulations with the particles.

Furthermore, in this section we will show the same results explained previously, regarding Case study B, to evaluate the effect of glasses with diameters $d = 3cm$ and $d = 4cm$ on ocular surface protection. A parallel evaluation between Case study A and the latter will also be interesting to understand how different geometries in the computational volume can have different effects on the flow near the surface of the eye and on the energies involved.

5.3.1 Case study A

Walk and Run case with Eyelashes

The analysis of the results starts from the walk case so the actual setup presents an inlet velocity of $1.1m/s$ for walking and $4.0m/s$ for running. In *Figure 5.7* the magnitude of the velocity field is coloured with red for positive values tending to the maximum velocity, with blue for the values tending to the minimum velocity. The figure shows that the maximum magnitude value is in correspondence of the inlet of the domain and it tends to decrease along the x direction and close to

the eye and the eyelashes. It is clear that for both cases there are slight differences in terms of stream lines and the tendency of the flow is similar but there are only differences of magnitude velocity.

In *Figure 5.8* are shown the trends of the three components of speed and pressure along the slice in the y direction for a run case and a walk case; It is clear that the trends in both the run and walk cases are similar, with differences in amplitudes which are greater in the run case. In both cases the $U0$ velocity's component reaches the lowest values in correspondence of the eyelashes, and then stabilizes inside the ocular surface. The pressure P takes on complementary values to the velocity's component $U0$. Components of velocity $U1$ and $U2$ do not show relevant data.

In *Figure 5.9* are shown the trends of the three components of speed and pressure along the slice in the x direction for a run case and a walk case; it is clear that the components of velocity $U0$ and $U1$ tends to decrease moving from the inlet to the eye's surface. Also in this case there are differences in amplitudes which are greater in the run case and the pressure P takes on complementary values to the velocity's component $U0$. Components of velocity $U1$ and $U2$ do not show relevant data.

In *Figure 5.10* and *Figure 5.11* are shown the trends of the two main parameters of the turbulence: k and ϵ .

The differences in the lengths and number of eyelashes do not significantly affect the trends of speed, pressure and turbulence parameters; for this reason, the main parameter for evaluating the effect of the velocity field is the presence or absence of eyelashes and how they can divert the air flow.

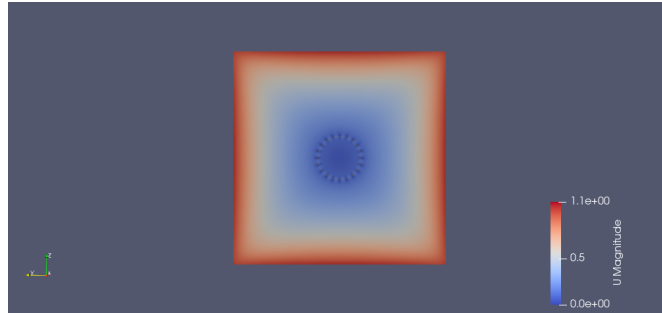
Comparison with the case without eyelashes

In order to evaluate the effect of the eyelashes on the velocity field, the simulation in the run case is explanatory; comparing the velocity components $U0$ and $U1$ in both Slice 1 and Slice 2, it is called how the absence of the cilia makes the flow almost symmetrical in the x direction, generating without undergoing a major change in the flow in y direction. Such modifications are appreciable in a similar way for the parameters k and ϵ .

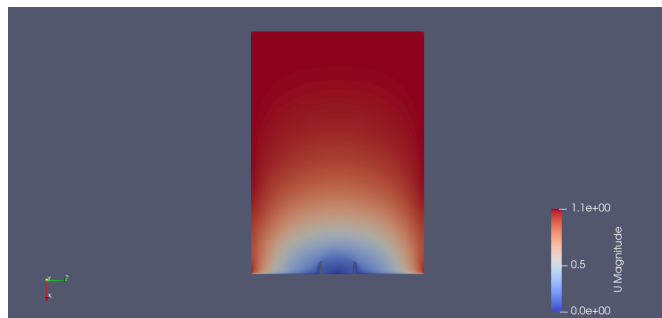
5.3.2 Case study B

The analysis of the results of Case study B starts from the sneezing case so the actual setup presents an inlet velocity of $0.83m/s$ for coughing and $0.5m/s$ for running. In *Figure 5.14* the magnitude of the velocity field is coloured with red for large values and with blue for the small values. The figure shows that the maximum magnitude value is in correspondence of the inlet of the domain and it tends to decrease along the y direction and close to the glasses and the eyelashes as shown in *Figures b* and *d*. It is clear that for both cases there are slight differences but overall flow characteristics are the same but there are only differences of magnitude and it is interesting to note how the presence of a protection device, in this case a circular lens, drastically decreases the flow generated by the velocity field in the area below the lens itself. The field of velocity without the lens is similar to that shown in *Figure 5.7* and it is useful to compare the two cases: in the absence of a lens, as expected, the air flow generated by the velocity field arrives on the ocular surface with greater intensity. In *Figure 5.15* the trends of the three velocity components and pressure along the slice are shown in the y direction for a sneezing and coughing case. It is clear that the trends in both cases are similar with differences in amplitudes which are greater in the sneezing case. In both cases the UO velocity's component reach the lowest values not in correspondence of the eyelashes but before them, due to the presence of the lens. It is interesting to compare the cases with and without lens in order to understand how the air flow velocity decrease in the y direction. The pressure P takes the complementary values to the velocity component UO . Also in these cases the components of velocity $U1$ and $U2$ don't show relevant data. The same comparisons can be made for Slice 2, as shown in *Figure 5.16*; also in this case it is possible to notice an important difference between the cases with the lens and the cases without the lens by evaluating a decrease of the speed component in the x direction.

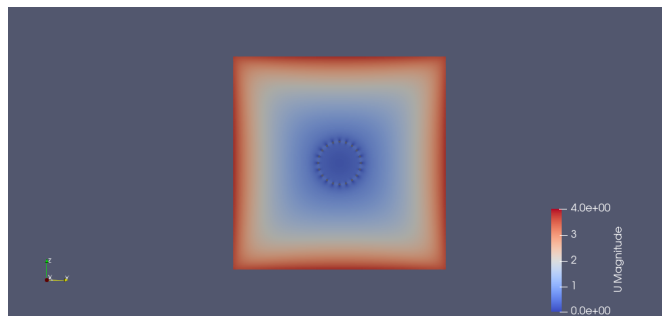
Following the considerations seen above, an evaluation of the *Figures 5.17* and *5.18* is interesting to notice that the kinetic energy k in cases with the lens decreases rapidly near the lens. This confirms the fact that the presence of the lenses also has positive effects in terms of kinetic energy on the ocular surface, decreasing it.



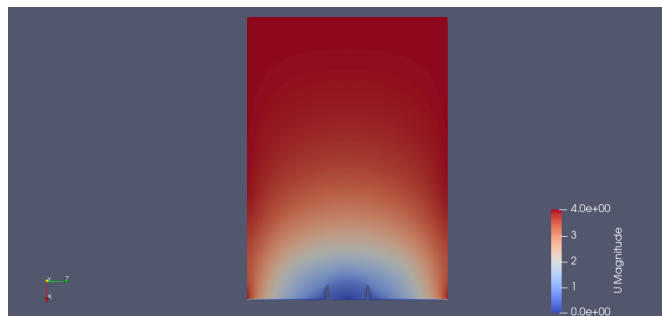
(a) *velocity Field WalkSlice1*



(b) *velocity Field Walk Slice2*

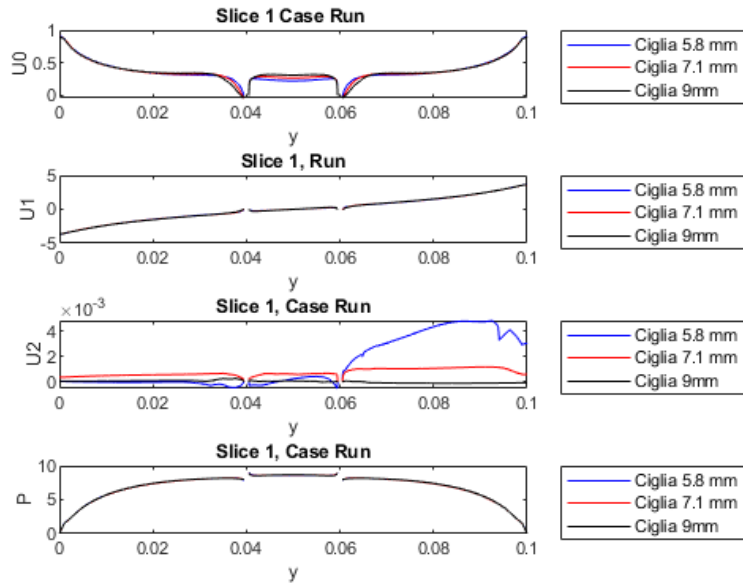


(c) *velocity Field Run Slice1*

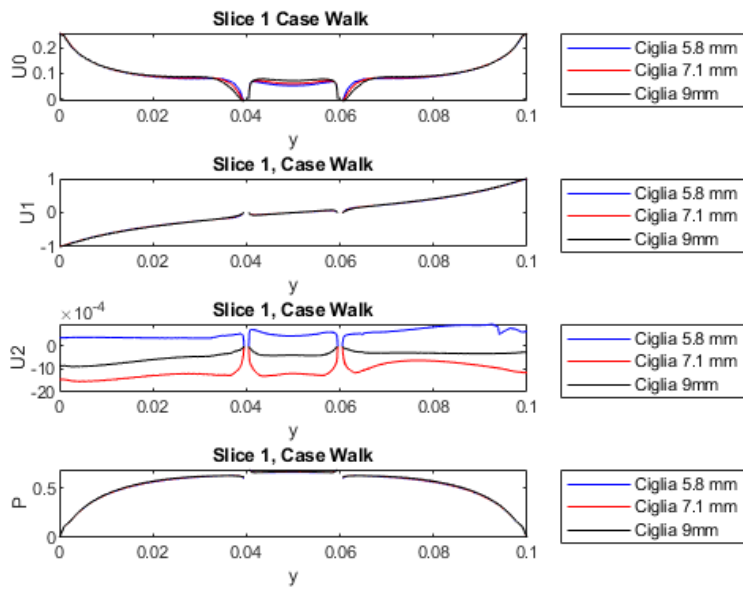


(d) *velocity Field Run Slice2*

Figure 5.7: *velocity field of the velocity magnitude on a horizontal (y -normal) and vertical (x -normal) section.*

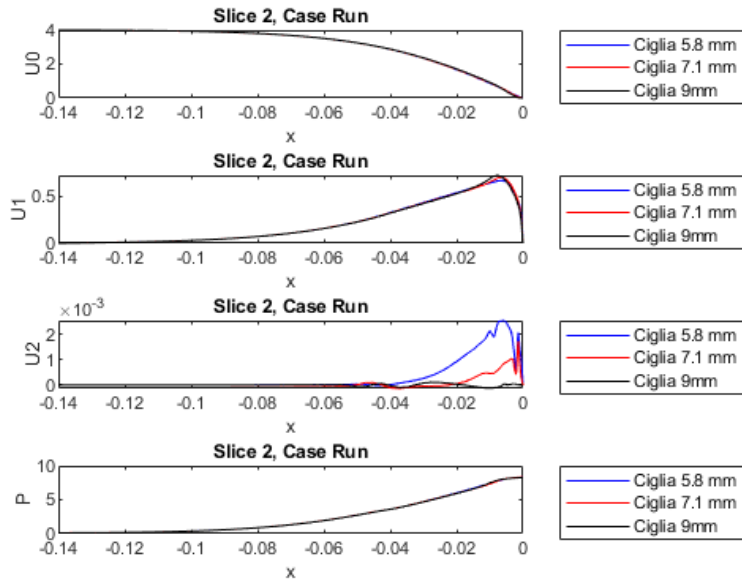


(a) U_0, U_1, U_2, P plot Slice1 case Run

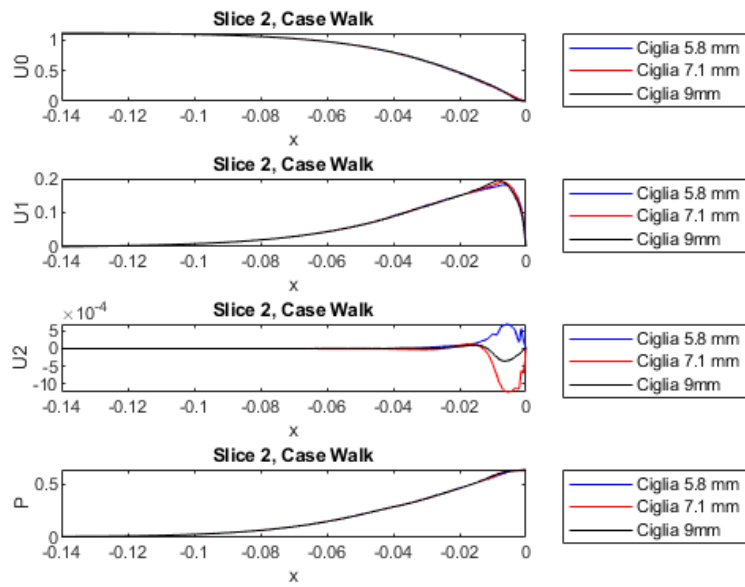


(b) U_0, U_1, U_2, P plot Slice1 case Walk

Figure 5.8: *Slice 1* plots.

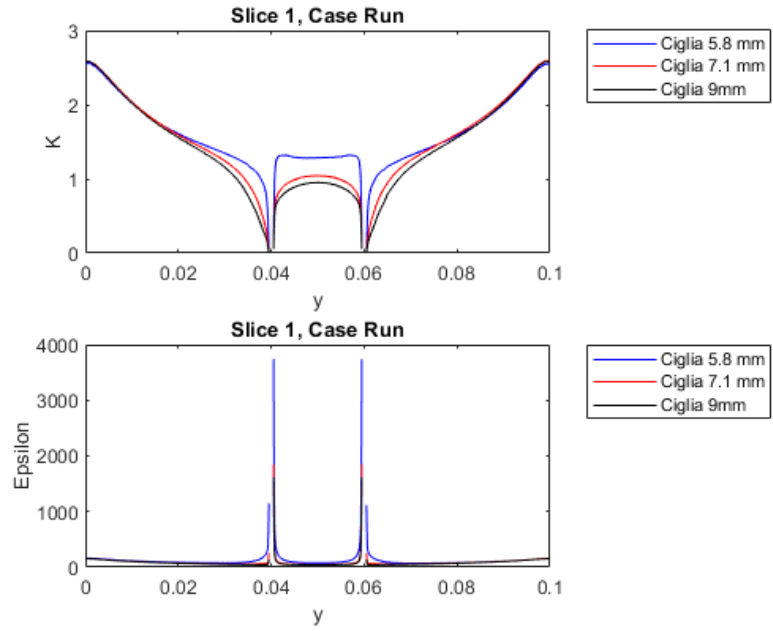


(a) U_0, U_1, U_2, P plot Slice1 case Run

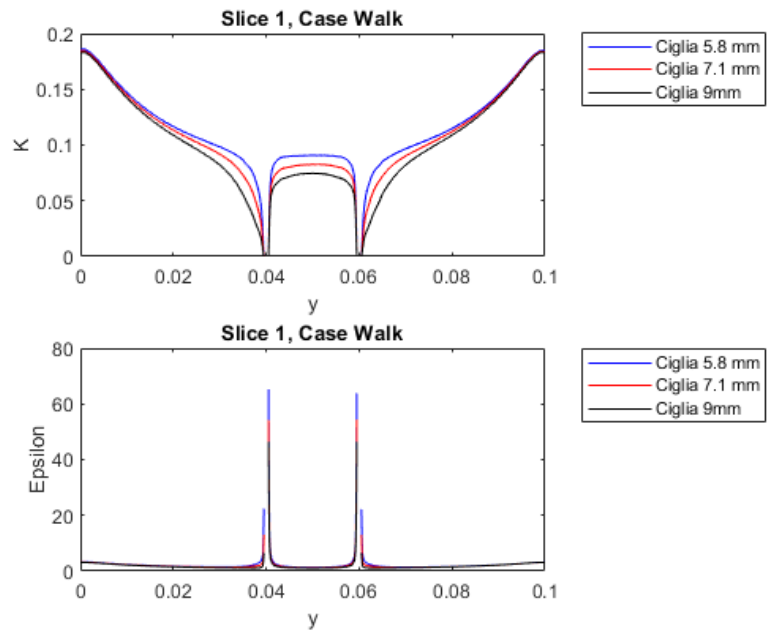


(b) U_0, U_1, U_2, P plot Slice2 case Walk

Figure 5.9: Slice 2 plots.

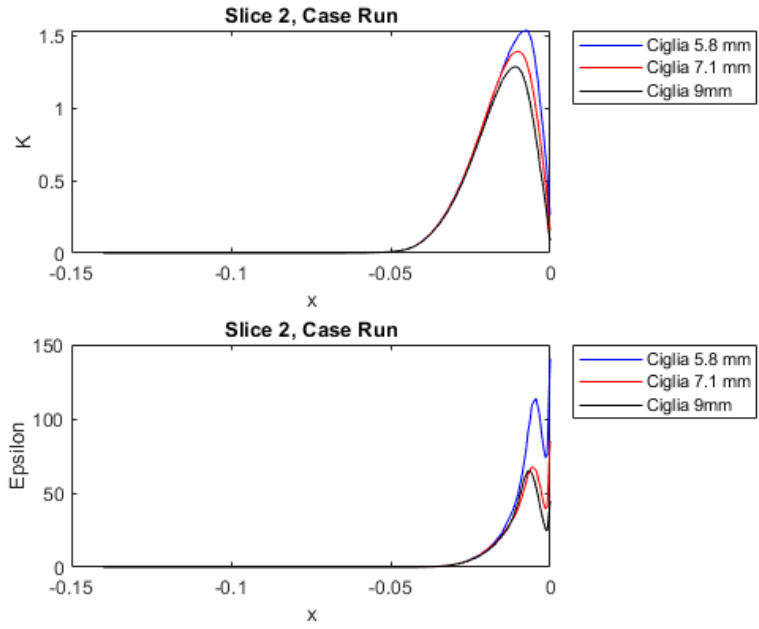


(a) $k \in \text{plotSlice1 case Run}$

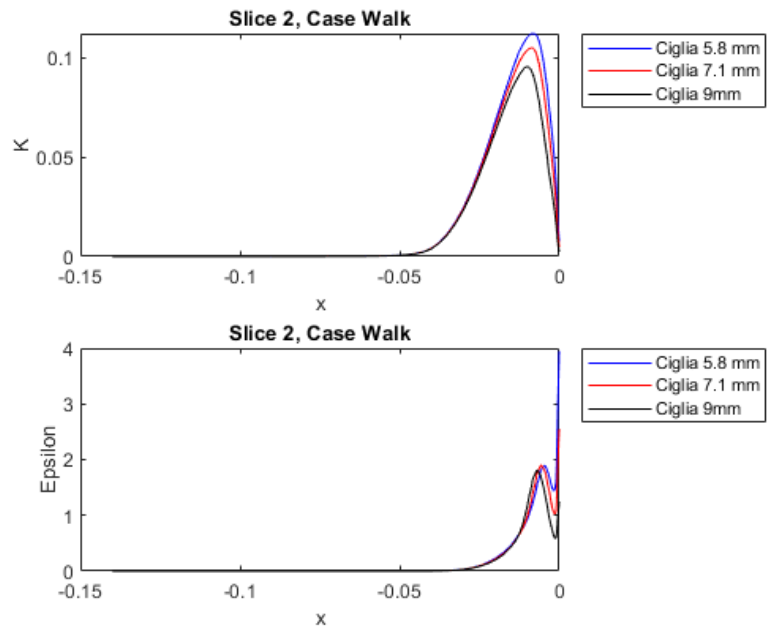


(b) $k \in \text{plot Slice1 case Walk}$

Figure 5.10: *Slice 1 plots.*

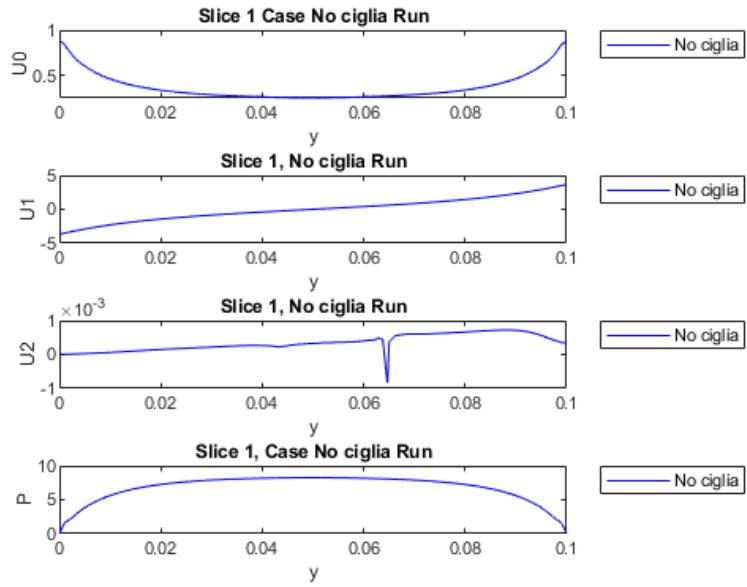


(a) $k \in \text{plotSlice2 case Run}$

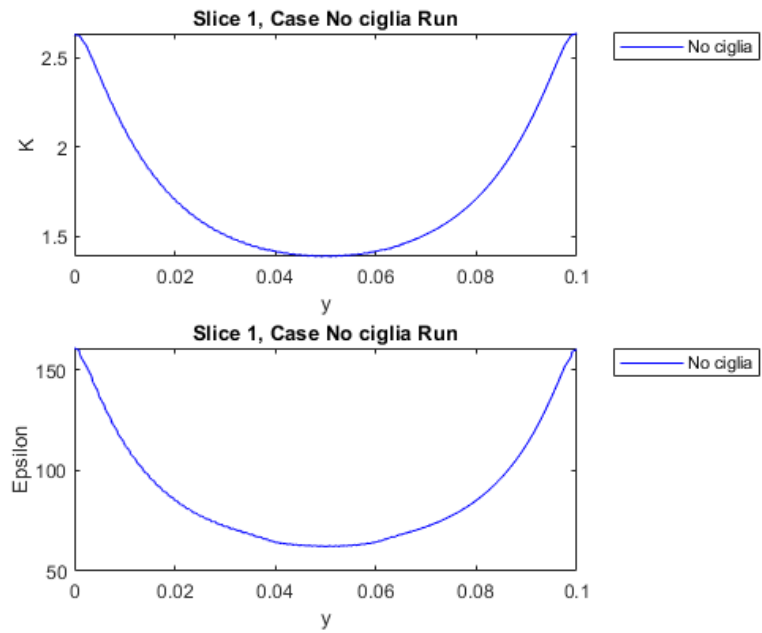


(b) $k \in \text{plot Slice2 case Walk}$

Figure 5.11: *Slice 2 plots.*

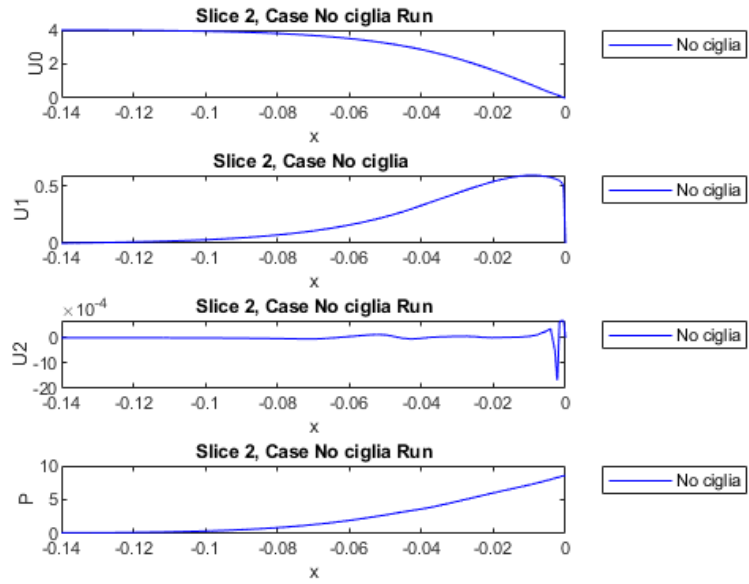


(a) $k \in \text{plotSlice1 case Run No Eyelashes}$

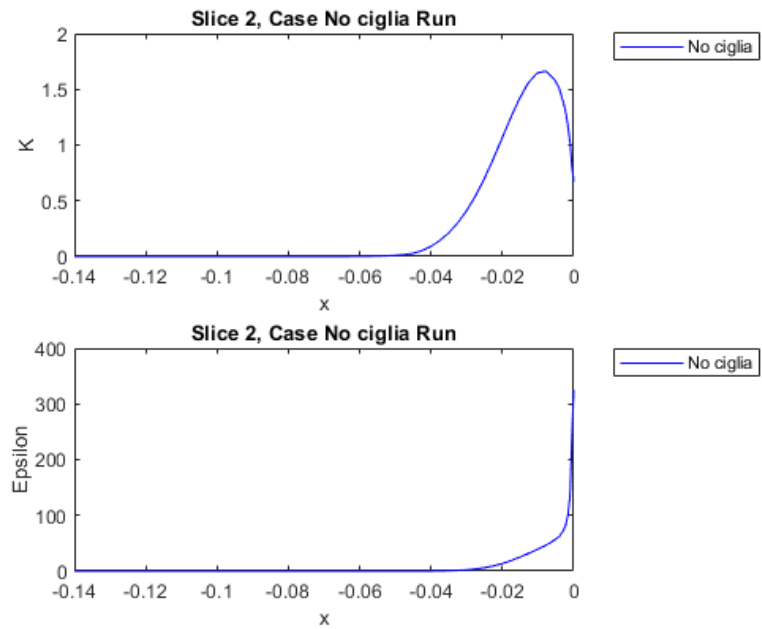


(b) $k \in \text{plot Slice1 case Run no Eyelashes}$

Figure 5.12: *Slice 1 plots.*

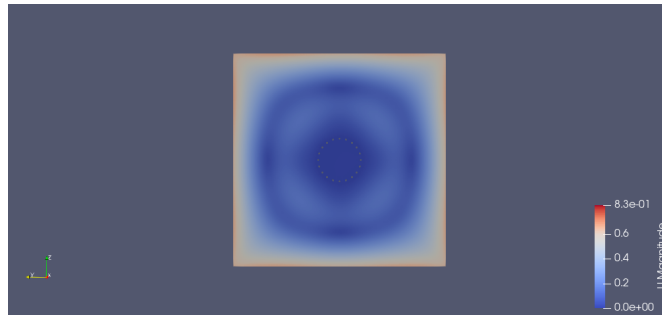


(a) $k \in \text{plotSlice2 case Run No Eyelashes}$

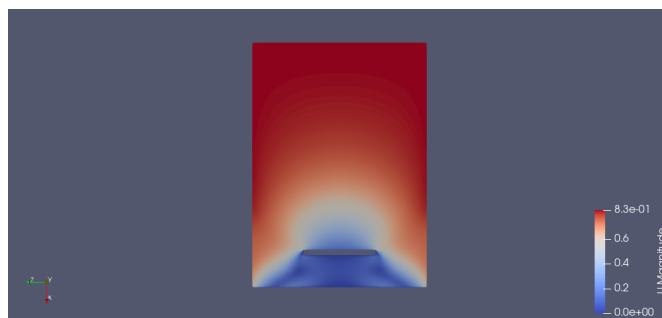


(b) $k \in \text{plot Slice2 case Run no Eyelashes}$

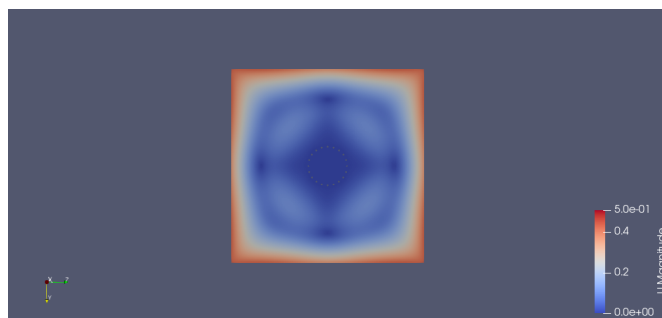
Figure 5.13: *Slice 2 plots.*



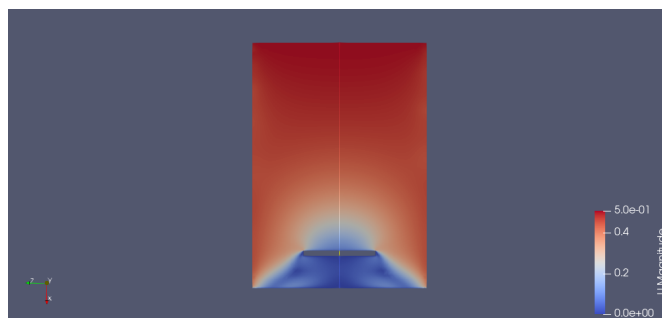
(a) *velocity Field SneezingSlice1*



(b) *velocity Field Sneezing Slice2*

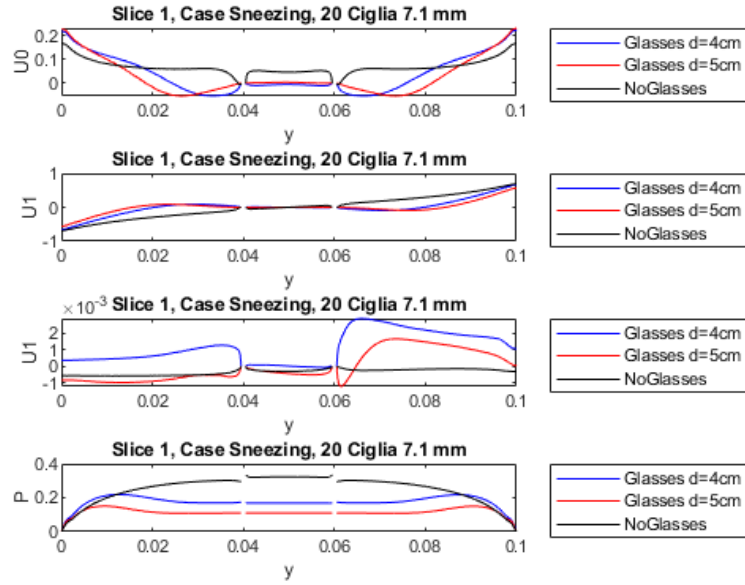


(c) *velocity Field Coughing Slice1*

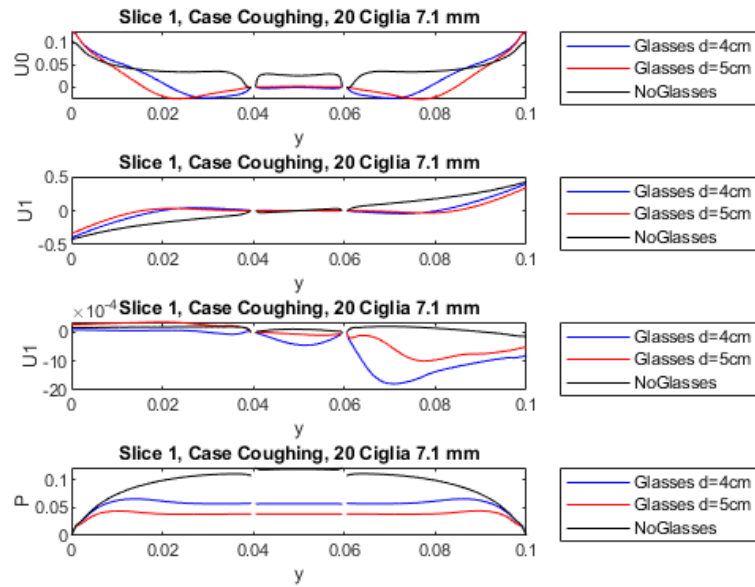


(d) *velocity Field Coughing Slice2*

Figure 5.14: *velocity field of the velocity magnitude on a horizontal (y-normal) and vertical (x-normal) section.*

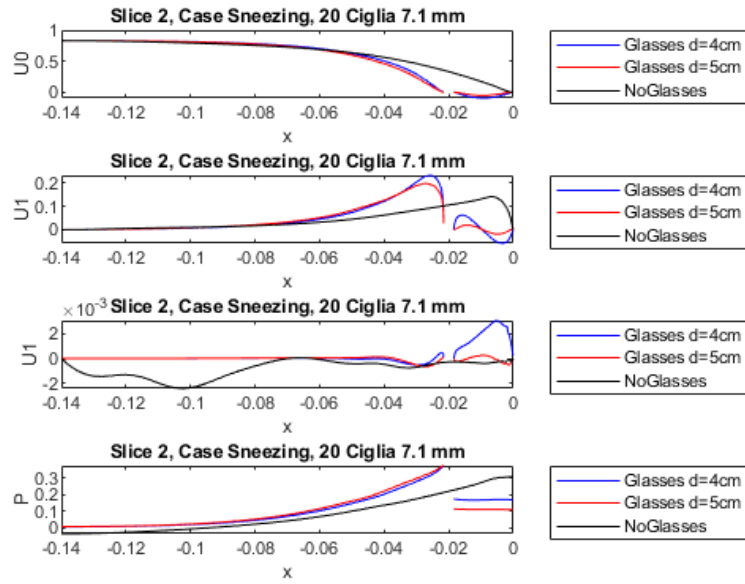


(a) U_0, U_1, U_2, P plot Slice1 case Sneezing

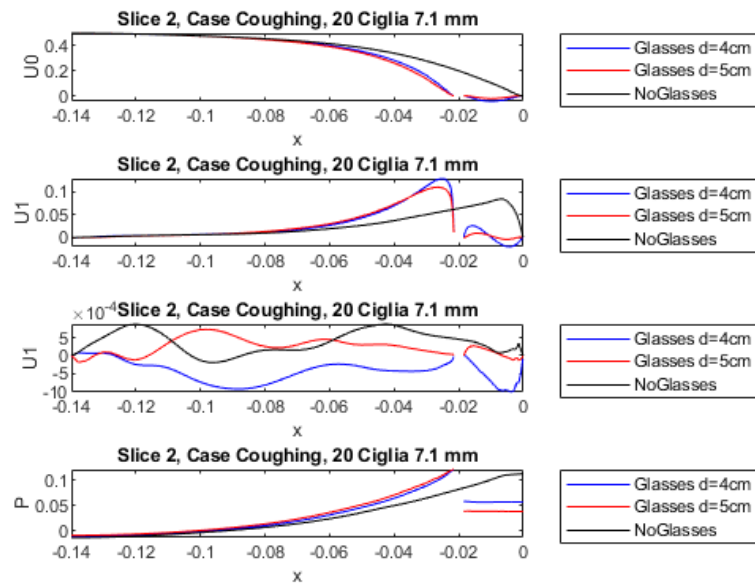


(b) U_0, U_1, U_2, P plot Slice1 case Coughing

Figure 5.15: *Slice 1 plots.*

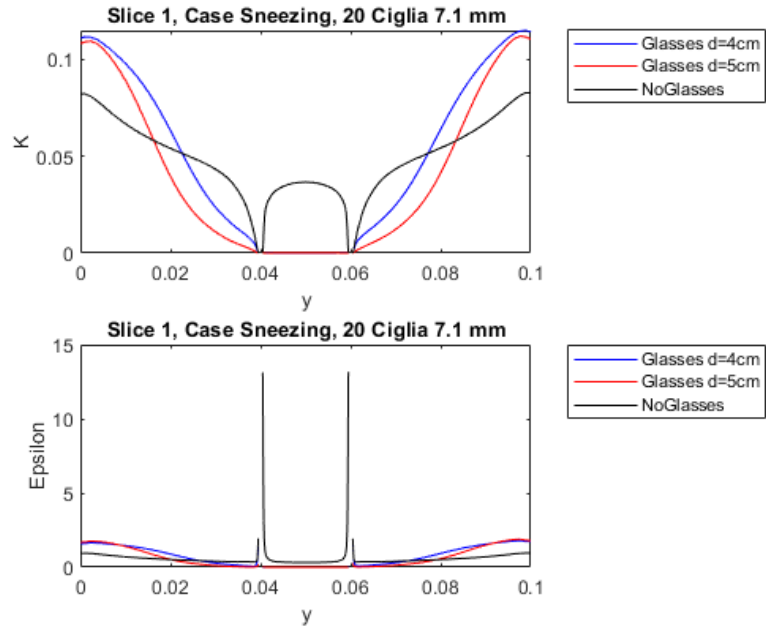


(a) U_0, U_1, U_2, P plot Slice2 case Sneezing

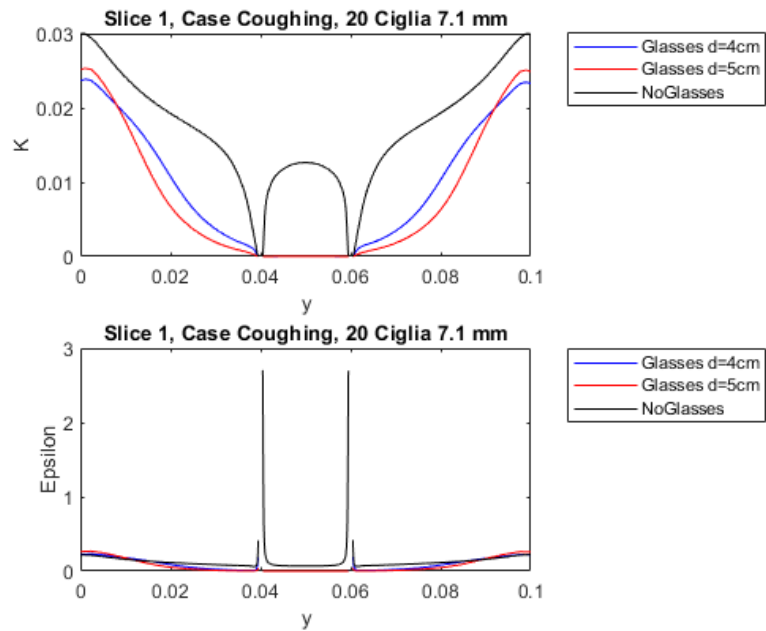


(b) U_0, U_1, U_2, P plot Slice2 case Coughing

Figure 5.16: *Slice 2 plots.*

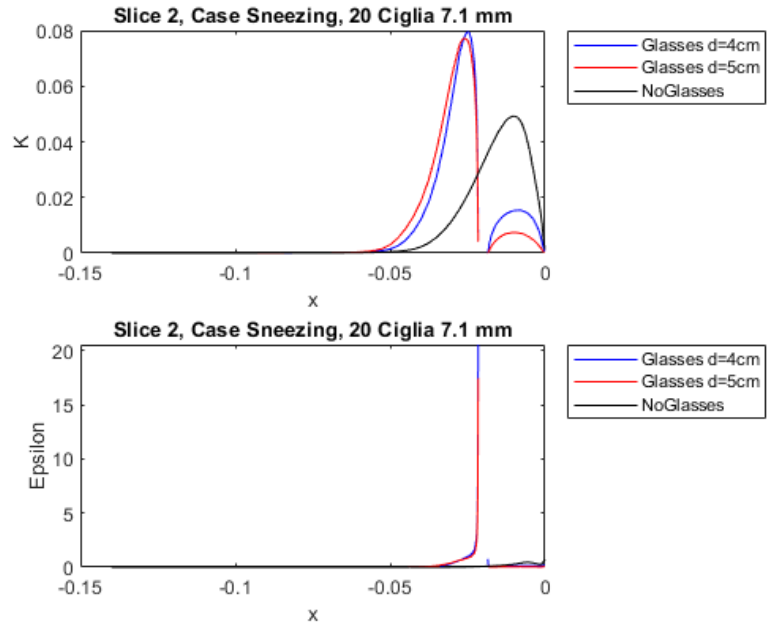


(a) $k \epsilon$ plotSlice1 case Sneezing

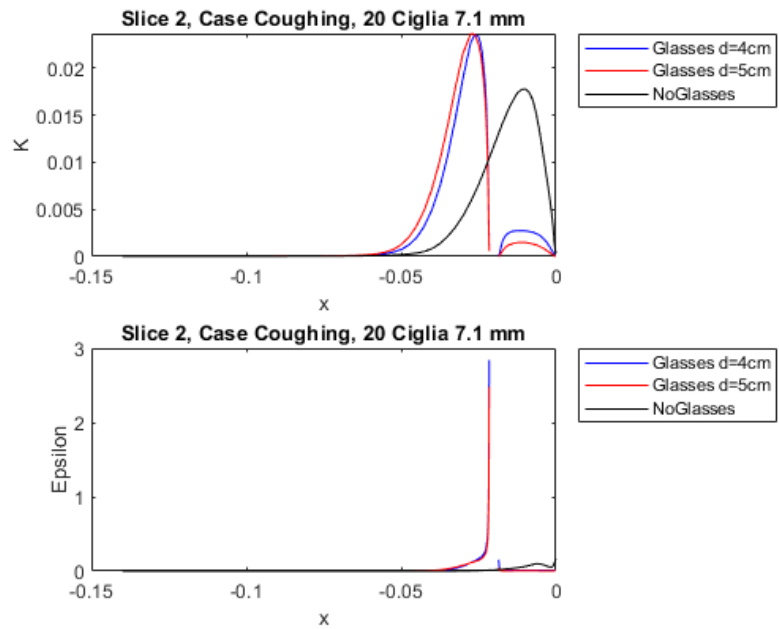


(b) $k \epsilon$ plot Slice1 case Coughing

Figure 5.17: *Slice 1* plots.



(a) $k \in \text{plotSlice2}$ case Sneezing



(b) $k \in \text{plot Slice2}$ case Coughing

Figure 5.18: *Slice 2* plots.

Part III

Simulations with Particles

Chapter 6

Particle Implementation

6.1 Governing Equations

To numerically model a multiphase flow, it is often important to use separate formulations for the different phases. The *particle phase* consists of bubble, particle, or drops and the *continuous phase* is the fluid in which these particles are generally immersed. The particle can be composed of solid, liquid, or gas, and the continuous fluid can be a liquid or a gas. The coupling between the particle motion and its surroundings can be used to classify the character of the multiphase flow, and thus help determine appropriate numerical techniques. The broadest division is between dispersed and dense flows, and refers to which coupling mechanism primarily determines the particle motion. A multiphase flow can be considered dispersed if the effect of particle-fluid interactions dominates the overall transport of the particles, while it is said to be dense if particle-particle interaction dominates particles motion. Dispersed flows includes one-way coupling (where the dispersed-phase motion is affected by the continuous phase, but not vice versa) and two-way coupling (where the dispersed phase also affects the continuous phase through the interphase coupling). Dense flows usually have four-way coupling where mutual interactions between particles become significant and the effects of the particles on the continuous fluid are weak and often neglected. As well described in [39], volume fraction of particles is the main parameter to make the division between one, two or four way coupling and therefore between dispersed and dense. The volume fraction is defined as $\phi_p = \frac{MV_p}{V}$ where M is the number of particles, V_p is the volume of a single particle and V is the volume occupied by particles and fluid:

- for $\phi_p < 10^{-6}$ there will be one-way coupling;
- for $10^{-6} < \phi_p < 10^{-3}$ there will be two-way coupling and the particles can also increase or dump turbulence;
- for $\phi_p > 10^{-3}$ there will be four-coupling and the flow will be considered as dense.

Another important parameter that may contribute to the selection of the appropriate model is the particle momentum *Stokes number* defined as the ratio between the particle response time τ_p and that of the system τ_s

$$S_t = \frac{\tau_p}{\tau_s} \quad (6.1)$$

$$\tau_p = \frac{\rho_p d^2}{18\rho_f \nu} \quad (6.2)$$

$$\tau_s = \frac{L_s}{v_s} \quad (6.3)$$

The equation 6.2 is valid only for *Stokes flow*.

If $S_t \rightarrow 0$, the particle behaves as a fluid tracer (momentum one-way coupling) and if $S_t \rightarrow \infty$ is unresponsive to the ow variations. One would define a Stokes number not only for momentum but also for mass and temperature in order to evaluate with more precision the mass coupling and energy coupling of particles with the continuous phase. If two-way coupling is considered, it simply involves some source terms in the continuous phase equations (momentum, energy, turbulence models...) that are generally described in an Eulerian reference frame. For the sake of simplicity, we have limited our interest to the one-way coupling.

6.1.1 Particle equations

Various treatments of the particle field can be employed. Particles could be described in an Eulerian or Lagrangian reference frame and, as suggested by *E. Loth* in his paper [40], distinctions could be done about the treatment of particle surface forces. In this work only the Lagrangian approach will be discussed. With this reference frame the particles are treated as individual and properties are updated along the path of each particle. For the treatment of the surface forces, the point- force treatment represents the ow over the particle with empirical and theoretical treatments (specifying a drag or lift coefficient) to obtain the force

on the particle. For the resolved surface treatment, the fluid dynamics (e.g., pressure and shear stress distributions) are fully resolved over the entire particle surface and then integrated to obtain the overall hydrodynamic forces. Following the point-surface approach and defining \mathbf{x}_p as the particle centroid and m_p the particle mass, Lagrangian particle equation of motion is:

$$m_p \frac{\partial \mathbf{v}}{\partial t} = \mathbf{F}_{body} + \mathbf{F}_{surf} \quad (6.4)$$

The left hand side represents the particle mass inertia and the right hand side represents the sum of body forces and surface forces on the particle. Body forces are those related to gravitational effects:

$$\mathbf{F}_{body} = \frac{(\rho_p - \rho)\pi d_p^3}{6} \mathbf{g} \quad (6.5)$$

where d_p and ρ_p are respectively the droplet diameter and droplet density. Surface forces can be seen as the sum of different terms: drag, virtual mass, a term related to pressure gradient and one to the ‘‘history’’ of particle (Basset term). The expressions for all these terms are listed below without a rigorous derivation:

The drag force is:

$$F_{d,i} = \frac{1}{2} \frac{\pi d_p^2}{4} \rho_f C_d |\mathbf{u} - \mathbf{u}_p| (u - u_{p,i}) \quad (6.6)$$

with

$$C_d = \frac{24}{Re_p} \left(1 + \frac{3}{16} Re_p\right)$$

The pressure gradient force is:

$$F_{p,i} = \frac{1}{6} \pi d_p^3 \rho_f \frac{Du_i}{Dt} \quad (6.7)$$

The added mass force (virtual force) is:

$$F_{A,i} = \frac{\pi d_p^3}{12} \rho_f \left(\frac{Du_i}{Dt} - \frac{\partial u_{p,i}}{\partial t} \right) \quad (6.8)$$

The Basset force is:

$$F_{B,i} = \frac{3}{2} d_p^2 \rho_f \sqrt{\pi \nu} \int_{-\infty}^t \frac{\partial}{\partial \tau} (u_i - u_{i,p}) \frac{\partial \tau}{\sqrt{t - \tau}} \quad (6.9)$$

where Re_p is the particle Reynolds number based on relative velocity:

$$Re_p = \frac{\rho d_p (\mathbf{u} - \mathbf{u}_p)}{\mu} \quad (6.10)$$

where ρ is the density of the continuous phase. A better description of all these terms can be found in [40] and [41].

6.2 Dispersion Models

Dispersion models are methods that seek to predict how turbulence affects the particles motion. They are employed for RANS (*Reynolds Averaged Navier Stokes equations*) simulations with particles in order to account the effect of unresolved turbulent structures. For this reason it is clear that these models will not be used on LES (*Large Eddy Simulation*) or DNS (*Direct Numerical Simulation*) simulations because the turbulent structures will be filtered and solved or completely solved. The idea behind those methods is to allow particle simulations without the need of a LES or DNS solutions which are extremely time consuming. On the other side these models will have less accuracy and an extremely complex mathematics involving stochastic variables in partial differential equations. In OPENFOAM[®] two dispersion models are implemented: *Stochastic Dispersion Model* and *Gradient Dispersion Model*. The *Stochastic Dispersion Model* adds a stochastic component \mathbf{u}_{turb} at the fluid velocity \mathbf{u} that is seen by each particle. The velocity associated with particles \mathbf{u}_p that determines the forces previously described is computed as it follows:

$$\mathbf{u}_p = \mathbf{u} + \mathbf{u}_{turb} \quad (6.11)$$

The magnitude of \mathbf{u}_{turb} is chosen for each parcel from a Gaussian random number distribution with standard deviation related with the turbulent kinetic energy k .

Chapter 7

Particle Simulations and Results

7.1 Case study

After the description of the employed models, the dissertations, moves on the study case. In OPENFOAM[®] all the entries defining the particles are contained in the dictionary *kineamticCloudProperties*. Two types of particles are widely studied: particles of PM (Particulate Matter) that indicates the set of solid or liquid substances suspended in air (with which they form a mixture called "atmospheric aerosol") which have dimensions ranging from a few nanometers to 100 micrometers and particles which represents the droplets of saliva potentially carrying viruses such as Sars-Cov2. The aim of the work is to show how these particles are deposited on the ocular surface and how they can be deflected by the fluxes of the motion field in different situations. It is important to underline that these two types of particles are not completely unrelated to each other; in fact, it has been demonstrated that areas in which there is a high level of environmental pollution; several studies have found that air pollution is a risk factor for respiratory infection by carrying microorganisms and affecting body's immunity [42].

It is known that the computational effort in particles simulations is strickly related with the total number of particles. In order to choose the number of particles for each simulation, several tests were carried out with 100, 200, 500 and 5000 particles per second; the results showed that in each case the behavior was the same, that is, most of them escaped from the computational volume with respect to the number of particles that remained suspended in it or deposited in

the various surfaces at the last moment of simulation. However, the cases with 100, 200 and 500 particles per second did not allow for an exhaustive statistical analysis due to the low total number of particles in the domain.

For this reason the choice moved on the case with the higher number of particles; the total number of particles per second that was chosen is $n_{particles/second} = 5000$. Nevertheless, for both case study there are some limitations: the most relevant is certainly the geometry with which the model was built, as said previously in the section about the generation of the motion fields. Another limitation concerns the gravity factor and the turbulence model chosen; in fact, in the absence of gravity, in all cases it leads to a more uniform distribution of particles on all surfaces and, especially in case study B, it leads to a decrease in the number of particles deposited on the cilia as the particles followed exclusively the flow which it was directed towards the lens. It is clear how these two assumptions made lead to limitations to work; in fact, it is not true that gravity acts on particles exclusively in the domain of interest, but particles undergo this effect even before entering the domain. Furthermore, the turbulence model chosen is a standard model that is certainly different from a real turbulence case, in which, presumably, vorticity effects are formed. By combining these two aspects, the flow and consequently the path of the particles could lead to a different deposition of the particles on the various surfaces. To simplify the discussion, the eyelashes and the lens have been trivially modeled as cylinders and the eye as a circumference. This model, excellent for carrying out a preliminary study, needs to be improved and brought closer to reality through the modeling of a three-dimensional spherical eye (consequently with a concavity that allows the particles to wedge into the eye socket in the case not were caught by the eyelashes), of eyelashes with a curvature, and in general, of a *stl* pattern representing a human face. A further aspect to be explored concerns the choice of boundary conditions and the setup of the selected cases; in fact, the hypothesis that particles are captured by some surfaces and not deflected or rebounded is for simplified purposes. At the same time, the distribution, number and density of the particles was generated by an extrapolation of the literature values found in the different scientific articles. Future applications could be interesting if the mean airborne density of PM10 particles in case study A and a law describing the motion of saliva droplets from a certain distance were evaluated for case study B.

Two other aspects to consider when evaluating the simulations are the absence

of interactions between particles and the absence of accumulation; the set up of the cases in fact, provides that when two particles collide they do not have any type of interaction and continue their undisturbed path and at the same time, they do not accumulate which means that on a surface in which a particle is attached, not if it will attack another one.

7.1.1 Choice and setup of atmospheric particulate deposition

For the Case study A, 20 simulations, each of which lasting 60 seconds starting from the last instant in which it reaches the motion field converges, were carried out in order to evaluate a potential situation in which a person is running and walking; in the first case, as explained in the previous chapters, the flow velocity is 4 m/s , in the second case 1.1 m/s . The assumption has been made that the particles are carried by the air flow and consequently they have been assigned the same flow velocity in the two cases; this aspect appears to be in agreement with a potential real case as small particles have a small inertia with respect to the flow.

All simulations were performed with the *icoUncoupledKinematicParcelFoam* solver, which is an unsteady solver for Lagrangian particle clouds.

Furthermore, for the two situations, the cases with 20, 30, 40 lashes and lengths of 5.8, 7.1, and 9.0 mm were evaluated as well as the cases in the absence of lashes in order to evaluate the central point of the work: how much and how the eyelashes protect the ocular surface.

The set up and choice of atmospheric particulate particles, whose values have been entered in the directory *kinematicCloudProperties*, has been chosen as follows for each particle:

- Diameter: 10 μm
- Density ρ : 1600 Kg/m^3
- Poisson Ratio : 0.187

The distribution of the particles was assigned as *fixedValue*, and in this way it was assumed that the particles had all the same diameter; although in the real case the distribution is approximately Gaussian.

During the motion, the particles are subjected to the effect of the velocity field and can interact with the surfaces of the control volume in a different way: get stuck (*type* stick), rebound on them (*type* rebound) or cross them (*type* escape).

The various surfaces have been set up as follows:

- Top: *type* rebound
- Eye: *type* stick
- Bottom: *type* stick
- North, South, East, West: *type* escape

A relevant aspect regarding simulations is certainly gravity; in the absence of gravity the particles tend to distribute more homogeneously than in the case in which gravity acts in the y direction.

7.1.2 Choice and Setup of Droplets deposition

For the Case study B, 6 simulations, each of which lasting 5 seconds were carried out ; in the first case, as explained in the previous chapters, the inlet velocity is 0.83 m/s , in the second case 0.5 m/s . The assumption has been made that the particles are carried by the air flow and consequently they have been assigned the same inlet velocity in the two cases; this aspect appears to be in agreement with a potential real case as the small particles have a small inertia with respect to the flow as shown in the previous case study.

Also in this case study, all simulations were performed with the *icoUncoupled-KinematicParcelFoam*.

Furthermore, for the two situations, the case with 20 eyelashes and lengths of 7.1 mm is evaluated with lens with diameter of 4 mm and 5 mm in order to evaluate the central point of the work: how much and how the lens protect the ocular surface.

The set up and choice of atmospheric particulate particles, whose values have been entered in the directory *kinematicCloudProperties*, has been chosen as follows for each particle:

- Diameter: variable with normal distribution μm
- Density ρ : 1000 Kg/m^3

- Poisson Ratio : 0.187

The distribution of the particles was assigned as *Normal*. The choice of this distribution, however, stems from the fact that the droplets that emerge from the mouth in the event of a sneeze or a cough are of different sizes; following the work of Xie *et al.* in which the size of the saliva droplets was evaluated between 60 and 100 μm , in this work we have set the following values:

- Mean: 75 μm
- Standard deviation : 25 μm
- Max Value: 100 μm
- Min Value : 60 μm

7.2 Results

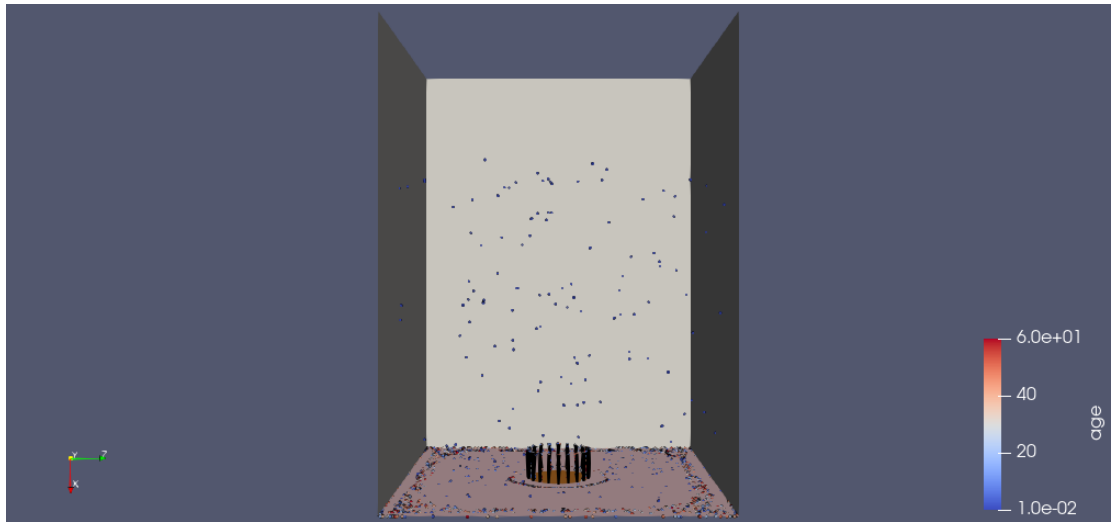
The results of the simulations of particle will be shown in the following section. Particular attention will be paid to the quantification of the particles deposited in the various patches of the computational volume and to how the different situations significantly affect the deposition of the particles on the surface of the eye. The data obtained by OPENFOAM[®] are post processed used Matlab and visualized using Paraview.

In case study A, particular attention will be paid to the quantity of PM particles captured by the eyelashes and how it can change with their geometry. At the same time, it will be evaluated how the absence of eyelashes leads to potentially dangerous situations for example how the particles, which are not captured by the eyelashes, are able to deposit on the inner part of the eyelid or on the surface of the eye. In case study B, particular attention will be paid to the quantity of droplets, captured by the eyelashes and by the lens placed at a fixed distance from the surface of the eye and the differences between a simulation with lens and without lens in the same conditions. Following the results obtained for Case Study A, eyelashes with a length of $9.0mm$ were chosen, chosen as the ideal length, and diameters of $5cm$ and $4cm$ of a hypothetical circular lens were evaluated. The main purpose of the work will be to evaluate a minimum degree of protection provided by the lenses in situations potentially harmful to human health; in fact, as shown in the introductory articles, the eye is a vehicle thanks to which a virus carried by a droplets can enter the human body and reproduce.

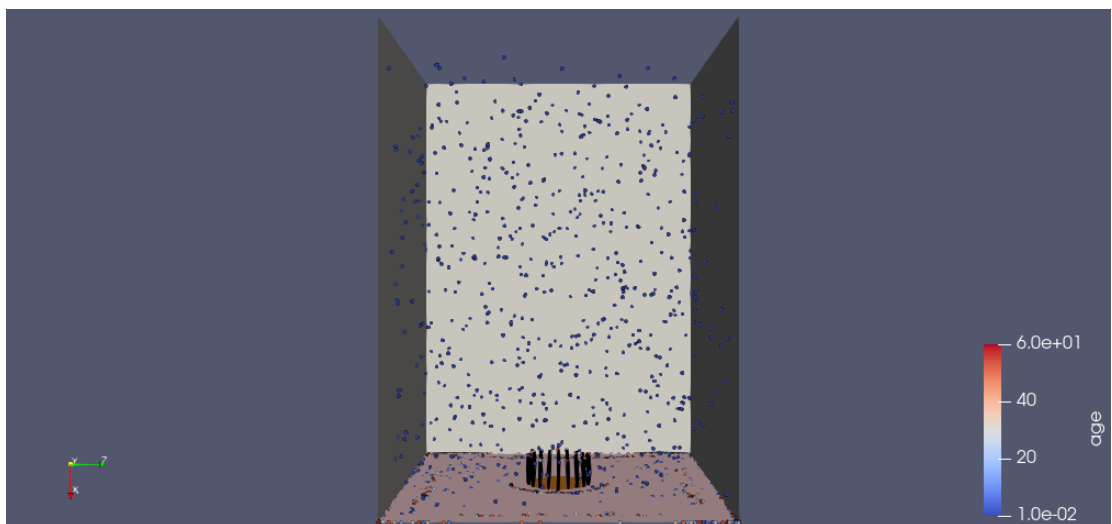
7.2.1 Atmospheric particulate deposition

The analysis of the results starts from the case with eyelashes. Our interest was focused on the particles fate: where they are going and what are the critical parameters. It is interesting to show the particle cloud at the last instant of the, that is $t = 60$ sec. In this first analysis the parameters concerning the length and the number of eyelashes are not taken into consideration as we show only which of the two situations is more dangerous with the same geometric parameters. In *Figure 7.1* the PM cloud is shown in the entire domain in the case Run and in the case Walk. In the first case there are fewer particles suspended in the domain as most of them are deposited on the bottom, eye and cilia surfaces and it will be shown that most of them escape from the domain. In the second case,

the considerations on the number of particles that escape from the domain are about the same but there are more particles suspended in the domain; this is due to the lower flow rate. In Figure 7.2 the difference between the Run case and the Walk case is shown; it is easy to understand how the deposition is quite similar in the two cases, with an important difference in the amount of particles deposited on the surface bottom and ciglia. This leads to the conclusion that in the run case, because of a higher flow velocity, there is a greater probability that the PM particles are deposited on the eye and on the eyelashes. In Figure 7.3 two special cases are shown: an important assessment to make concerns the role of gravity; in the cases shown in the two previous figures, gravity determines an accumulation of particles in the area of the domain towards which gravity acts (y direction) and consequently, assuming that the person is standing, the particles are deposited in the upper part of the eyelashes ; this could represent an interesting reasoning about the fact that the upper lashes are longer than the lower lashes to protect the surface of the eye. In the absence of gravity, as shown in Figure 7.3(a), the deposition of particles is more homogenous. However, there are some considerations to be made: gravity is evaluated exclusively in the longitudinal length of the computational domain and we assume that the velocity of the particle at the inlet has a certain direction and the direction depends on what happens upstream of the computational domain In Figure 7.3 (b) the case Run without eyelashes is shown: particle deposition effects are similar to the case with eyelashes as a first consideration; however due to the simplified geometry of the model, particles tend to settle in the bottom patch.

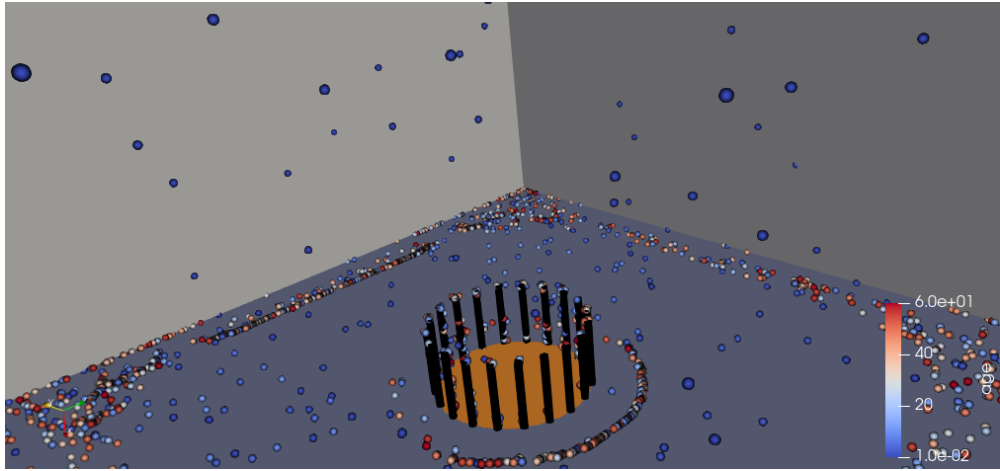


(a) *Case Run Eyelashes 9mm*

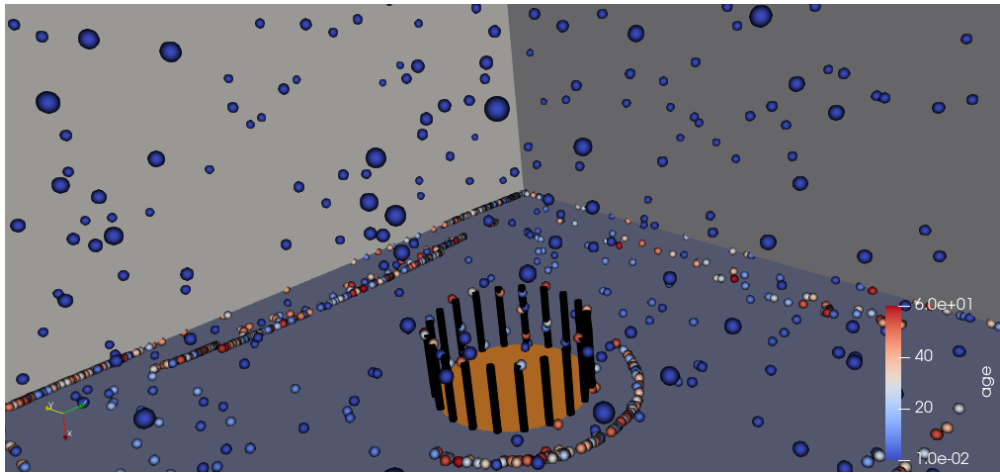


(b) *Case Walk Eyelashes 9 mm*

Figure 7.1: *PM cloud visualized at time $t=60$ sec entire computational volume*

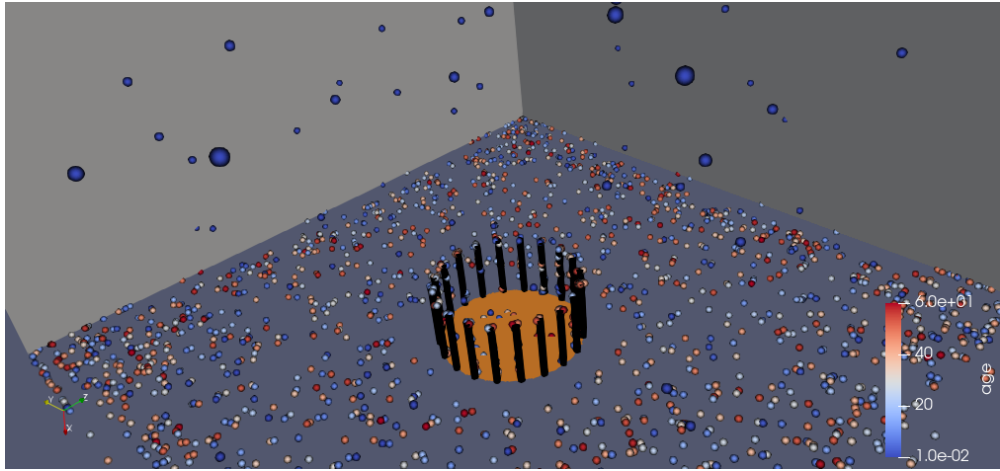


(a) *Case Run Eyelashes 9 mm*

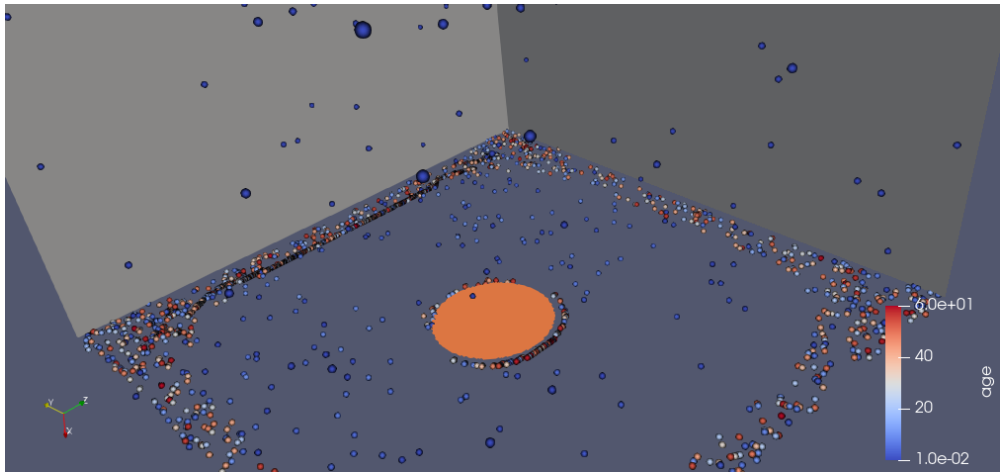


(b) *Case Walk Eyelashes 9 mm*

Figure 7.2: *PM cloud visualized at time $t=60$ sec bottom, eye and eyelashes.*



(a) *Case Run Eyelashes 9 mm no gravity*



(b) *Case Run No Eyelashes*

Figure 7.3: *PM cloud visualized at time $t=60$ sec bottom, eye and eyelashes without gravity (a) and without eyelashes (b).*

The most relevant aspect for the purpose of the work is to quantify the number of particles deposited in each surface in order to evaluate and establish an experimental protocol that allows to assign an ideal number and length of eyelashes. This purpose can be reached by comparing the various cases that have been simulated, and then drawing conclusions relating to them. Assuming the adhesion conditions as type stick of the most important surfaces and as type escape for the side walls of the computational domain, Tables 7.1 and 7.2 show the total number of particles and their final destination after 60 seconds of simulation. The first column shows the name of the case with the length (L) in mm of the eyelashes and the amount (N), the column *Current* shows the number of particles that are suspended in the computational domain, *Added* the number of particles injected into the domain in 60 seconds, *Escaped* the number of particles escaped from the computational domain while the Patches names concern the number of attached particles to them. At the same time, Tables 7.3 and 7.4 show the same normalized values with respect to the number of particles per second introduced into the system (5000), so that the various cases can be evaluated in parallel.

The quantification of the results can also be explained thanks to the introduction of a parameter:

- β : number of particles deposited on the eyelashes / number of particles introduced into the calculation volume

The β parameter suggests, as shown in *Figure 7.4* and *Figure 7.4*, the larger β , the greater the number of particles deposited on the facial surface or eyelashes compared to the particles introduced into the system and it can be deduced that also in this case a greater number of eyelashes (40) the facial surface captures fewer particles with the length $L = 5.6mm$ while the eyelashes capture a greater number of particles with the length of $L = 7.1mm$ and $L = 9.0mm$. Furthermore, as the length of the eyelashes increases, there is an increase in the number of particles captured regardless of the number of eyelashes of the model; with a number of lashes equal to 40, there is a more important slope of the curve at high values of lash length.

Following the values of the tables introduced previously, given the low number of particles deposited on the eye, these parameters will be evaluated exclusively for and eyelashes patch.

To evaluate how the parameters influence the number of particles captured by the lashes, a contour plot is shown in *Figure 7.5* showing the number of lashes on

the x axis and their length on the y axis for both the run case and the walk case. What emerges is how a small number of cilia between 20 and 30 captures too few particles, while a high number such as 40 captures a much greater number of particles. In the case of walking, as a first aspect the graph shows that the number of particles captured by the eyelashes is lower than in the case of running; in fact, the maximum number of particles captured turns out to be around 100 in the case with lashes of 9.0 mm length and number of lashes 40, a value which is more than doubled in the case of running. Another aspect to take into consideration is the fact that the contour plot in the case of walking presents curves with a very similar slope; consequently both the parameters regarding the length of the lashes and the parameters regarding their number are important. This does not happen for the run case, in which the curves have a similar slope up to 30 lashes, as this number increases they take an almost horizontal trend which represents the fact that increasing the number of eyelashes the only parameter that seems to be representative is the length.

Case Walk	Particles					
	<i>Current</i>	<i>Added</i>	<i>Eye</i>	<i>Eyelashes</i>	<i>Bottom</i>	<i>Escaped</i>
1. L 5.8 N 20	1690	$2.995 \cdot 10^5$	1	31	975	$2.9826 \cdot 10^5$
2.L 7.1 N 20	1793	$2.995 \cdot 10^5$	0	24	1067	$2.9816 \cdot 10^5$
3. L 9.0 N 20	1674	$2.995 \cdot 10^5$	0	32	936	$2.9828 \cdot 10^5$
4. L 5.8 N 30	1661	$2.995 \cdot 10^5$	1	33	942	$2.2829 \cdot 10^5$
5. L 7.1 N 30	1628	$2.995 \cdot 10^5$	0	42	920	$2.9832 \cdot 10^5$
6. L 9.0 N 30	1660	$2.995 \cdot 10^5$	0	52	925	$2.9829 \cdot 10^5$
7. L 5.8 N 40	1731	$2.995 \cdot 10^5$	0	72	969	$2.9822 \cdot 10^5$
8. L 7.1 N 40	1700	$2.995 \cdot 10^5$	0	88	926	$2.9825 \cdot 10^5$
9. L 9.0 N 40	1738	$2.995 \cdot 10^5$	0	110	941	$2.9821 \cdot 10^5$
10. No eyelashes	1341	$2.995 \cdot 10^5$	2	//	636	$2.861 \cdot 10^5$

Table 7.1: *Quantifies of particles case walk*

Case Run	Particles					
	<i>Current</i>	<i>Added</i>	<i>Eye</i>	<i>Eyelashes</i>	<i>Bottom</i>	<i>Escaped</i>
1. L 5.8 N 20	2074	$2.995 \cdot 10^5$	1	56	1765	$2.9788 \cdot 10^5$
2.L 7.1 N 20	2231	$2.995 \cdot 10^5$	0	80	1887	$2.9772 \cdot 10^5$
3. L 9.0 N 20	2090	$2.995 \cdot 10^5$	1	130	1694	$2.9786 \cdot 10^5$
4. L 5.8 N 30	2074	$2.995 \cdot 10^5$	0	90	1677	$2.9788 \cdot 10^5$
5. L 7.1 N 30	2055	$2.995 \cdot 10^5$	0	137	1658	$2.9790 \cdot 10^5$
6. L 9.0 N 30	2120	$2.995 \cdot 10^5$	1	195	1689	$2.9783 \cdot 10^5$
7. L 5.8 N 40	2026	$2.995 \cdot 10^5$	1	103	1660	$2.9792 \cdot 10^5$
8. L 7.1 N 40	2027	$2.995 \cdot 10^5$	0	118	1633	$2.9792 \cdot 10^5$
9. L 9.0 N 40	2234	$2.995 \cdot 10^5$	0	259	1720	$2.9772 \cdot 10^5$
10. No eyelashes	2243	$2.995 \cdot 10^5$	4	//	1957	$2.9771 \cdot 10^5$

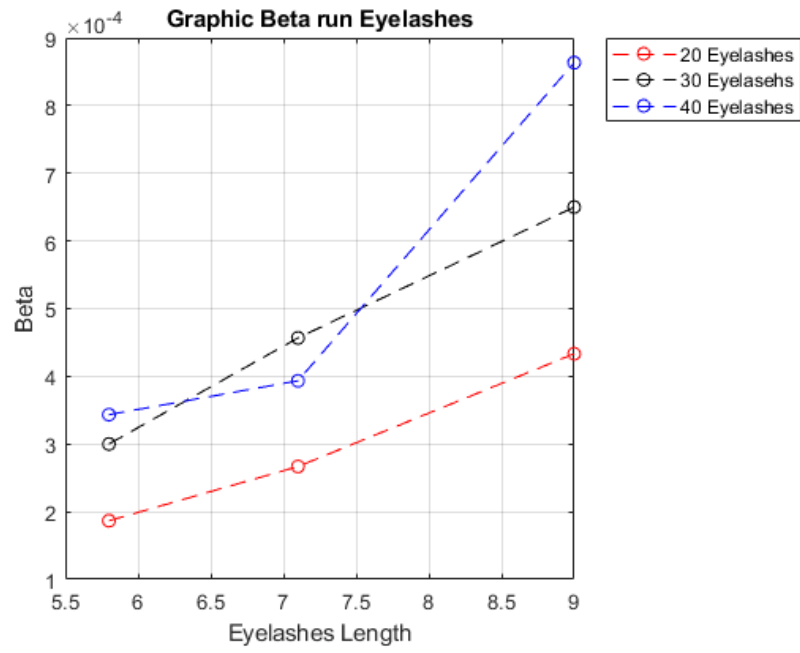
Table 7.2: *Quantifies of particles case run*

Case Walk	Particles					
	<i>Current</i>	<i>Added</i>	<i>Eye</i>	<i>Eyelashes</i>	<i>Bottom</i>	<i>Escaped</i>
1. L 5.8 N 20	0.388	59.99	0.0002	0.0062	0.195	59.652
2.L 7.1 N 20	0.3586	59.99	0	0.0048	0.2134	59.631
3. L 9.0 N 20	0.3348	59.99	0	0.0064	0.1872	59.655
4. L 5.8 N 30	0.3322	59.99	0.0002	0.0066	0.1884	59.658
5. L 7.1 N 30	0.3256	59.99	0	0.0084	0.184	59.664
6. L 9.0 N 30	0.332	59.99	0	0.0104	0.185	59.658
7. L 5.8 N 40	0.3462	59.99	0	0.0144	0.1938	59.644
8. L 7.1 N 40	0.340	59.99	0	0.0176	0.1852	59.644
9. L 9.0 N 40	0.3476	59.99	0	0.022	0.1882	59.65
10. No eyelashes	0.2682	59.99	0.0004	//	0.1272	59.772

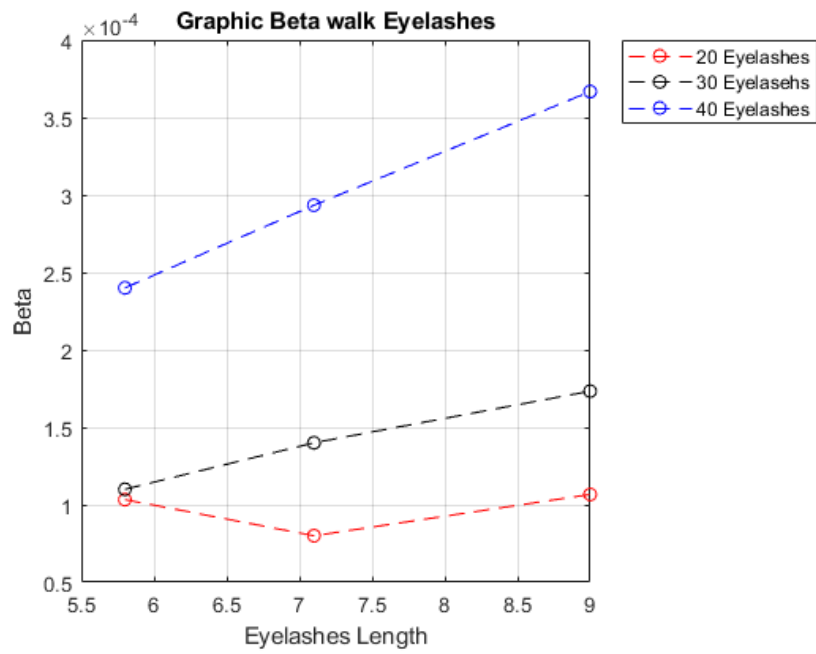
Table 7.3: *Quantifies of particles case walk normalized*

Case Run	Particles					
	<i>Current</i>	<i>Added</i>	<i>Eye</i>	<i>Eyelashes</i>	<i>Bottom</i>	<i>Escaped</i>
1. L 5.8 N 20	0.4148	59.99	0.0002	0.0112	0.353	59.574
2.L 7.1 N 20	0.4462	59.99	0	0.016	0.3774	59.544
3. L 9.0 N 20	0.418	59.99	0.0002	0.026	0.3388	59.572
4. L 5.8 N 30	0.4148	59.99	0	0.018	0.3354	59.575
5. L 7.1 N 30	0.411	59.99	0	0.0274	0.3316	59.579
6. L 9.0 N 30	0.424	59.99	0.0002	0.039	0.3378	59.566
7. L 5.8 N 40	0.4052	59.99	0.0002	0.0206	0.332	59.585
8. L 7.1 N 40	0.4054	59.99	0	0.0236	0.3266	59.585
9. L 9.0 N 40	0.4468	59.99	0	0.0518	0.344	59.54
10. No eyelashes	0.4486	59.99	0.0008	//	0.3914	59.541

Table 7.4: *Quantifies of particles case run normlized*

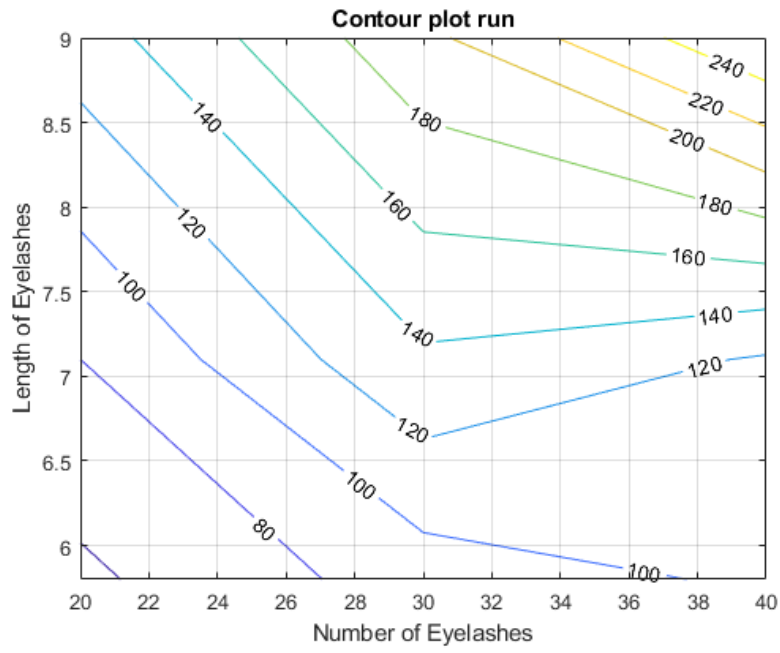


(a)

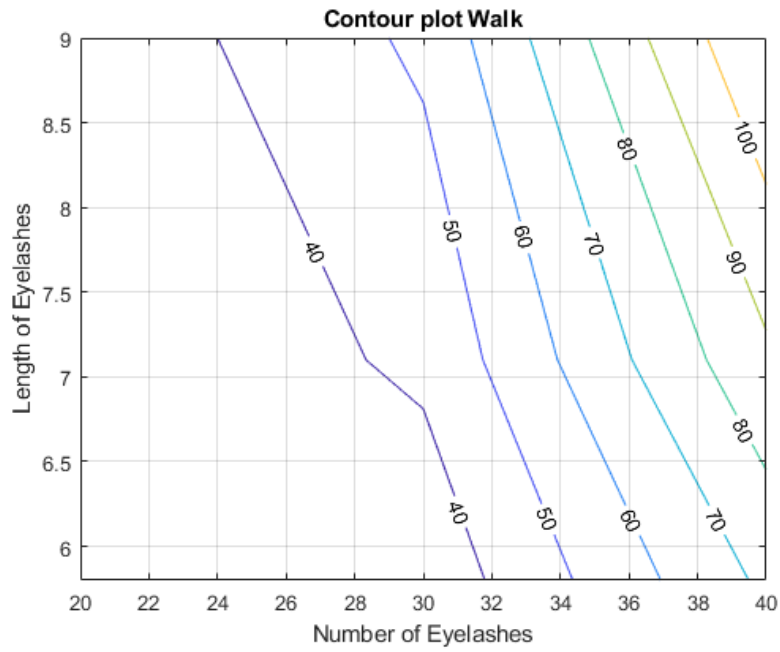


(b)

Figure 7.4: β on eyelashes patch case run (a) and case walk (b)



(a)



(b)

Figure 7.5: Contour plot with the number of particles captured by eyelashes, case run (a) and case walk (b)

Cylindrical volume in front of the ocular surface evaluation

Here we show the number of particles passing through a cylindrical volume positioned within the volume between the surface of the eye and the eyelashes; the evaluation was made both in the case with 40 lashes of $9mm$ length, and in the case without lashes. Both case were evaluated during a running. This cylinder, as shown in the *Figure 7.6*, is centered in the center of the eye and has a radius $R = 0.01m$ and a height $h = 0.01m$; this represents a volume with a base similar to the size of the circumference of the eye and a height slightly higher than that of the eyelashes and permit to have an idea of how many particles pass through that volume and it was done because the simplifications of the model and the mesh that has been created, do not allow to have certainties regarding the deposition. On the other hand, the number of particles that pass in front of the eye, which could potentially deposit themselves on the ocular surface, is more truthful.

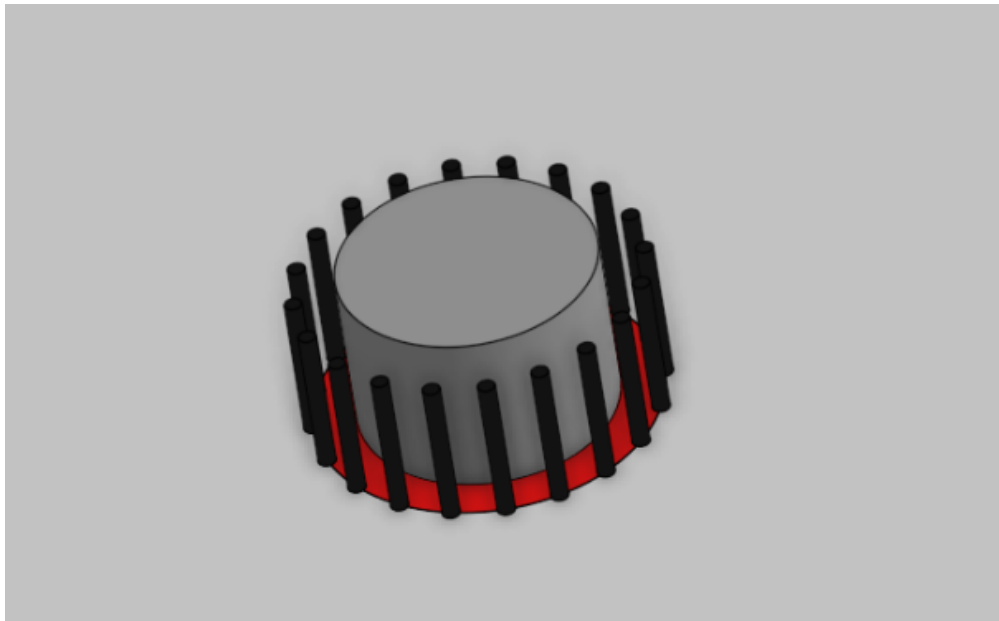


Figure 7.6: *Cylindrical volume in front of the ocular surface*

The purpose of this type of analysis is to understand how the presence of eyelashes can affect the number of particles within the chosen volume. To do this, the 60 seconds of simulation already presented previously were evaluated and the results were the following:

Case with eyelashes:

- Total particles entered into the volume: 44
- Particles captured by the eyelashes after 60 seconds: 259
- Average Particles entered per second: 3.3846

Case without eyelashes:

- Total particles entered into the volume: 76
- Particles captured by the eyelashes after 60 seconds: //
- Average Particles entered per second: 5.8452

It is clear that, in the presence of eyelashes, a smaller number of particles cross the volume, suggesting that there is also a modification of the flow that carries them. In Figure 7.7 are schematically shown the results.

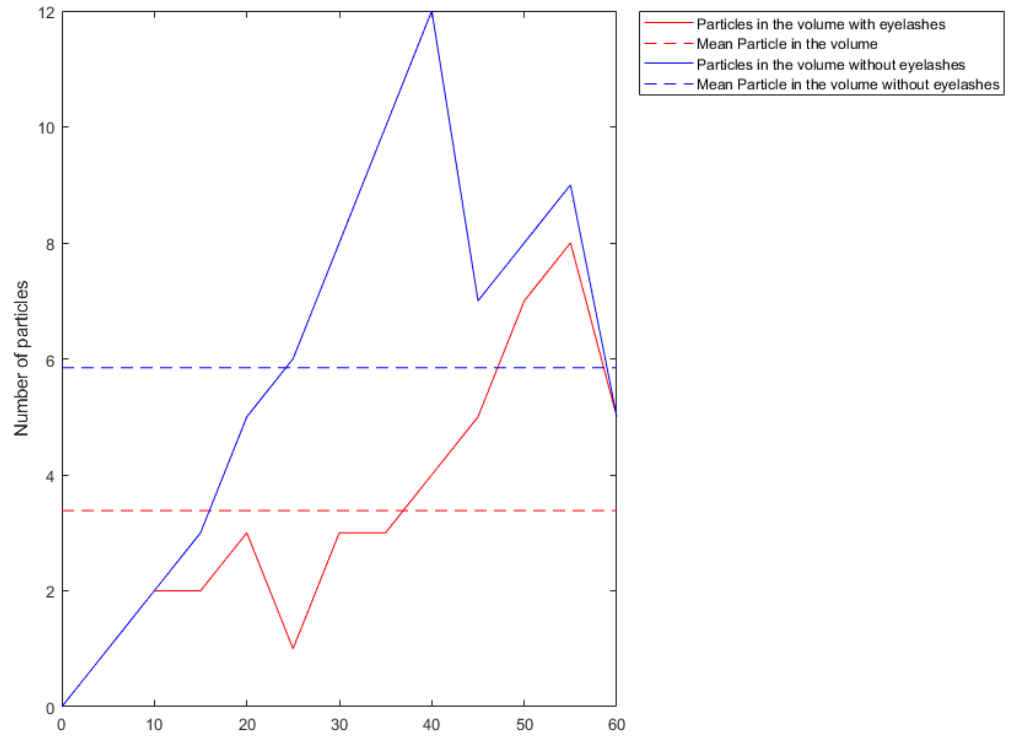


Figure 7.7: Plot of the particles passing through the cylindrical volume as a function of time

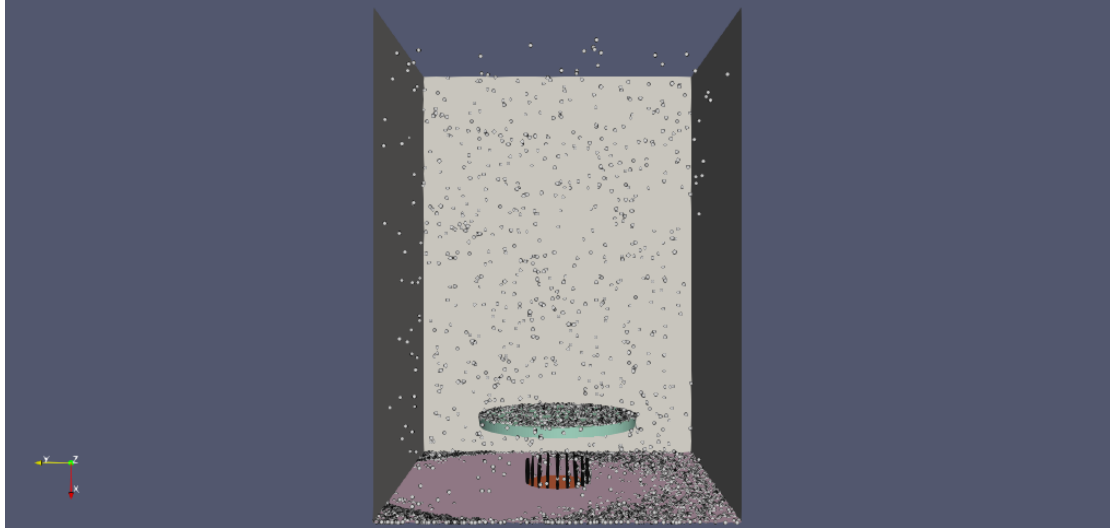
7.2.2 Droplets deposition

The analysis of the results, also in this case, starts with a 3D visualisation of the simulation with and without the lens. To synthesize the discussion, it appears reasonable to show the case with a lens of diameter $d = 5\text{cm}$; in fact, the results of the simulations with a smaller diameter are almost the same as demonstrated in the results of the velocity field.

Our interest was focused on the particles fate and it is interesting to show the particle cloud in the first moment of simulation, for example at $t = 5$ sec; this is done because it is assumed that the duration of an event such as cough or sneeze is temporally short.

In Figure 7.8 the clouds of droplets related to the case of sneezing (a) and to the case of coughing (b) are shown; in the first case it appears clear that the greater intensity of the event leads to the deposition of a greater number of particles than in the second case, due to a different inlet speed set in the flow field. In both cases, however, the lens captures a large number of particles preventing them from coming into contact with the ocular surface and confirming both the severity of the sneeze case compared to the cough, and the positive effect that the lens has. It should be noted that even the eyelashes capture more particles and consequently play their role in a more appropriate way in the case of sneezing. The same effects are shown in *Figure7.9* giving particular attention to the area of interest, ie the lens and the surface of the eye.

In Figure 7.10 two particular cases are shown. In the Figure (a) are shown the results without the lens and it appears clear that, without a protection, the surface of the eye is affected by a greater number of particles as well as the eyelashes. In Figure (b) is shown a simulation without the effect of the gravity in y direction and the arrangement of the particles in the bottom appears symmetrical, as well as the particles are positioned more homogeneously on the surface of the lens; however, this situation is far from a real case.

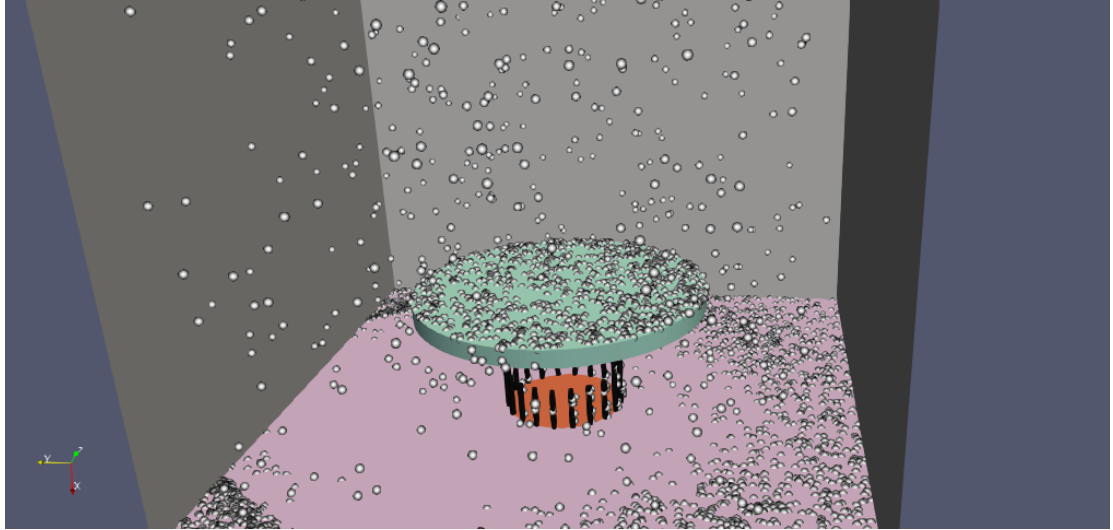


(a) Case sneezing Lens $d=5\text{cm}$, eyelashes $L=7.1\text{ mm}$

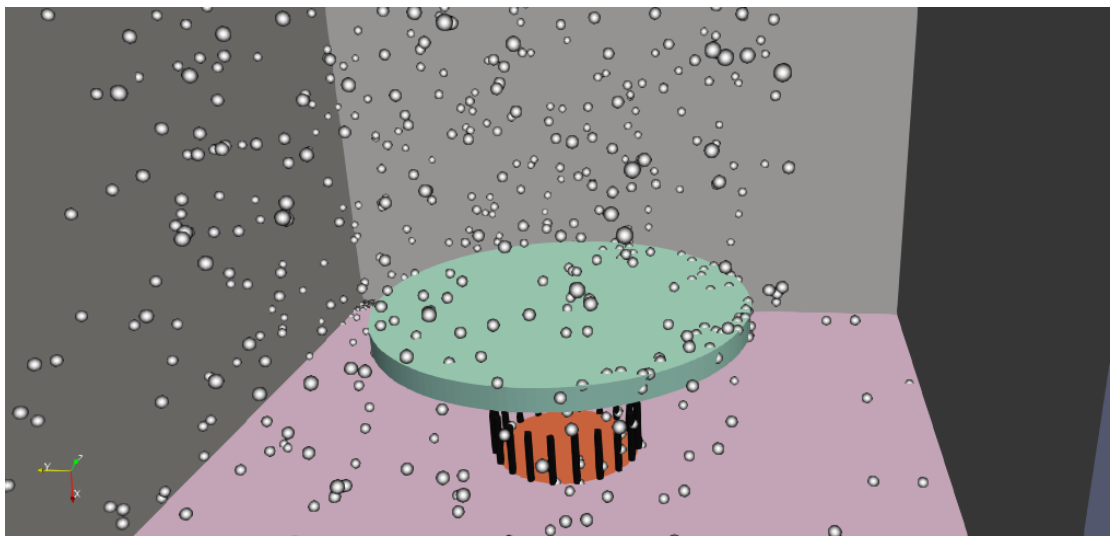


(b) Case coughing Lens $d=5\text{cm}$, eyelashes $L=7.1\text{ mm}$

Figure 7.8: Droplets Cloud at time $t=5\text{sec}$ entire computational volume

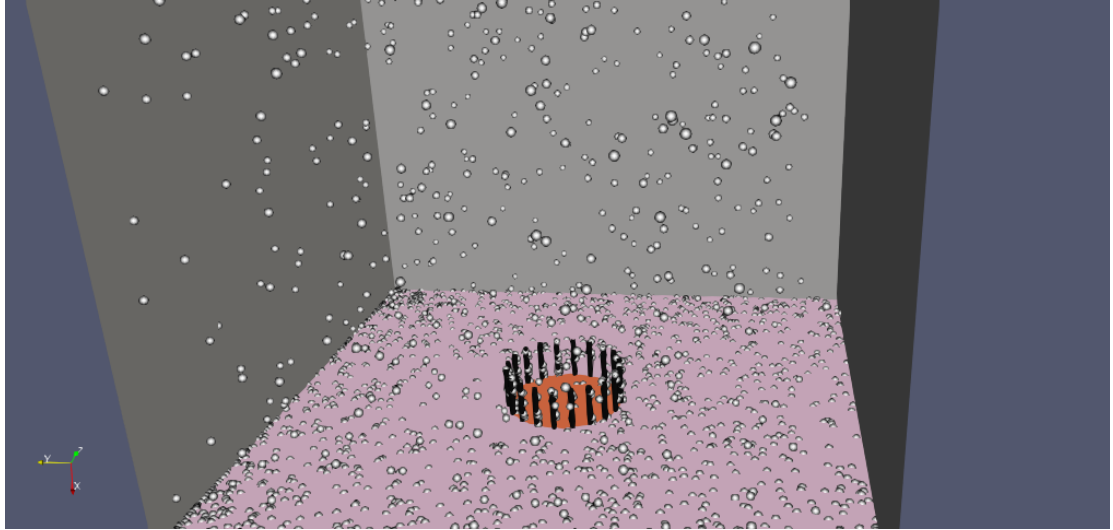


(a) Case sneezing Lens $d=5\text{cm}$, eyelashes $L=7.1\text{ mm}$

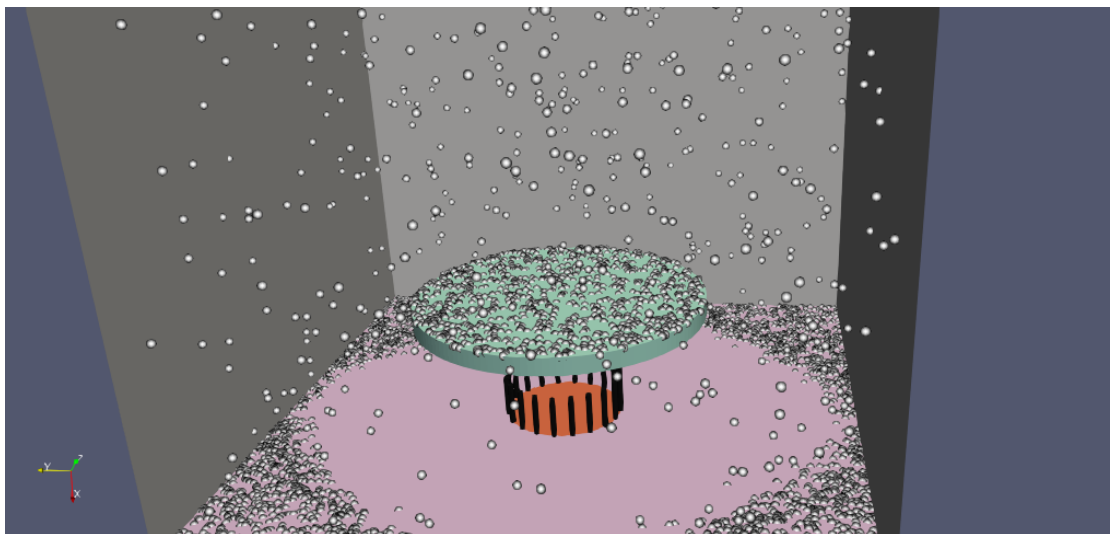


(b) Case coughin Lens $d=5\text{cm}$, eyelashes $L=7.1\text{ mm}$

Figure 7.9: Droplets Cloud at time $t=5\text{sec}$ bottom, lens, eye and eyelashes



(a) Case sneezing without Lens, eyelashes $L=7.1$ mm



(b) Case sneezing Lens $d=5$ cm, eyelashes $L=7.1$ mm, no gravity

Figure 7.10: Droplets Cloud at time $t=5$ sec bottom, lens, eye and eyelashes

Also in this case study, the quantification of the results is fundamental in order to understand which is the path of the particles and which surfaces are affected by them. As already mentioned, droplets are potentially carriers of viruses such as Sars-CoV-2 and, upon coming into contact with the eye, can penetrate the respiratory system and cause the onset of diseases and inflammation in the lungs . For this reason, the use of a lens could be useful at the same time as the respiratory protection mask. The aim of the project is to understand and quantify the importance of the lens in protecting the ocular surface so that it provides support for natural means of protection such as eyelashes. Assuming the adhesion conditions as type stick of the most important surfaces and as type escape for the side walls of the computational volume, Tables 7.5 shows the total number of particles and their final destination after 5 seconds of simulation. The first column shows the name of the case with the length (L) in mm of the eyelashes and the type of case (C=coughing, S=sneezing), the column *Current* shows the number of particles that are suspended in the computational volume, *lens* the number of particles on the lens, *Escaped* the number of particles escaping from the computational volume while the Patches names concern the number of attached particles to them. The fixed parameters are the number of particles introduced into the system after 5 seconds is, for all cases it is 24950 particles and the lash length equal to 7.1 mm. At the same time, Tables 7.6 shows the same normalized values with respect to the number of particles per second (5000) introduced into the system, so that the various cases can be evaluated in parallel. Also in this case we introduced a parameter which can explain the quantification of the results evaluated at time $t = 5s$ sec:

- β : number of particles deposited on the eyelashes or on the lens/ number of particles introduced in the calculation volume

Following the values of the tables introduced previously, given the low number of particles deposited on the eye, these parameters will be evaluated exclusively for lens and eyelashes patches.

The analysis of the parameter β led to conclusions similar to those reached in the previous case; to confirm the fact that a pair of glasses with a larger surface protects better, in *Figure 7.11* is shown that as the diameter of the lens increases, the number of particles deposited on the lens increases with a high slope in the case of sneezing, with a lower slope in the case of cough; at the same time the number of captured particles of the eyelashes decreases with a similar slope in

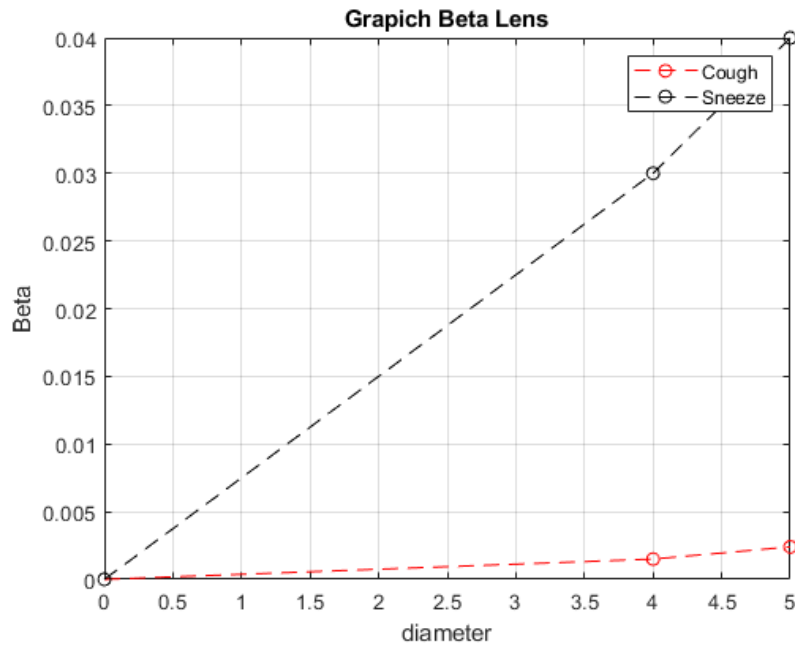
both cases showing that the eyelashes and the surface of the eye are protected by the lens.

Case	Particles					
	<i>Current</i>	<i>Lens</i>	<i>Eye</i>	<i>Eyelashes</i>	<i>Bottom</i>	<i>Escaped</i>
1. d=4 C	1270	38	0	26	38	23680
2. d=4 S	4640	781	0	83	3007	20310
3. d=5 C	1273	62	0	16	62	23677
4. d=5 S	4579	1010	0	65	2730	20371
5. d=// C	1202	//	0	65	40	23748
6. d=// S	2693	//	7	141	1724	22257
7. d=5 S NoGrav	5505	1079	0	0	3615	19445

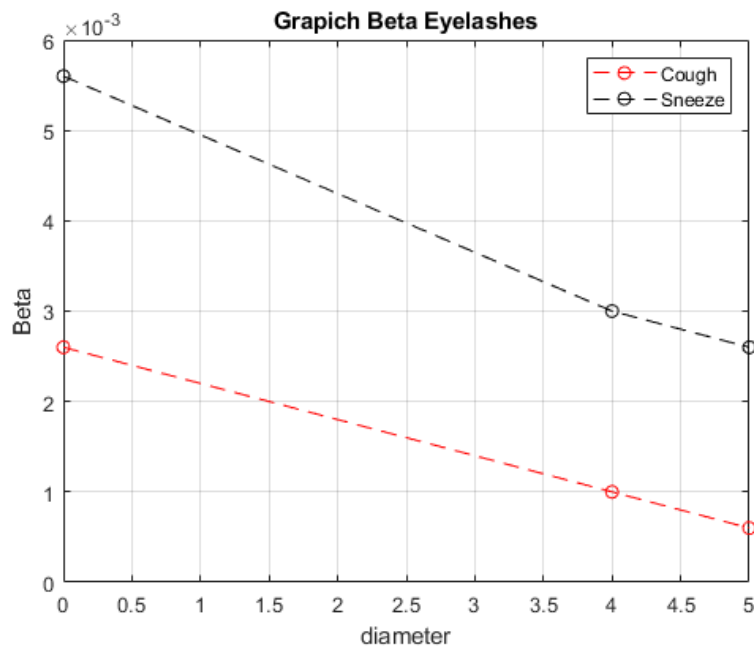
Table 7.5: *Quantification of particles of Droplets*

Case	Particles					
	<i>Current</i>	<i>Lens</i>	<i>Eye</i>	<i>Eyelashes</i>	<i>Bottom</i>	<i>Escaped</i>
1. d=4 C	0.254	0.076	0	0.0052	0.007	4.73
2. d=4 S	0.928	0.156	0	0.0166	0.6	4.06
3. d=5 C	0.2546	0.0124	0	0.0032	0.0124	4.73
4. d=5 S	0.91	0.202	0	0.013	0.546	4.07
5. d=// C	0.240	//	0	0.013	0.008	4.74
6. d=// S	0.5386	//	0.0014	0.028	1724	4.45
7. d=5 S NoGrav	1.10	0.21	0	0	0.72	3.889

Table 7.6: *Quantification of particles of Droplets Normalized*



(a) *Lens*



(b) *Eyelashes*

Figure 7.11: *Alpha* evaluated on lens (a) and eyelashes (b)

Cylindrical volume in front of the ocular surface evaluation

Using the same volume shown in *Figure 7.7*, here we show the number of particles that pass through the chosen cylinder in a case in which there is a lens with a diameter of $d = 5$ cm and in a case in which there is not this lens; both cases are evaluated during a sneezing, that is chosen as the case in which there are more particles deposited on the various surfaces. Following the work of Amador et al. we have chosen a length of eyelashes $L = 7.1mm$.

In this case the 5 seconds of simulation were evaluated and the results were the following:

Case with lens:

- Total particles entered into the volume: 44.
- Particles captured by the eyelashes after 5 seconds: 65.
- Average Particles entered per second: 2.95.

Case without lens:

- Total particles entered into the volume: 76.
- Particles captured by the eyelashes after 5 seconds: 141.
- Average Particles entered per second: 7.25.

The graph in *Figure 7.12* shows how in the absence of a lens, there is a greater number of particles that pass through the volume and consequently the danger of these falling on the surface of the eye increases.

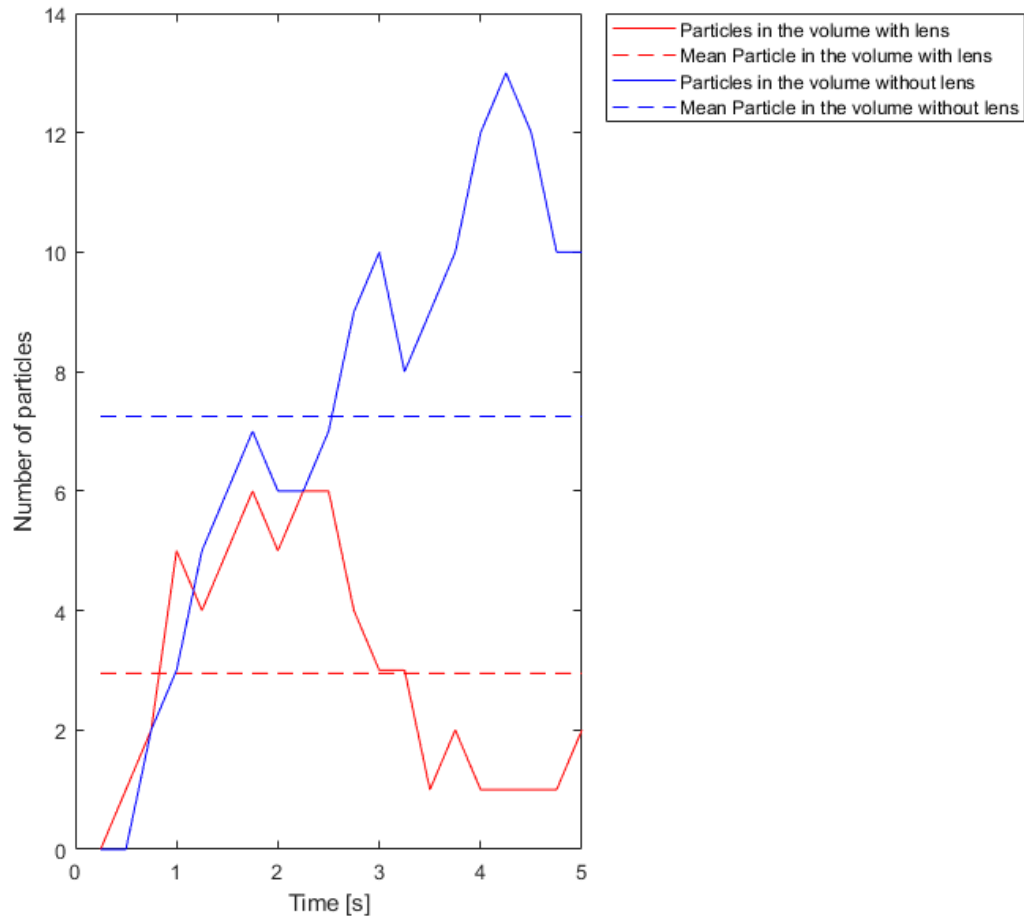


Figure 7.12: *Plot of the particles passing through the cylindrical volume as a function of time*

Discussion

Following the results reported above, the first aspect that can be noticed both in case study A and in case study B is that the eyelashes and the lens of the glasses are useful to protect the ocular surface from the air flow decreasing the kinetic energy; by increasing the length of the eyelashes and the size of the diameter of the circular lens, the decrease is greater. In order to evaluate the effectiveness of eyelashes and lenses on particle deposition, it is necessary to consider the two cases separately, which is due to the fact that the conditions under which the simulations were carried out are different and the particles have sizes, distributions and different densities. However, it is useful to remember that the valid results for the simulation with PM10 can also be useful if you want to study the protection against viral agents such as Sars-CoV-2. SIMA (Società Italiana di Medicina Ambientale), states that atmospheric particulate acts as a carrier, i.e. as a transport vector, for many chemical and biological contaminants, including viruses.

The results and conclusions of this thesis work are based on the fact that the protection of the eye from the deposition of particles is evaluated considering both the number of particles captured by the eyelashes but also on the number of particles that cross the volume positioned in front of the eye. In a real case, assuming the concavity of the eye socket in which the eye is inserted, it is assumed that a part of the particles not captured by the eyelashes or by the lens are deposited on the ocular surface, which would justify the protective function of them. Analyzing the average of particles per second present in the volume mentioned above, it is clear that the presence of eyelashes decreases the number of particles per second in the volume by 41.8% while the presence of the lens decreases the number of particles per second in the volume of 59.4%. These data confirm the effective effectiveness of eyelashes and lenses.

In the case study A, the β parameter clearly shows how as the length of the eyelashes increases, its value increases; this leads to consider that the length of the ideal eyelashes found by Amador *et al* of $L = 7.1mm$ does not coincide with the length that allows to capture the greatest number of particles which in our case is $L = 9.0mm$. About the number of eyelashes, the β curve increases as the number of eyelashes increases with a greater slope for the Run case. The contour plot confirms what can be deduced from β by relating the two fundamental parameters for this study: the length and number of eyelashes. Considering as more effective than the eyelashes that capture more particles, the case with 40 eyelashes of length $L = 9.0mm$ is the most performing. Considering this length, the results show that the increase in the number of eyelashes from 20 to 40 of 24.96% in the walk case and 167% in the run case.

In the case study B, the β parameter evaluated for the lens increases as the diameter increases with a greater slope in the case of sneezing, on the contrary it decreases for eyelashes with a similar slope both in the case of sneezing and in the case of coughing. This shows that the lens is more effective in protecting the eye during an event that generates a more intense field of motion, such as in the case of sneezing.

The presence of the lens leads to a decrease in the capture of the eyelashes of 10% in the case of a lens with a diameter of 4 cm and 12.6% in the case of a lens with a diameter of 5cm for cough, while the decreases are respectively 81.78% and 107.16% in the case of sneezing. Here too there is a confirmation of the fact that by increasing the diameter, the eyelashes have a smaller number of particles captured.

At the end of the discussion, what emerges is that there are some optimal ratios in order to protect the eye from particle deposition: unlike the optimal ratio found by Amador, $L/W = 0.35$, in our work this ratio seems deviates to a higher value $L/W = 0.45$. At the same time, the optimal ratio calculated between the size of the lens and the distance between the lens and the eye is $D/P = 2.5$.

Conclusions

The purpose of this thesis was to evaluate the function of eyelashes in protecting the ocular surface from airborne PM particles and if there was an ideal length and number of eyelashes. In parallel, we were interested in the function that lenses have in protecting the eye from saliva droplets, potentially carrying viral agents. To achieve this aim, a 3D geometry representing the eye, eyelashes and lens was created and numerical simulations were carried out in a computational volume.

The degree of protection to the deposit of particles on the ocular surface that the eyelashes and the lens offer has been evaluated considering how many particles are captured by them and the average how many particles pass very close to the ocular surface. Having evaluated all the data collected, it is possible to state with certainty that:

- The presence of eyelashes and lens decreases the average number of particles that transit near the ocular surface. This protects the cornea against deposition
- The parameters of length and number of eyelashes influence the deposition of particles. With $L/W = 0.45$ there is a greater capture than shorter lengths evaluated in previous work by Amador $L/W = 0.35$ *et.al.*
- A circular lens with $D/P = 2.5$ captures a high number of particles, effectively protecting the cornea.

The work presented is a new field of research and with many new possible modifications and development in the future; a more realistic 3D geometry and a more focused choice on the particles used could lead to more reliable results and a more detailed evaluation of the deposition of particles on the ocular surface.

Appendix

Percentages of the results

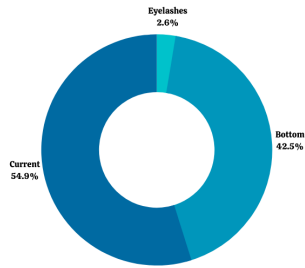
In this appendix, the data relating to the previously presented tables and in the form of percentages are shown through pie diagrams. In *Figure 7.13*, considering $t = 60$ sec for case study A, the percentage of particles deposited or suspended in each patch for the run case, supposed to be of greater interest due to the greater danger, is shown in as a pie chart below. Cases with length eyelashes of $7.1mm$ and $5.6mm$ and a case without eyelashes are evaluated.

In *Figure 7.14*, considering $t = 5$ sec for case study B, the percentage of particles deposited or suspended in each patch for the sneezing case, supposed to be of greater interest due to the greater danger, is shown as a pie chart below. Cases with length eyelashes of $7.1mm$ with lens'd diameter of $d = 5cm$, $d = 4cm$ a case without lens are evaluated.

In both cases, the final instants of the simulations were evaluated, in which there is a high number of particles. From the total particle computation, the particles escaping from the domain from the side walls were not counted as they do not interfere with the results set by this thesis work.

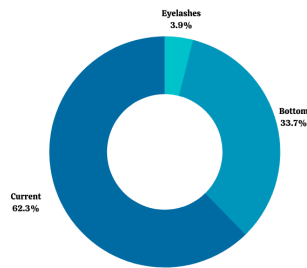
It is important to note how a large number of particles are suspended in the domain, a large number are deposited on the facial surface (bottom) due to the effects of gravity and that although in a reduced percentage, there are particles both on the eyelashes and on the eye; the low percentages, taking into consideration the large number of particles entering, are however representative of an action potentially harmful to the human eye.

CASE RUN EYELASHES
L=5.6 N=40



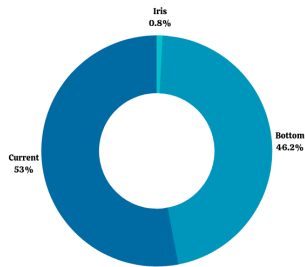
(a) Case Run, eyelashes $L=5.6$ mm, $N=40$

CASE RUN EYELASHES
L=9.0 N=40



(b) Case Run Lens, eyelashes $L=9.0$ mm, $N=40$

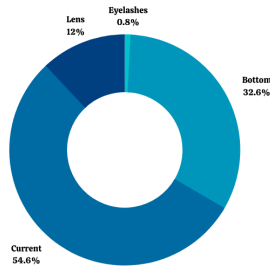
CASE RUN NO
EYELASHES



(c) Case Run, No eyelashes, $N=40$

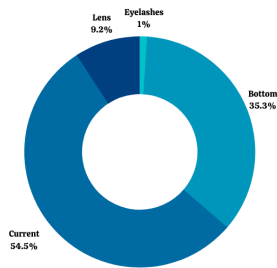
Figure 7.13: Pie chart with particle percentages at instant $t = 60$, Case Run

CASE SNEEZING
L=7.1 N=40 D=5CM



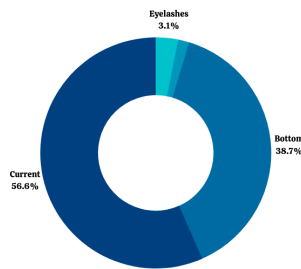
(a) Case sneezing Lens $d=5\text{cm}$, eyelashes $L=7.1\text{mm}$

CASE SNEEZING
L=7.1 N=40 D=4CM



(b) Case Sneezing Lens $d=4\text{cm}$, eyelashes $L=7.1\text{mm}$

CASE SNEEZING
L=7.1 N=40 NO LENS



(c) Case Sneezing no Lens, eyelashes $L=7.1\text{mm}$

Figure 7.14: Pie chart with particle percentages at instant $t = 5$, case Sneezing

Bibliography

- [1] Guillermo J Amador, Wenbin Mao, Peter DeMercurio, Carmen Montero, Joel Clewis, Alexander Alexeev, and David L Hu. Eyelashes divert airflow to protect the eye. *Journal of the Royal Society Interface*, 12(105):20141294, 2015.
- [2] Jasper Fuk-Woo Chan, Kin-Hang Kok, Zheng Zhu, Hin Chu, Kelvin Kai-Wang To, Shuofeng Yuan, and Kwok-Yung Yuen. Genomic characterization of the 2019 novel human-pathogenic coronavirus isolated from a patient with atypical pneumonia after visiting wuhan. *Emerging microbes & infections*, 9(1):221–236, 2020.
- [3] G Seminara, B Carli, G Forni, S Fuzzi, A Mazzino, and A Rinaldo. Commissione per l’ ambiente e le grandi catastrofi naturali accademia nazionale dei lincei.
- [4] Sima Asadi, Anthony S Wexler, Christopher D Cappa, Santiago Barreda, Nicole M Bouvier, and William D Ristenpart. Aerosol emission and superemission during human speech increase with voice loudness. *Scientific reports*, 9(1):1–10, 2019.
- [5] JK Gupta, C-H Lin, and Q Chen. Flow dynamics and characterization of a cough. *Indoor air*, 19(6):517–525, 2009.
- [6] Marcelo Guzman. Bioaerosol size effect in covid-19 transmission. 2020.
- [7] Prateek Bahl, Con Doolan, Charitha de Silva, Abrar Ahmad Chughtai, Lydia Bourouiba, and C Raina MacIntyre. Airborne or droplet precautions for health workers treating covid-19? *The Journal of infectious diseases*, 2020.

- [8] Web page: [https://www.who.int/publications-detail/infection-prevention-and-control-during-health-care-when-novel-coronavirus-\(ncov\)-infection-is-suspected](https://www.who.int/publications-detail/infection-prevention-and-control-during-health-care-when-novel-coronavirus-(ncov)-infection-is-suspected).
- [9] Chuan-bin Sun, Yue-ye Wang, Geng-hao Liu, and Zhe Liu. Role of the eye in transmitting human coronavirus: what we know and what we do not know. *Frontiers in Public Health*, 8:155, 2020.
- [10] Vira Bitko, Alla Musiyenko, and Sailen Barik. Viral infection of the lungs through the eye. *Journal of virology*, 81(2):783–790, 2007.
- [11] Jessica A Belser, Paul A Rota, and Terrence M Tumpey. Ocular tropism of respiratory viruses. *Microbiol. Mol. Biol. Rev.*, 77(1):144–156, 2013.
- [12] Jianyun Lu, Jieni Gu, Kuibiao Li, Conghui Xu, Wenzhe Su, Zhisheng Lai, Deqian Zhou, Chao Yu, Bin Xu, and Zhicong Yang. Covid-19 outbreak associated with air conditioning in restaurant, guangzhou, china, 2020. *Emerging infectious diseases*, 26(7):1628, 2020.
- [13] Keith Zimmerman, Fiona Kearns, and Radouil Tzekov. Natural protection of ocular surface from viral infections—a hypothesis. *Medical Hypotheses*, page 110082, 2020.
- [14] David Douglas and Robert Douglas. Addressing the corona virus outbreak: will a novel filtered eye mask help? *International Journal of Infectious Diseases*, 2020.
- [15] T Schneider and Mats Bohgard. Airborne particle deposition onto the ocular surface. *Indoor Air*, 15(3):215–219, 2005.
- [16] Gang Tan, Juan Li, Qichen Yang, Anhua Wu, Dong-Yi Qu, Yahong Wang, Lei Ye, Jing Bao, and Yi Shao. Air pollutant particulate matter 2.5 induces dry eye syndrome in mice. *Scientific reports*, 8(1):1–13, 2018.
- [17]
- [18] Ankit Gupta, Hemant Bherwani, Sneha Gautam, Saima Anjum, Kavya Musugu, Narendra Kumar, Avneesh Anshul, and Rakesh Kumar. Air pollution aggravating covid-19 lethality? exploration in asian cities using statistical models. *Environment, Development and Sustainability*, pages 1–10, 2020.

- [19] Mitchell H Friedlaender. A review of the causes and treatment of bacterial and allergic conjunctivitis. *Clinical therapeutics*, 17(5):800–810, 1995.
- [20] Siyu Zou, Jinping Zha, Jie Xiao, and Xiao Dong Chen. How eyelashes can protect the eye through inhibiting ocular water evaporation: a chemical engineering perspective. *Journal of the Royal Society Interface*, 16(159):20190425, 2019.
- [21] Web page: <https://www.medicinenet.com/image-collection/eyeanatomydetailpicture/picture.htm>.
- [22] Web page: <http://www.medicalook.com/humananatomy/organs/eyelidsandeyelashes.htm>.
- [23] JI Na, OS Kwon, BJ Kim, WS Park, JK Oh, KH Kim, KH Cho, and HC Eun. Ethnic characteristics of eyelashes: a comparative analysis in asian and caucasian females. *British Journal of Dermatology*, 155(6):1170–1176, 2006.
- [24] R. rumolo, vitolo e., dizionario medico dompè, masson, 1993, isbn 88-214-1914-2.
- [25] Web page: <https://www.onshape.com/>.
- [26] Web page: <https://cfd.direct/>.
- [27] F Moukalled, L Mangani, and M Darwish. The finite volume method in computational fluid dynamics,an advanced introduction with openfoam and matlab. *Springer*, 2016.
- [28] Jesse Liberty. *C++ Unleashed*. Sams, 1999.
- [29] Christopher J Greenshields. Openfoam user guide. *OpenFOAM Foundation Ltd, version*, 2015.
- [30] Hendrik Tennekes, John Leask Lumley, Jonh L Lumley, et al. *A first course in turbulence*. MIT press, 1972.
- [31] David C Wilcox. Turbulence modeling for cfd. la canada, ca: Dcw industries. *Inc, November*, 2006.
- [32] Web page: <https://www.wolfdynamics.com/>.

- [33] Joel Guerrero. Introduction to computational fluid dynamics: Governing equations, turbulence modeling introduction and finite volume discretization basics. *Predavanja, Veljača*, 2014.
- [34] Web page: <https://knowledge.autodesk.com/it/support/simulation-mechanical/learn-explore/caas/sfdcarticles/sfdcarticles/ita/how-to-perform-a-mesh-convergence-study.html>.
- [35] Bert Blocken, F Malizia, T van Druenen, and T Marchal. Towards aerodynamically equivalent covid19 1.5 m social distancing for walking and running. *Questions and Answers. Website Bert Blocken, Eindhoven University of Technology (The Netherlands) and KU Leuven (Belgium). Disponibile su: <http://www.urbanphysics.net/COVID19.html> (ultimo accesso 21 aprile 2020)*, 2020.
- [36] Lydia Bourouiba, Eline Dehandschoewercker, and John WM Bush. Violent expiratory events: on coughing and sneezing. *Journal of Fluid Mechanics*, 745:537–563, 2014.
- [37] ZY Han, WG Weng, and QY Huang. Characterizations of particle size distribution of the droplets exhaled by sneeze. *Journal of the Royal Society Interface*, 10(88):20130560, 2013.
- [38] X Xie, Y Li, ATY Chwang, PL Ho, and WH Seto. How far droplets can move in indoor environments—revisiting the wells evaporation–falling curve. *Indoor air*, 17(3):211–225, 2007.
- [39] Said Elghobashi. On predicting particle-laden turbulent flows. *Applied scientific research*, 52(4):309–329, 1994.
- [40] E Loth. Numerical approaches for motion of dispersed particles, droplets and bubbles. *Progress in energy and combustion science*, 26(3):161–223, 2000.
- [41] Clayton T Crowe and Efstathios E Michaelides. Basic concepts and definitions. *Multiphase flow handbook*, pages 24–25, 2006.
- [42] Zhu Yongjian, Xie Jingu, Huang Fengming, and Cao Liqing. Association between short-term exposure to air pollution and covid-19 infection: Evidence from china. *Science of the total environment*, page 138704, 2020.